Freie Universität Berlin
Department of Physics

DIPLOMA THESIS

Laser-induced Femtosecond Spin Dynamics in Metallic Multilayers

Author:
Adrian Glaubitz
glaubitz@physik.fu-berlin.de

Supervisor:
Priv. Doz. Dr. Uwe Bovensiepen

January 26, 2010

Contents

List of Figures

List of Tables

Diese Arbeit wurde am Fachbereich Physik der Freien Universität Berlin in der Arbeitsgruppe von Prof. Dr. Martin Wolf unter der Anleitung von Priv. Doz. Dr. Uwe Bovensiepen in der Zeit vom 01. Februar 2009 bis zum 01. Februar 2010 angefertigt.

Ich versichere dass die vorliegende Diplomarbeit selbstständig und ohne unerlaubte Hilfe angefertigt wurde.

Datum Unterschrift

Chapter 1

Introduction

Magnetism has been known since the ancient times as a phenomena of nature. Lodestones are natural magnets and are essentially minerals of iron and several of its oxides. They were already referred to in books dated 400 BC, in China. The name "magnet" actually comes from lodestones found in Magnesia, Greece. A mariner's compass is probably the best-known and oldest application of magnetic phenomena, it was first mentioned around 1100 AD in Chinese literature. The easiest construction consists of a magnetized iron needle floating in water.

Despite its long history and scientific interest in magnetic phenomena dating back at least to William Gilbert in the 1600s, magnetism had not been understood so well like electrostatics. Its laws were long time unveiled and it was less well understood due to one basic difference to electrodynamics: *There are no magnetic mono-poles.* It was not until the advent of electric currents that magnetism could be fully explored. In 1819 Ørsted discovered by accident that a current-conducting wire deflected the needle of a compass and about one year later, the two french physicists Jean-Baptiste Biot and Felix Savart deduced the *Biot-Savart-Law* which relates magnetic fields to electric currents as their sources. At the same time Michael Faraday conducted experiments to build a device that can be considered to be the first electric motor. Later he discovered electromagnetic induction and even predicted that light and electro-magnetism are closely related but he could not provide a mathematical formula nor prove the relationship with light. It was the mathematician James Clerk Maxwell who eventually delivered the final mathematical framework now called *Maxwell Equations.* They describe the behavior of electric and magnetic fields in the presence of electric charges and currents, also incorporating the laws discovered by Biot and Savart, which can be deduced from Maxwell's equations.

From electrostatics we know that the basic entity is a single charge (*mono-pole*) whereas in magneto-statics it is a magnetic *dipole.* Think of it as a small compass needle on the atomic scale which aligns itself in an

external magnetic field. In a solid, the total magnetization is defined as the amount of magnetic moment per volume, so the more dipoles are aligned into one direction the stronger the magnetization along this axis will be. To generate such an external field in order to induce a change of magnetization of the solid, one could simply drive a current through a wire according to the Biot-Savart-Law and expose the solid to it. Other ways are mechanical impact or thermal heating, both increase the disorder of all dipoles and thus reduce magnetization. A rather new and sophisticated method of changing magnetization is the method of *spin injection* where a change is induced by "injecting" electrons into a solid. Due to their intrinsic angular momentum (*spin*) electrons have a magnetic moment and thus are able to act on the magnetic moments in the solid (spin-dependent scattering).

Those spin dynamics induced by electronic excitations have potential applications in magnetic recording with a dramatic speed increase over conventional magnetization techniques. In our project the electronic excitation is performed optically, with a femtosecond laser in a SHG[1] pump-probe scheme, the excited electrons are called *hot electrons*[2]. Such an optical excitation can occur on a very short time scale which is limited only by the duration of the laser pulse. Magnetization can thus be changed within pico- to femtosecond lapses and one is able to overcome the lower barrier of time scale of 10^{-9} of induction with the classical method using an external field. Our model setup of such a spin injection or spin transfer experiment are layers of gold which has a large ballistic mean free path and iron as an itinerant ferromagnet.

Spin polarized electrons excited in one ferromagnetic layer travel through a noble metal layer layer and the scattering in the second ferromagnetic layer results in a spin transfer torque which eventually changes the net direction of its magnetization. The Fe/Au/Fe-films are grown epitaxially on transparent, dual-side polished substrates of Magnesium-Oxide (MgO(001)) in an MBE vacuum chamber. The excitation of hot carriers is realized through pumping through the backside of the transparent substrate, the detection through front-probing at the metal-film surface.

Before the final goal of changing the magnetization over spin transfer torque can be achieved, we investigate on the proper preparation of our model system, i.e. the samples. Since the metallic layers are films which are grown epitaxially on the MgO(001) substrate, several parameters can be tuned during preparation to change the properties of the films and thus the measurable output signal. For instance, the optimal thicknesses of ferromagnetic and the gold layer are yet undetermined. The first is important

[1] SHG = Second Harmonic Generation, a method which uses the optical second harmonic signal for surface sensitive probing.

[2] Hot electrons or hot carriers in general are carriers (electrons or holes) which are not in thermal equilibrium with the lattice and can move from one region to another without an externally applied bias.

to maximize the output of spin polarized electrons and the latter for making the gold layer as thick as possible as long the spin polarized electrons can be detected at the gold surface[3] A well established method for determining such thicknesses is by growing the films in wedge-shapes. The wedge form allows to perform the pump-probe measurements with different film thicknesses by simply sweeping with the laser spot along the wedge. Growing a gradient shape is certainly more difficult than simply growing flat films but this way we can perform all measurements on one sample rather than having to prepare several substrates, all with different thicknesses. This makes the measurements more consistent, as only the the sample will be slightly moved with respect to the laser beam, the rest of the setup remaining unchanged.

During the experiments it has shown that the roughness and the parameters of the evaporation process have much more impact on the results obtained in the optical measurements than we had predicted before. In general, a higher roughness of the film surface may yield higher SHG signals due to the field enhancement in localized plasmon modes. We therefore performed experiments to analyze the samples produced to investigate into that direction as well.

1.1 Outline of this thesis

This thesis is divided into five chapters.

In chapter two we start with the current state of the art in the research field of spin dynamics of low-dimensional ferromagnetic structures, the preliminary work of this group and the objectives and goals of the further research and what is covered by this thesis. This includes the use of a femtosecond laser as an excitation source as well a probe with high time resolution to detect the magnetization with *Second Harmonic Generation*. To induce a magnetization in the ferromagnetic films, an electromagnet with dual-nested Helmholtz coils, in which the sample resides during experiments, was designed and constructed as well as a special sample holder.

Chapter three covers all steps and methods which were involved to produce the samples used in the measurements. It is explained how the surface quality of the thin films was achieved and verified[4]. Methods for quality analysis include STM-, RHEED- and AES-measurements[5]. The substrates

[3]For both the "source" ferromagnetic layer and the gold layer we want to maximize the thickness. A thick enough source will maximize the output of spin-polarized electrons but keeping it thin enough that most carrieres excited are ballistic. A thick enough gold layer will decouple the itinerant ferromagnets, assuring that transfer of magnetic momentum is performed through the ballistic electrons and not some kind of exchange interaction.

[4]Impurities and rough film-surfaces impair the excitation transport of the ballistic electrons through scattering

[5]STM: Scanning tunneling microscope, RHEED: Reflection high-energy electron diffraction, AES: Auger electron spectroscopy

were prepared with ultrasonic cleansing in organic solvents, degassing and annealing under ultra-vacuum conditions. We also investigated the influence of the substrate temperature on the sample surface corrugations. The construction and use of the the shutter for producing the samples with gradient thickness (*wedge*) is discussed.

The actual measurements and results of the key experiments are shown and discussed in chapter four.

Finally a discussion and conclusion of the whole thesis is given in chapter five. An outlook towards possible future experiments with the setup are outlined. The future goal of the experiments is to be able to induce a change of magnetization of a second ferromagnetic (i.e. iron) film on top of the gold film (*Spin transfer*). For this, the results from our measurements are hopefully going to be helpful to grow films with the optimum thicknesses to maximize the efficiency of excitation of the ballistic electrons as well their transfer through the non-ferromagnetic gold film. These studies may have high impact on the fundamental studies of spin-dependant electron-electron scattering and transport.

Chapter 2

Methods & Materials

Modern information technologies have gone through a rapid development in the past 30 years. While the first personal computers started with volatile memory sizes in the order of a few kilobytes and non-volatile magnetic memory in the order of a few hundreds kilobytes, concurrent personal computers feature volatile memories with several gigabytes (10^9 Bytes) and non-volatile magnetic storage devices with up to terabytes (10^{12} Bytes). This dramatic increase has been achieved mainly through the boost of data density made possible by smaller structures in solid-state semiconductors for the volatile and the discovery of the *Giant Magneto Resistance* and *Tunneling Magneto Resistance* for the non-volatile magnetic devices.

Even though technology slowly shifts from classical magnetic non-volatile storage devices to flash memory [1], the former are still favored over the latter in most personal computers as they offer a much better cost/data capacity ratio. Furthermore, the overall capacity of flash memory is limited by a lower data density as compared to magnetic storage. The research on fast and high-density non-volatile magnetic memory is therefore still in focus of solid-state physics, more precisely the field of spin dynamics in low-dimensional ferromagnetic structures [1, 2, 3].

2.1 Spin transfer torque

Current state-of-the-art magnetic storage devices employ several advanced techniques which have been developed in the past twenty years to increase data density. Two of them are the already mentioned GMR [4, 5] and TMR effects which allow to replace the coils as detectors for surface magnetization by small solid-state devices to allow measurement of much smaller magne-

[1] "Flash memory" refers to non-volatile random access memory devices, which have floating gate transistors within their memory cells. The transistors can be permanently activated/deactivated by applying a program/erase bias voltage at the gate to fill/empty electrons from/in the gate.

tizations, the spatial dimensions of the device being reduced as well. To increase the data density on the storage medium, i.e. the disk, material scientists have developed new ferromagnetic coatings[2] which allow smaller magnetic domains on the disk. A very recent approach to increase data density further is the technique of *perpendicular recording* [6] which uses materials with higher coercivity[3] with the help of an additional magnetically soft layer which couples to the field of the write head to increase the effective field. Higher coercivity of the material then allows to reduce domain sizes and therefore increasing data density.

However, non of these techniques tackle the problem of faster storage directly. All speed improvements originate from the fact that data density increases and thus more data can be read or written within the same time the read/write-head flies over the spinning disks. A direct approach has to address the method how magnetization is changed in the ferromagnetic storage layer. Currently all magnetic and magneto-optic storage devices use coils to generate magnetic fields to change magnetization. Since the coils are driven by electronic circuits, the speed of magnetic switching is limited by the cut-off frequency of the electronic components. Fastest switching in electronic circuits that can be achieved with current technologies is in the nanosecond regime. In [7], fastest magnetic switching with conventional pulses is stated to have 100 ps pulses at best. However, in chapter 15 [8], Stöhr elaborates, that faster switching is possible when using femtosecond lasers.

Spin transfer torque is a completely new concept to induce magnetization changes in ferromagnets [9], [10]. Like GMR, the fundamental physics behind it is spin-dependent scattering. In GMR, electrons are filtered by their angular momentum (due to spin-dependent scattering) passing through one of the ferromagnetic layers of a *spin valve* structure and tunnel through a non-magnetic interlayer into a second ferromagnetic layer. Electrons can only pass when both ferromagnetic layers have parallel magnetization. Now, if we change the setup such that the second layer is rather magnetically soft and its magnetization is non-parallel to that one in the first layer, the electrons from the first layer change the magnetization in the second layer by transfer of angular momentum. The magnetization in the ferromagnet exerts a torque on this flow of angular momentum and the flow generates an opposite torque onto the ferromagnets magnetization so that both the flowing spins and the magnetization in the ferromagnet finally reach parallel alignment.

From this rather simple model it is obvious how a device for spin transfer has to be constructed. It is a spin-valve structure consisting of two

[2]The platters themselves are made from non-magnetic materials like aluminum or glass. The data is stored on thin magnetic films, made from iron oxides or cobalt alloys.

[3]The coercivity of a ferromagnet determines the necessary strength of an applied field to fully demagnetize it.

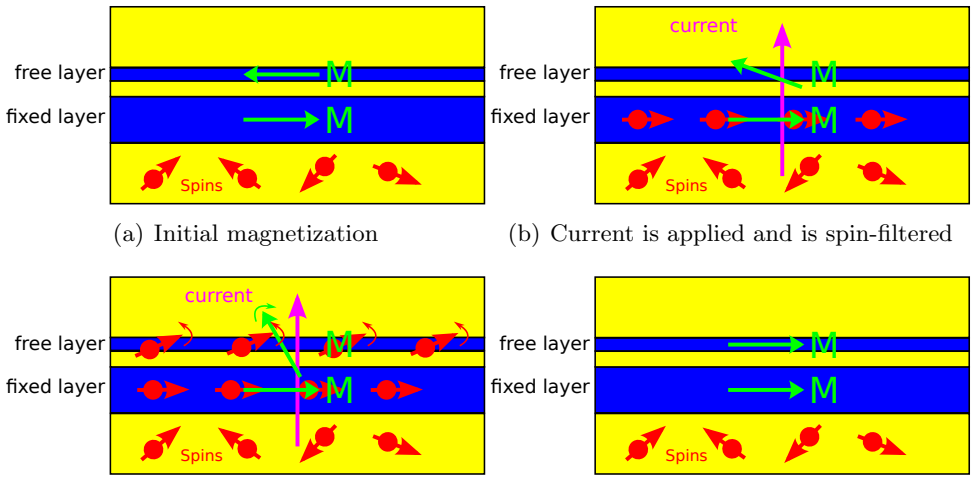

(a) Initial magnetization

(b) Current is applied and is spin-filtered

(c) The spin-filtered electrons flip $\vec{M}$

(d) After removing the current

Figure 2.1: A nano pillar multi-layer setup to induce spin transfer with an electric current. Electrons from the lower copper layer have initially disordered spins, the magnetizations in the two ferromagnetic layers are anti-parallel (a). Due to fluctuations the magnetization in the free layer ceases to have an anti-parallel orientation with the first magnetic layer. Upon applying an electric current, electrons from the lowest copper layer flow through the *fixed layer* where they are spin-filtered to pass through another non-magnetic layer which separates the two magnetic ones (b). Once the spin-filtered electrons pass through the *free layer*, spin torque is exerted to the non-parallel magnetization in that layer resulting which aligns it parallel to the fixed layer (c). After the current is removed, magnetization, the free layer can remain in the switched state (d).

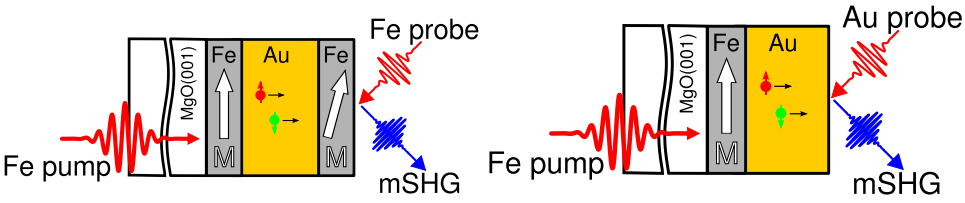

(a) Setup for spin transfer experiment (b) Setup for investigation of spin transport

Figure 2.2: A substrate of MgO(001) is the basis of the model setup that we investigate. With molecular beam epitaxy techniques, layers of iron and gold are deposited onto the substrate. Electrons are optically excited in the first ferromagnet and transfer their spin to a second ferromagnet which is separated by a paramagnetic spacer (a). To investigate spin transport in gold, we waive for the second ferromagnet and probe the magnetization at the gold surface (b).

magnetic layers separated by a non-magnetic one. Additional itinerant conducting layers have to be provided as source and drain for the electrons. The electrons are spin-filtered by the first magnetic layer, travel through the non-magnetic layer to finally pass through the second magnetic layer to exert an angular momentum, finally they are collected by the drain layer. Figure 2.1 illustrates such a setup which was actually put into practice in [11, 12].

However, such setups still have the disadvantage that the switching of magnetization occurs electrically and thus we are still confined regarding the speed of switching. This is the point where lasers come to the rescue. If we are able to use pulsed lasers with pulse-lengths in the femtosecond regime to excite spin-polarized electrons in a ferromagnetic layer, let them pass through a non-magnetic layer and finally exert spin torque in a second magnetic layer, we will achieve switching of magnetization at unprecedented speeds. In fact, we have conceived such a setup which uses multi-layers of iron as ferromagnets and gold as non-magnetic spacer layer. Figure 2.2 (a) shows the principal setup of our concept.

Key tool in our experiments is a custom femtosecond laser system which provides ultrashort and high-energy pulses necessary to excite spin-polarized electrons with sufficient energy (*hot electrons*). The setup allows time-resolved linear (MOKE) and non-linear (SHG) optical spectroscopy. The technique behind the measurements is a pump-probe scheme where the laser beam is split into a high-intensity (80 % of beam power) pump and low-intensity probe beam (20 %). Time resolving is carried out with a delay stage which varies the two beams relative path lengths on a picosecond time scale. Detailed description of the experimental setup is found in section 2.4.

2.2 Specific goals of this thesis

Before the final goal of this project, the optical switching of magnetization can be carried out, detailed investigations of the electron and spin dynamics involved have to be performed. For this, the model setup is altered by waiving for the second ferromagnetic layer (see Fig. 2.2, (b)). This allows to measure both the charge and the spin components of the carrier transport with surface sensitive methods. Furthermore, the proper technique for producing samples has to be chosen by means of measurements of film quality (see chapter 3). The goals of this thesis within the projects frame were both the production and analysis of the samples and further investigations of the spin and electron dynamics. This includes the following tasks:

- construction of a shutter for controlled sample preparation
- construction of a magnet allowing both MOKE and SHG measurements
- development of techniques for sample preparation and of characterization procedures
- further investigation of electron and spin dynamics

2.3 Experimental techniques

Our all optical approach for exciting and probing the spin dynamics in the specimen implements several linear and non-linear optical effects. The latter ones are more important for us. In particular, we are focussing on the following effects:

- Linear reflectivity to measure bulk electron and lattice dynamics
- Magneto optical Kerr effect (MOKE) to measure bulk spin dynamics
- Second Harmonic Generation (SHG) to measure electron, lattice and spin dynamics at surfaces and interfaces

2.3.1 Linear Reflectivity

As already mentioned, we are using a pump-probe scheme to excite and investigate the spin dynamics in our samples. The main concept behind this technique is to excite the medium with a high power pump pulse and probe the dynamics after a certain delay after excitation with a much weaker probing pulse. Usually, the two beams are obtained by separating the laser beam with a beam splitter. When the delay between pump and probe is zero, however, the situation changes and new effects arise. With zero delay, pump

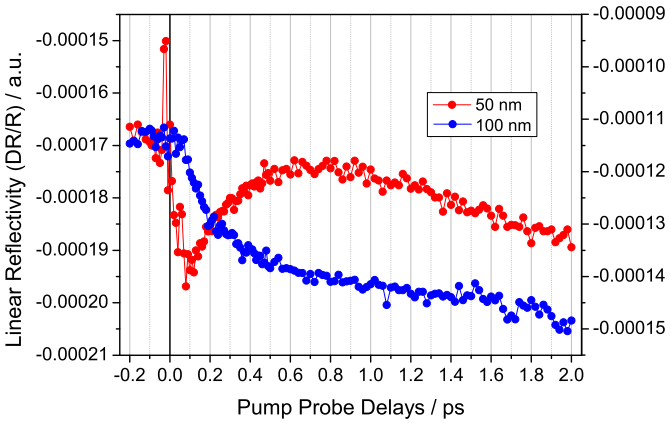

Figure 2.3: Sample plots for linear reflectivity showing the linear reflectivity for 50 and 100 nm gold layers. The peak at zero delay arises from the spatial and temporal overlap of pump and probe and can hence be used as a calibration for zero delay.

and probe are superimposed and the excitation depends of the coherent superposition of the beams.

As we are primarily concerned with the pump-induced changes in the second harmonic and not the fundamental signal, we are not further discussing this topic here, more details can be found in [13]. However, the coherent artifact becomes handy in our experimental setup. Since the generation of the coherent artifact arises from the spatial and temporal overlap of pump and probe beams, it can be used to determine the *zero* for the delay stage. Since the linear reflectivity is measured with a separate photo diode instead of the photo multiplier we have an independent mean to calibrate the zero delay of the pump-probe setup since the delay $t = 0$ can be easily distinguished by peaks arising from the coherent artifact (see Fig. 2.3).

2.3.2 MOKE

Magneto-optical Kerr effect (MOKE) describes a phenomenon which allows optical detection of magnetization. The basic effect is the interaction of polarized light with medium due to magnetization. The polarization of an incident light beam is altered upon reflection. For transmission the principally same effect is referred to as Faraday effect.

To understand these effects on the macroscopic scale, we consider the dielectric constant of a material as a tensor rather than a scalar:

$$\epsilon(\omega) = \begin{pmatrix} \epsilon_{xx} & 0 & 0 \\ 0 & \epsilon_{yy} & 0 \\ 0 & 0 & \epsilon_{zz} \end{pmatrix} \tag{2.1}$$

For an optically isotropic medium, $\epsilon_{xx} = \epsilon_{yy} = \epsilon_{zz}$ (thus ϵ is a scalar). If the magnetization is non-zero, the off-diagonal elements will become non-vanishing. From [14], the tensor for a magnetized medium becomes:

$$\epsilon(\omega) = \begin{pmatrix} \epsilon_{xx} & \epsilon_{xy} & -\epsilon_{xz} \\ -\epsilon_{xy} & \epsilon_{xx} & \epsilon_{yz} \\ \epsilon_{xz} & -\epsilon_{yz} & \epsilon_{xx} \end{pmatrix} \tag{2.2}$$

and thus the medium is no longer isotropic. Macroscopically, MOKE can be explained as follows: We consider the incident light beam (linear polarized wave) as a superposition of two circular polarized waves with opposite rotation direction but equal amplitude. When the electromagnetic wave is reflected from a medium with an anisotropic dielectric constant, the two superposing waves experience different refractive indices and thus different velocities within the medium. This results in a phase shift between the two constituents and finally in rotation of the linear polarization plane. If the magnetization is perpendicular to the the surface (polar MOKE) for example, the rotation due to the Kerr effect is proportional to the magnetization $\mathbf{M}$ which is proportional to the ratio of the components of the dielectric tensor:

$$\Theta_K \propto \frac{\epsilon_{xy}}{\epsilon_{xx}} \propto \mathbf{M} \tag{2.3}$$

Depending on the geometry, there are three configurations for MOKE (see Figure 2.4): Either with in-plane magnetization (transversal and longitudinal MOKE) or out-of-plane magnetization (lying within the plane of incidence, that is along the surface normal: polar MOKE). To fully understand MOKE on the microscopic scale beyond the given phenomenological explanation, quantum mechanics will play the primary part. It is the combined effect of spin-orbit coupling and exchange interaction with the selection rules for optical transitions which yield a proper in-depth explanation of MOKE [15].

Linear MOKE is generally bulk sensitive. For surface sensitive magnetization measurements, the non-linear optical variant of MOKE has to be applied, also known as magneto-induced second harmonic generation (mSHG) which will be discussed in Section 2.3.5. Moreover, linear MOKE is less sensitive since the off-diagonal tensor elements which define the change of polarization and thus magnetization of the sample, are usually very small. For mSHG, the even and odd tensor components (with respect to reversal

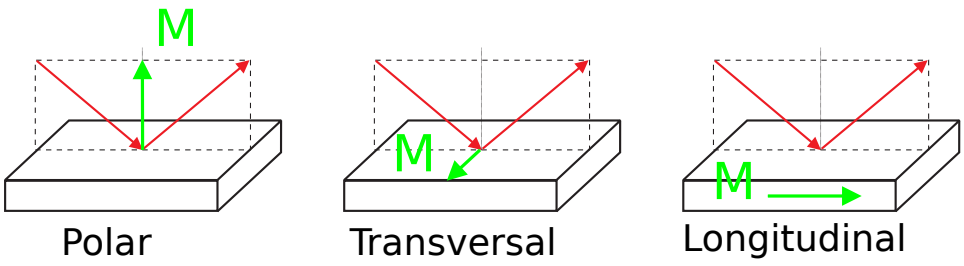

Figure 2.4: Depending on the orientation of the magnetization in the specimen with respect to the incident light beam, one talks about *polar*, *transversal* or *longitudinal mode*.

of magnetization, see Sec. 2.3.4) are of comparable magnitude and therefore yield much high effects than linear MOKE. As an example, in [15] it is shown for Ni that with linear MOKE, the ratio of even and odd tensor components is around 0.03 whereas it is 0.27 for non-linear magneto-optics.

2.3.3 Linear vs. non-linear optics

Non-linear optics hasn't evolved before the invention of the first lasers in the 1960s since it requires high intensity fields to produce a detectable non-linear optical response. Non-linear effects occur, for example, when focussing a high-intensity ultrashort laser pulse onto a specimen which will react to the irradiation with an *optical response*. We consider an incoming electric field $\mathbf{E}(\mathbf{r},t)$ and the specimen as a medium in which a polarization $\mathbf{P}(\mathbf{r},t)$ is induced. The corresponding non-homogeneous wave equation for the propagation of $\mathbf{E}$ through a medium is derived from Maxwell's equations [16]:

$$\triangle\,\mathbf{E}(\mathbf{r},t)+\frac{1}{c^2}\frac{\partial^2}{\partial t^2}\mathbf{E}(\mathbf{r},t)=-\frac{4\pi}{c^2}\frac{\partial^2}{\partial t^2}\mathbf{P}(\mathbf{r},t) \tag{2.4}$$

This wave equation describes the optical response of the medium. This response perturbs the further propagation so that a mutual dependence exists, which results in the various linear and non-linear optical effects. For linear effects, the polarization is usually expressed as follows:

$$\mathbf{P}(\mathbf{r},t)=\epsilon_0\int_{-\infty}^{+t}dt'\int_{-\infty}^{+\infty}d^3r'\chi^{(1)}(\mathbf{r}-\mathbf{r}',t-t')\mathbf{E}(\mathbf{r}',t') \tag{2.5}$$

with ϵ_0 being vacuum permittivity and $\chi^{(1)}$ the first-order susceptibility tensor which accounts for the fact that the medium might be anisotropic, i.e. the response field might not be parallel to the electric field. This linear expression is valid as long as the intensity of the irradiating electric field $\mathbf{E}(\mathbf{r},t)$ is not too high. For high intensities, non-linear effects will arise and

the above expression has to be expanded in series of the electric field to account for the non-linear terms, thus for the n-th order:

$$\begin{aligned}\mathbf{P}^{(n)}(\mathbf{r},t) &= \epsilon_0 \int_{-\infty}^{+t} dt_1..dt_n \int_{-\infty}^{+\infty} d^3r_1..d^3r_n \times \\ &\quad \chi^{(n)}(\mathbf{r}-\mathbf{r}_1, t-t_1, .., \mathbf{r}-\mathbf{r}_n, t-t_n)\mathbf{E}(\mathbf{r}_1,t_1)..\mathbf{E}(\mathbf{r}_n,t_n)\end{aligned} \tag{2.6}$$

and the total polarization has to be summed over all n:

$$\mathbf{P}(\mathbf{r},t) = \sum_n \mathbf{P}^{(n)}(\mathbf{r},t) \tag{2.7}$$

First order terms correspond to linear, all higher terms to non-linear effects. Since we are dealing with linear and second harmonic effects only, we neglect terms of order 3 and higher. We calculate the Fourier transformation of to yield polarization in frequency domain, restricting us to *Sum Frequency Generation* (i.e. only considering sums of the composing frequencies):

$$\mathbf{P}(\omega) = \mathbf{P}^{(1)}(\omega) + \mathbf{P}^{(2)}(\omega_1+\omega_2) + ... \tag{2.8}$$

$$= \epsilon_0[\chi^{(1)}(\omega)\mathbf{E}(\omega) + \chi^{(2)}(\omega_1+\omega_2)\mathbf{E}(\omega_1)\mathbf{E}(\omega_2) + ...] \tag{2.9}$$

For the case of $\omega_1 = \omega_2$ we are dealing with *Second Harmonic Generation* which is underlying principal physics of the main tool for our measurements, see section 2.3.4.

2.3.4 Second Harmonic Generation

Second Harmonic Generation (SHG) is a special case of sum frequency generation (SFG) where two photons unite to generate a new photon with the energy being the sum of the energies of the single photons. SHG is the degenerate case of SFG in the sense that the frequencies of the two photons are identical, thus $\omega_1 = \omega_2$. From 2.8 and 2.9, the polarization for SHG becomes in electric-dipole approximation:

$$\mathbf{P}^{(2)}(\omega_1+\omega_2 = 2\omega) = \epsilon_0\chi^{(2)}(2\omega)\mathbf{E}(\omega)\mathbf{E}(\omega) \tag{2.10}$$

or for just one component:

$$P_i^{(2)}(2\omega) = \epsilon_0\chi_{ijk}^{(2)}(2\omega)E_j(\omega)E_k(\omega) \tag{2.11}$$

The interesting quantity in this context is the susceptibility χ which is a third rank tensor with 27 components. However, since the frequencies of the two contributing waves are identical, we have a symmetry regarding the permutations of j and k and thus the tensor χ reduces the amount of its non-vanishing components to 18 since $\chi_{ijk}^{(2)} = \chi_{ikj}^{(2)}$. The amount of components is

reduced further when choosing a particular crystal symmetry, polarization geometry or by choosing a particular crystallographic orientation in the optical setup.

It remains to clarify the importance of SHG for surface investigations. SHG has a very high sensitivity to the properties of surfaces and interfaces of centrosymmetric media such as their symmetry structure, charge distribution and magnetization and so on. This specific sensitivity of SHG can be understood easily, let's consider equation 2.9. In case of a centrosymmetric crystal, 2.9 has to be invariant against inversion symmetry. Thus exchanging $\mathbf{E}$ and $\mathbf{P}$ for $-\mathbf{E}$ and $-\mathbf{P}$ should yield the same mathematical result, thus 2.9:

$$\mathbf{P} = \epsilon_0[\chi^{(1)}(\omega)\mathbf{E}(\omega) + \chi^{(2)}(2\omega)\mathbf{E}(\omega)\mathbf{E}(\omega) + ...] \tag{2.12}$$

becomes:

$$-\mathbf{P} = \epsilon_0[-\chi^{(1)}(\omega)\mathbf{E}(\omega) + \chi^{(2)}(2\omega)\mathbf{E}(\omega)\mathbf{E}(\omega) + ...] \tag{2.13}$$

However, both equations can be valid simultaneously only if all even orders of χ are zero. Therefore in a centrosymmetric medium, the contributions to SHG are *zero*. At surfaces, however, the inversion symmetry of centrosymmetric crystals is broken and the odd components of contributions to polarization become non-zero.

Within electric-dipole approximation, for centrosymmetric media, SHG processes are sensitive to surfaces and other interfaces where inversion symmetry is broken.

2.3.5 Non-magnetic vs. magnetic SHG

Upon irradiating the medium with a high-intensity laser pulse, a SHG signal is generated which is used to probe electronic and magnetic properties. This is possible since the electric field at second harmonic is compound of two signals:

- a non-magnetic or "crystallographic" component which reflects changes of the band structure and the electronic distribution function; both are monitors for electron and lattice dynamics since vibrations and lattice deformations are reflected there
- a magneto-induced component which is, accordingly to all known experimental results, proportional to the local magnetization $\mathbf{M}$

We refer to the two components as *even* and *odd* component, forming the total electric field at 2ω. Even and odd here refer to the symmetry of

the components regarding inversion of the external magnetic field: the even component remains unchanged while the odd component flips its sign.

We write down the components of the SHG electric field:

$$\mathbf{E}(2\omega) = \mathbf{E}_{even}(2\omega) + \mathbf{E}_{odd}(2\omega) \tag{2.14}$$

In our optical experiment, we measure intensities rather than electric fields, which can be expressed as:

$$\begin{aligned} I^{\uparrow\downarrow}(2\omega) &= |\mathbf{E}_{even}(2\omega) + \mathbf{E}_{odd}(2\omega)|^2 \\ &= E^2_{even}(2\omega) + E^2_{odd}(2\omega) \pm 2E_{even}(2\omega)E_{odd}(2\omega)\cos\varphi \end{aligned} \tag{2.15}$$

Here $I^{\uparrow\downarrow}(2\omega)$ refers to the direction of the saturating external magnetic field which determines the sign of the cross term (thus $\pm 2E_{even}(2\omega)E_{odd}(2\omega)\cos\varphi$). With the experimentally proved approximation $|\mathbf{E}_{even}| \gg |\mathbf{E}_{odd}|$, we find an expression which involves the magnetization:

$$\begin{aligned} I^{\uparrow\downarrow}(2\omega) &\propto |\mathbf{E}_{even}(2\omega) + \mathbf{E}_{odd}(2\omega)|^2 \\ &\approx \left|\vec{\beta}\right|^2 + 2\vec{\alpha}\vec{\beta}M = kM + c \end{aligned} \tag{2.16}$$

Now, when we want to use SHG as a tool to measure *pump-induced variations* (both non-magnetic and magnetic) of the non-linear response under laser irradiation, we have to define the quantities for these components and then derive them from the equations for the intensities (equations 2.15 and 2.16). Since we want to measure the variations *time-resolved*, we have to measure intensities within defined time intervals. The standard scheme for time-resolved measurements of pump-induced variations of the SHG usually involves a modulation technique which uses a chopper in the pump beam working at a frequency lower than the repetition rate of the laser but faster than any other experimental variations. With the chopper, we can measure the probe signal both with and without excitation by the pump, allowing to cancel noise with the help of a lock-in amplifier which is triggered by the chopper (see Fig. 2.5 and Sec. 2.4). The evolution of the variations in time are measured by delaying pump and probe beam with respect to each other. This is realized through a delay stage which varies the path length of the pump beam with high precision allowing to set the delay between the two beams as they hit the sample.

For each datapoint on the time axis and thus position of the delay stage defining the time delay between pump and probe, we measure the SHG intensity for opposite directions of the external magnetic field $\mathbf{H}$ with a detector synchronized with the chopper yielding the intensities in the presence $I^{\uparrow\downarrow}(t)$ and in the absence $I_0^{\uparrow\downarrow}(t)$ of excitation (the last quantity does

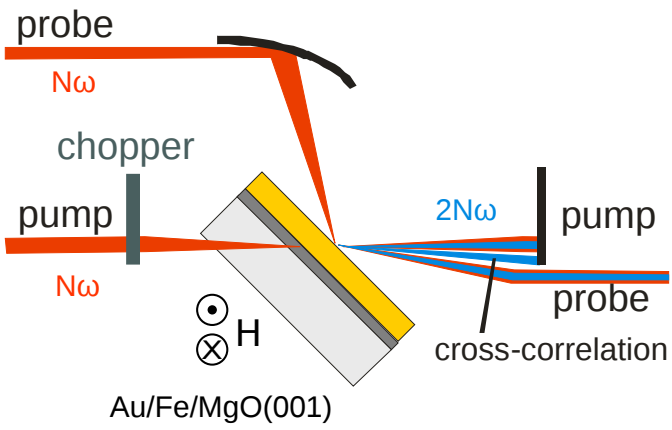

Figure 2.5: Principal experimental configuration of the pump-probe scheme. The pump beam hits the sample from the backside after passing through a chopper. The chopper is introduced to measure the pump-induced effects in the probe signal with low noise. The probe signal is measured from the front-side at the gold surface. The sample sits in a magnetic field which is switched in its direction back and forth for every delay step. The resulting SHG signals are pump, cross correlation and probe. Only the latter is detected, the other two being blocked by a knife. The probe beam passes through a monochromator and is detected with a photo-multiplier (not depicted).

not depend on the pump-probe delay but may vary in time due to external fluctuations of laser intensity, alignment, etc.). We combine the measured intensities into:

$$D^{\pm}(t) = \frac{I^{\uparrow}(t) \pm I^{\downarrow}(t)}{I_0^{\uparrow}(t) \pm I_0^{\downarrow}(t)} \tag{2.17}$$

It has been shown in [17] that the phase φ is smaller than 15° when measured in single-beam interferometry and therefore we can use $\cos\varphi \approx 1$ in Equation 2.15. Together with $E_{odd}^2 \ll E_{even}^2$, the even and odd components, which describe electron/lattice and spin dynamics respectively, become:

$$\Delta_{even}(t) = \sqrt{D^{+}(t)} - 1 \approx \frac{E_{even}(t) - E_{even}^0}{E_{even}^0} \tag{2.18}$$

for the electronic variations (electron/lattice dynamics) and

$$\Delta_{odd}(t) = \frac{D^{-}(t)}{\sqrt{D^{+}(t)}} - 1 \approx \frac{E_{odd}(t) - E_{odd}^0}{E_{odd}^0} \approx \frac{M(t) - M_0}{M_0} \tag{2.19}$$

for the magnetic variations.

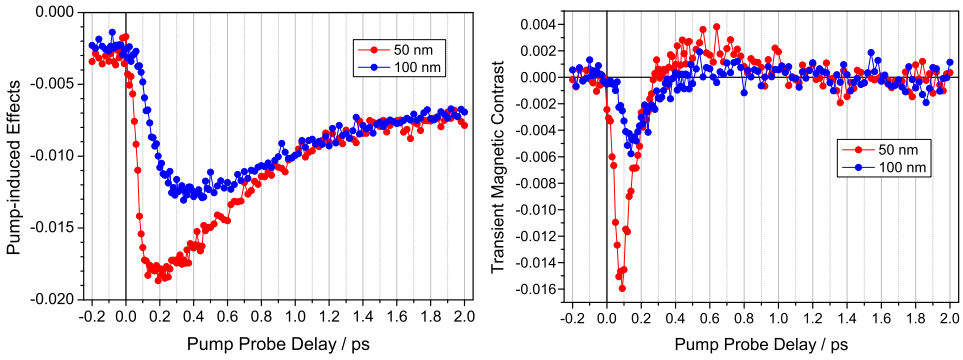

(a) Pump-induced effects (b) Transient magnetic contrast

Figure 2.6: Excerpt from SHG measurements on MgO(001)/Fe/Au multi-layers. Plot (a) shows the pump-induced effect of the SHG signal in dependence on the pump-probe delay for 50 and 100 nanometer thick Au layers. The maximum amplitude indicates the arrival of the ballistic electrons at the gold surface. (b) shows the dynamic contrast over the delay. The first, sharp peak indicates the arrival of the ballistic electrons, the overshoot is caused by electrons in the diffusive transport regime.

The expressions 2.18 and 2.19 yield the non-magnetic and magnetic variations and are thus our main tools for measuring pump-induced variations. However, when dealing with non-ferromagnetic media, equation 2.19 cannot be used to account for the magnetic variations since the material does not exhibit any magnetization. In order to be still able to measure changes induced by magnetization dynamics, we measure the *magnetic contrast* or magnetic asymmetry. It is defined as the relative variations of the SHG intensity for opposite directions of the external magnetic field. Thus:

$$\rho = \frac{I^{\uparrow}(2\omega) - I^{\downarrow}(2\omega)}{I^{\uparrow}(2\omega) + I^{\downarrow}(2\omega)} \tag{2.20}$$

using Equation 2.15, we can also write:

$$\rho \approx 2\frac{|E_{odd}|}{|E_{even}|}\cos\varphi \tag{2.21}$$

.

Figure 2.6 shows typical result plots for the *even component* (pump-induced effects) and *transient magnetic contrast* from our measurements. The pump-probe delay usually ranges between -0.5 and 5.0 ps which covers the most interesting regions for the evolution of the SHG signals[4]. The relative signal changes are usually within a percent of the electric field. This

[4]As we will see later, it turned out, that despite that there are other interesting effects detectable when scanning with longer pump-probe delays.

is enough to detect the ballistic electrons and distinguish them from the diffusive electrons, the former are manifested in the first peak while the latter induce a change of sign and an overshoot in the signal (Figure 2.6). The position of the peaks is mainly determined by the thickness of the films whose correlation is one of the major points of interest to be investigated in this work. Accurate measurements for different thicknesses will allow to determine the velocities of both ballistic and diffusive transport in the metal films.

2.4 Experimental Realization

The experimental setup consists of the following main components:

- the femtosecond laser as excitation source and signal probe
- the optics on the laser table to split the laser beam into pump and probe, compensate dispersion, control pump-probe delay and a non-linear optical crystal (BBO) for SHG reference
- a home-made magnet in Helmholtz configuration to produce homogeneous fields in the sample plane (both vertically and horizontally)
- a photodiode to detect linear response and a photo multiplier with a monochromator for the detection of non-linear response
- a lock-in amplifier and a photon counter connected to the photo diode and photo multiplier respectively, both triggered by the chopper in the pump-beam
- a computer running a *LabView* program code to control the delay stage and read and evaluate the outputs from the lock-in and photon counter

A schematic view of the complete setup can be seen in Figure 2.7. The caption of this figure contains a detailed description of the interaction of the single components, the most important of these are described in the following sections.

2.4.1 Femtosecond Laser

The laser employed in our setup is a *mode-locked* femtosecond laser system. This means, that unlike a normal continuous wave laser which produces a time-steady signal, the femtosecond laser generates single pulses. The pulses are necessary to achieve the minimum time resolution to measure ultra-fast electronic and magnetic phenomena whose durations lie within the pico- to femtosecond regime.

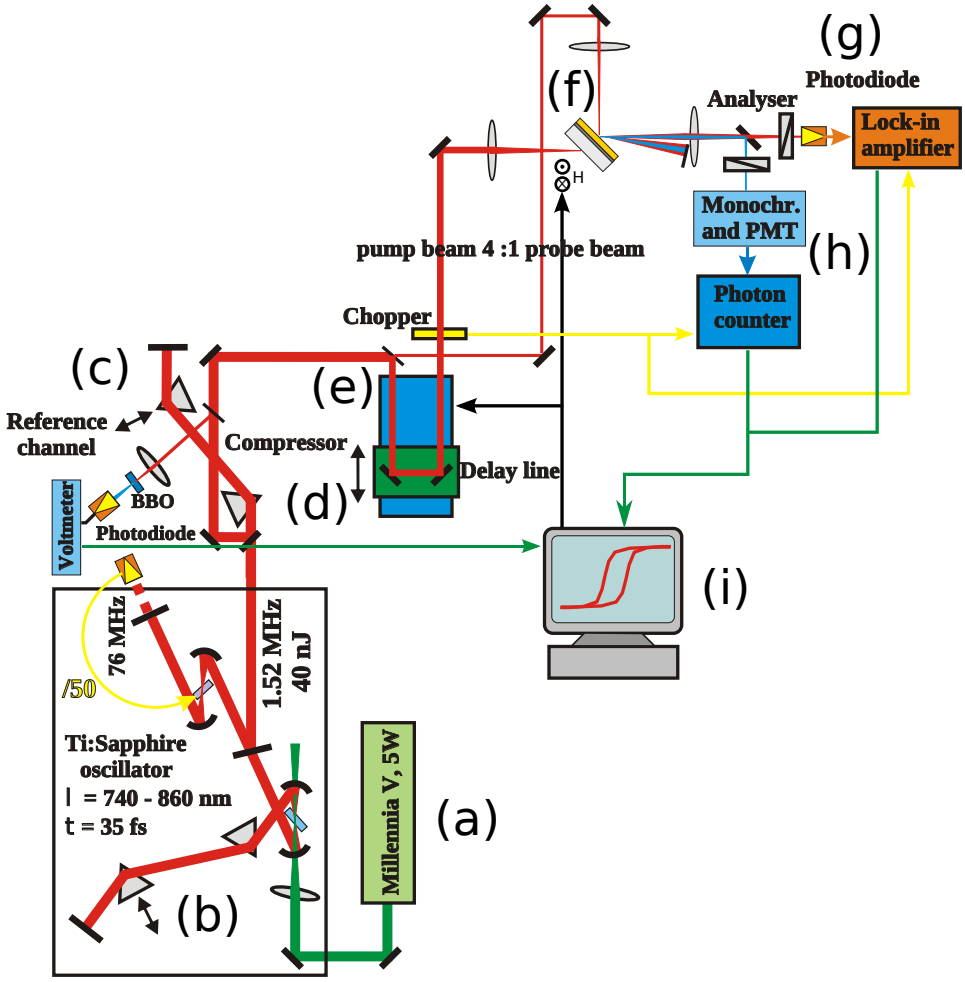

Figure 2.7: Overview of the complete setup for measurements. A 5W cw-laser (a) is used to pump a Ti:Sapphire crystal in the home-made femtosecond laser (b). The cavity is dumped at a rate of 1.52 MHz. A reference channel (c) is established with a BBO crystal to check the SHG signal. To pre-compensate the positive group dispersion of the laser pulse due to the optical elements, two prism compressors are employed, one within the cavity box (b) and a second one outside the box (d). The pump-probe delay can be tuned with a delay line (e) which varies the length of the beam path of the pump beam, pump and probe are split right before the delay line, with a ratio of 4:1. The pump beam runs through a chopper triggering both the photon counter (h) and the lock-in amplifier (g). The sample is located within the magnet at position (f), where both pump and probe adjoin again and the generated SHG signal is filtered with a knife and a dichroic mirror reflecting the SHG signal towards the slit of the monochromator and transmitting the fundamental to the photo-diode. The measured signals are fed into a computer which runs the software *LabView* (i). The computer controls both the delay line (e) and the magnet (f).

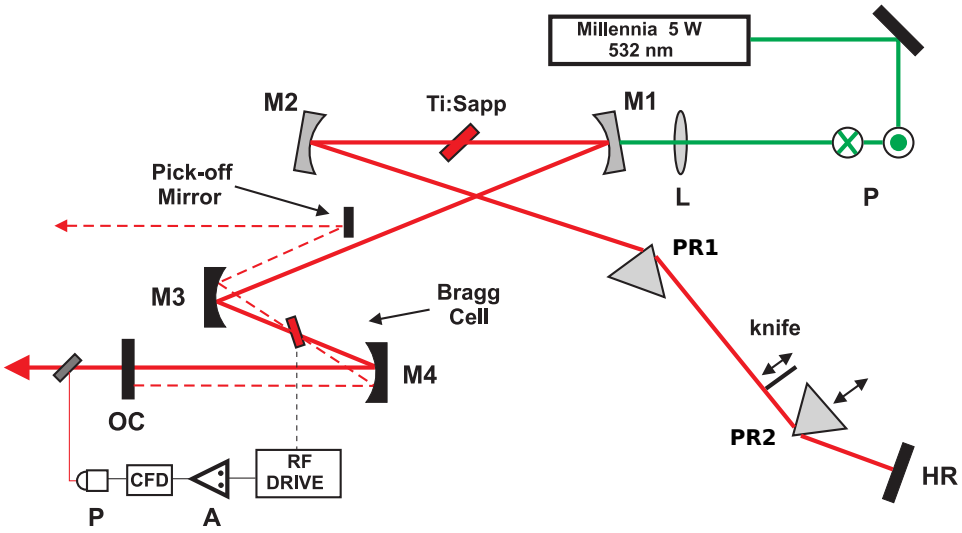

Figure 2.8: Configuration of the home-made laser employed in our setup. The oscillator system is pumped by a Nd:YVO_3 cw laser (Millennia). A periscope (**P**) rotates the plane of polarization of the beam parallel to the table, the lens (**L**) focusses it into the Ti:Sapp crystal which defines an oscillator together with the two mirrors **M1** and **M2**. The cavity dumping is performed by the Bragg-cell and mirrors **M3** and **M4**. The prisms **PR1** and **PR2** compensate negative group dispersion, the knife is used to tune the wavelength since it cuts parts of the spectrum. The main cavity is defined by the mirrors **OC** and **HR**.

Our laser is a home-made Titanium:sapphire (Ti:Al_2O_3) oscillator which provides pulses as short as 35 fs[5]. The laser was built by a former PhD student of this group and has been employed in a number of studies in surface science. It has two principal operating modes:

- normal oscillator mode (76 MHz repetition rate)
- cavity-dumped mode (1.52 MHz repetition rate)

In normal oscillator mode (@76 MHz), the pulse energy is around 6 nJ. By enabling cavity dumping, the pulse energy can be increased up to 42 nJ. The pulse duration always remains 35 fs. Since cavity dumping is performed by electronic switching (acousto-optical modulator, AOM), the dumping rate can be tuned externally and thus one has variable repetition rates.

[5]Since there are additional optical components involved, without the cavity dumping, pulses could be as short as 25 fs [18]).

Mode locking

Mode locking is the basic concept behind a pulsed laser system in the femtosecond regime. Within the laser oscillator cavity of a *continuos wave* laser (steady output as opposed to pulsed lasers), there are only a few modes and they oscillate independently from each other. In a mode-locking system, however, modes become coupled with each other so they form a wave package with high energy and large bandwidth instead of single continuous waves with discrete, nearly vanishing bandwidths[6]and small energies. To give some numbers: the mode-locked Ti:Sa laser has up to 250000 modes and 10 THz bandwidth while the conventional He:Ne laser yields only a couple of modes and a few GHz for the bandwidth.

Mode locking occurs when a mode of frequency ν is modulated with the frequency f which results in additional modes in the sidebands with frequencies $\nu + f$ and $\nu - f$. There are generally two types of mode locking: *active* and *passive*. In active mode locking, the laser oscillator is modulated externally with an electronic device (e.g. piezo, loudspeaker, servo, etc). Passive mode locking, on the other hand, takes place directly in the cavity of the laser. An optically active crystal works as an optical Kerr lens (*optical Kerr effect*) and amplifies locked modes.

The optical Kerr effect (not to be confused with the magneto-optical Kerr effect) is a phenomenon of non-linear optics. What happens is that the crystal changes it refractive index upon irradiation with laser light of high intensity. The refractive index can thus be written as:

$$n(E) = n_0 + cE^2 \tag{2.22}$$

To initiate mode locking, one has to introduce a perturbation into the system which can be easily achieved by knocking against one of the end mirrors of the cavity[7]. This perturbation will start to modulate the main mode of the cavity so that side bands arise. The more sidebands become locked to the main mode, the higher will be the intensity of this wave package generated. Provided that the intensity of the package is high enough, it will change the refractive index of the crystal (see Eq. 2.22) so that the package is focussed and amplified even further. For wave packages which do not have a large number of modes, the Kerr-focussing is minimal and thus those packages aren't amplified further and therefore discarded.

[6]In a cw laser the bandwidth is only determined by the natural bandwidth and other bandwidth broadening effects like the Doppler effect.

[7]In fact, mode locking was discovered by accident as one day one laser experimenter hit his laser setup which initiated mode locking.

Cavity dumping

As already mentioned, cavity dumping is a technique used to increase the pulse energy of the oscillator by almost a magnitude. The idea behind the concept of cavity dumping is to let a wave package run within the oscillator until it has accumulated enough energy. The dumping is performed by a Bragg crystal where the laser beam is diffracted. This is realized through acoustically induced optical grating which means that the refractive index of the crystal is spatially modulated. The crystal is mounted on a piezo which is fed by an external RF source (microprocessor-controlled driving unit from *APE Berlin* which controls the whole cavity dumping). Thus the laser pulse is coupled out of the oscillator every time the acoustic wave is turned on. The cavity dumping is feedback controlled, this means that a fast photodiode is employed to synchronize the driving unit with the repetition rate of the laser. For (fine) tuning, the driving unit allows to set the *phase*, *time delay*, *dumping rate* and *power output for the RF signal*. Since only every 50th pulse is dumped out of the cavity, the repetition rate is reduced compared to normal oscillator mode (1.52 MHz vs. 76 MHz). Other methods to increase the pulse energies are *single pulse amplifying* and *regenerative amplifying*. The former allow to keep the original repetition rate of the normal oscillator mode but since each single pulse has only a limited time[8] to accumulate energy, the pulse energies are lower compared to the cavity dumping technique we employ. On the other hand, regenerative amplifying allows high amplification of pulse energies with the caveat of a heavily reduced repetition rates since the pulses remain in the amplifying cavity for a long time before being dumped[9]. We chose *cavity dumping* since we wanted to have increased pulse energies to maximize the pump-induced effects (which are proportional to the pulse energy of the pump beam) but not as high as we could achieve with regenerative amplifiers since there would be risk of ablation (thermal destruction of the films). Single pulse amplifying would not yield high enough pulse energies and additionally the high repetition rates would risk the quick destruction of the films due to heat accumulation.

2.4.2 Chopper and lock-in amplifier

The chopper, photon counter and lock-in amplifier are essential parts of our pump-probe setup. The chopper operates at a frequency of approximately 450 Hz and modulates the pump beam and is necessary for the measurement of the pump-induced signal. The setup works as follows (see Fig. 2.9): The chopper generates a rectangular output signal which is synchronized to

[8] In single pulse amplifying systems, each single pulse runs through a second cavity and has only the time span between two pulses for amplification.

[9] In fact, regenerative amplifiers stretch the pulses, couple them into a cavity, dump the pulse once the pulse energies are high enough, then compress the pulses again. Thus it is obvious why the repetition rate is reduced so much.

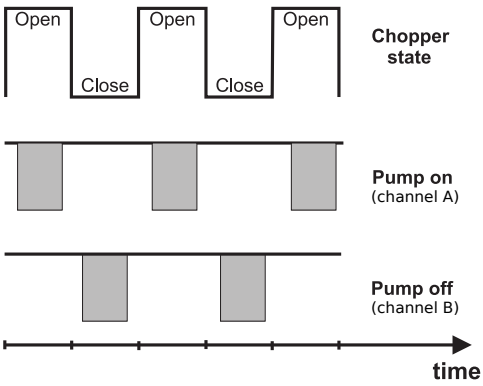

Figure 2.9: Schematic view of the chopper states on the time axis (upper part). The two lower parts show the time frames when the signal is measured for pump on and off. These time frames are shorter than the states of the chopper when it's open or closed. This makes sure that the chopper is always fully open or closed respectively when measuring the probe signal. The divisions on the time scale correspond to $1/f_{chopper}$.

its operation frequency. This signal is fed both to the photon counter (to measure the SHG signal) and to the lock-in amplifier (to measure the fundamental signal). The photon counter has two channels, one which counts the photons for the chopper state *open* and one for *closed*. The phase of the input signal from the chopper to the photon counter is adjusted such that the photon counter channel for *pump closed* (channel B) matches the rectangular output signal *low* and the channel for *pump open* (channel A) matches the *high* signal. Thus the photon counter is synchronized to the chopper and counts the states *chopper open* and *chopper closed* in the proper channels. The pump-induced effects are then proportional to:

$$\Delta_{even} \propto \sqrt{\frac{A}{B}} - 1 \tag{2.23}$$

To measure the fundamental, a photodiode is used which connects to a separate lock-in amplifier over a home-made amplification stage which consists of a fast (channel C) and slow (channel D) channel. The slow channel measures the average signal of the photodiode while the fast channel measures the fluctuating signal for chopper states *open* and *closed*. The former is fed into an analog-digital converter and the latter into the lock-in which suppresses the DC-part (average signal). The relative linear reflectivity is then obtained with:

$$\frac{\Delta R}{R} \propto \frac{C}{D} \tag{2.24}$$

2.4.3 Sample holder and magnet

To position the sample in the laser beam-path, a custom sample holder was designed (see fig. A.6, appendix A). It consists of an aluminum holder which has a molybdenum clamp mounted to it. The design was derived from the Omicron-brand sample holders which were used in the UHV chamber for sample preparation and analysis (see fig. 3.4, chapter 3). The sample itself is located inside two pairs of Helmholtz coils which produce a magnetic field in the plane of the sample and thus the thin films (see fig. 2.10). This is the external field necessary to produce the magnetization in the ferromagnetic films to yield spin-polarized electrons upon excitation. The Helmholtz configuration yields homogeneous fields and was therefore chosen for these experiments. The idea of using two nested Helmholtz pairs was to be able to produce magnetic fields both in transversal and longitudinal geometry regarding the sample surface. As we will learn later, measuring magnetic SHG requires the field to be transversal, measuring MOKE requires longitudinal configuration. The coils are custom-made, they were designed using a CAD-software and then handcrafted by the precision-engineering group of the department. Construction schematics can be found in the appendix.

All measurements were performed with fields high enough to saturate the magnetization of the ferromagnetic films.

2.5 Calibration of the magnet

Since the magnet is a home-made construction, before actually using it, we wanted to test whether it would satisfy our requirements to produce the external magnetic field to induce magnetization in the ferromagnetic layers of the samples. Furthermore, since we are driving the magnet with remote-controlled power supply, we only know the current through the coils but not the actual field. Thus, we have to calibrate the magnet to be able to match the field with the current set by the power supply. The specifications of the magnet are listed in Tab. 2.1.

Parameter	**Inner Coil Pair**	**Outer Coil Pair**
Number of Windings	75	120
Electrical Resistance	$1.641 \pm 0.278\ \Omega$	$4.469 \pm 0.089\ \Omega$
Radius	0.038 ± 0.002 m	0.068 ± 0.002 m

Table 2.1: Specifications of the two home-made Helmholtz magnets

We used a hall detector to measure the field of the operating magnet at various currents. Then we calculated the theoretical fields for both coils in

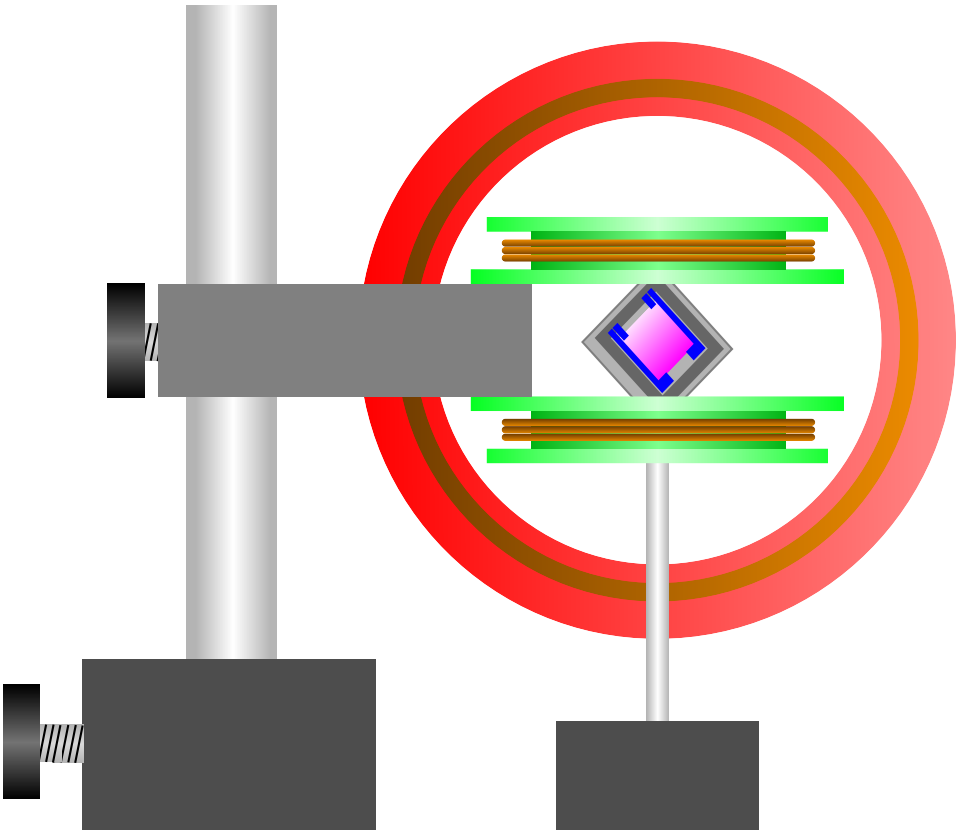

Figure 2.10: Schematic view of the dual nested Helmholtz setup used to produce two perpendicular magnetic fields in the sample plane. The coil-reels are given in red and green color (outer and inner pair). The sample is mounted onto a plate which has an omicron-clamp mounted to it (see Fig. 3.4). The coils (orange) are held in fixed position, while the sample-holder can be translated along all three axes. Note that the sample-plane is actually rotated by 90 degrees with respect to the outer coils' plane. The sample itself is colored purple.

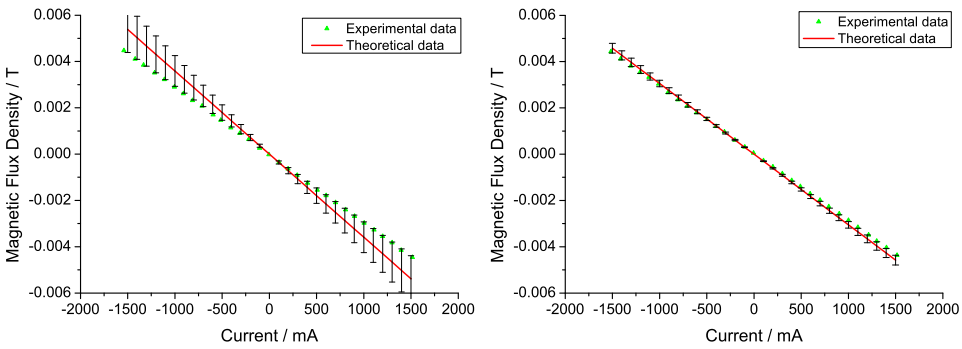

(a) Inner coil (b) Outer coil

Figure 2.11: Comparision of the experimental data measured with a hall detector and theoretical data determined from the coils parameters (diameter, coil spacing, number of windings). Current varies from -1500 to 1500 mA.

the Helmholtz configuration. It is known from standard literature, that for a Helmholtz configuration the field along the axis adjoining the coils of a Helmholtz pair, in the center is:

$$B = \mu_0 \times \frac{8 \times I \times N}{\sqrt{125} \times R} \tag{2.25}$$

with μ_0 being the permeability of the vacuum, N the number of windings per coil, I the current through the coils and R the radius of the coils. In perfect Helmholtz configuration, the spacing of the coils matches the radius of the coils, thus R.

The calibration data is shown in Figure 2.11. The plots show that the magnetic flux densities measured with the hall detector match nicely with the theoretical values calculated from the coil parameters in Table 2.1. Thus the magnet is ready for the actual measurements and we are always able to determine the exact flux density from the current displayed on the power supply. From the plots in Figure 2.11, we read the following calibration:

- Inner coils: 1 Ampere $\equiv$ 35 Gauss
- Outer coils: 1 Ampere $\equiv$ 30 Gauss

2.5.1 LabView evaluation software

Since the measurement results are always subject to fluctuations due to variations in the optical alignment, external influences (temperature, humidity, etc), we are performing several iterations of the same scans to reduce the statistical noise. As one single measurement can already take quite long to

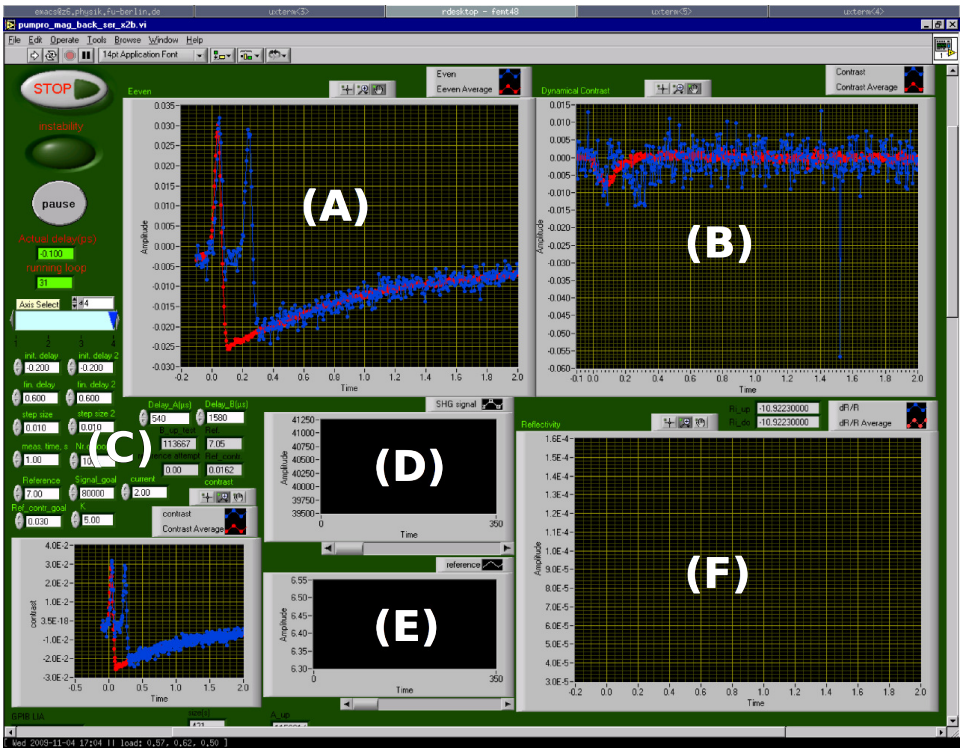

Figure 2.12: Screenshot of the main program used for our SHG measurements. The pump-induced effects are measured with the graph instrument (**A**), the transient contrast with (**B**). All parameters (scan range and resolution for pump-probe delay, minimum signal, minimum contrast in the reference channel, current for the coils, measurement times per step and chopper parameters) can be set with the edit boxes in (**C**). The graphs in (**D**) and (**E**) measure the plain SHG intensity and the SHG signal in the reference channel (BBO crystal). Graph (**F**) measures the linear reflectivity (see section 2.3.1).

finish[10], the measurement progress is completely automated and controlled with a program written in *LabView*. Thus long measurements can run completely unattended, only occasional checks of the alignment are naturally necessary. The program controls the delay stage, the magnet and keeps track of all measured parameters in several virtual instruments on its interface as seen in Figure 2.12.

Furthermore, the software counter-checks the measured SHG signal with a reference to make sure the optical alignment of the laser still yields output

[10]Scanning from −0.2 ps to 5.0 ps delay with 0.01 steps, for example, will take around 1200 seconds or 20 minutes (1 second each for measuring at each direction of the magnetic field and some time is required to move the delay stage further), running 10 loops for the statistics will take about 3 hours.

with high enough intensities[11]. If the SHG signal in the reference channel or in the actual measured SHG channel is too low, the software discards that datapoint and tries to measure it again. This makes sure that only data with proper alignment is recorded and all changes in the signal are only due to real effects in the sample and not due to some external fluctuations. Of course, there is some small tolerance for variations of the output signal but those are covered by the statistics and will not distort our data.

Internally, the program also performs the necessary computations of the input data so that the data stored on disk is ready for further analysis with additional software like *Origin* (i.e. pump-probe delay is calculated in picoseconds, intensities are for the pump-induced effects and transient contrast are calculated as relative changes, data is averaged, etc.). Other custom Labview programs include some to determine the cross correlation to setup the proper overlap and measure hysteresis loops of ferromagnetic films.

[11] Usually the phase of the cavity dumping shifts away during longer measurements which results in reduced power.

Chapter 3

Sample Preparation

The quality of the samples has key importance for our experiments. Previous experiments in [19] have shown that the intensity of the SHG signal depends on the topography of the surface, rough surfaces usually yield higher signals. On the contrary, impurities as well as high corrugations may cause unwanted scattering of the laser beams which can deteriorate the shape of the signal or impede finding the overlap in the pump-probe setup. Therefore we wanted to be able to control the topology of the surface from the evaporation and with possible additional treatments like sputtering to achieve surfaces which yield high intensity signals in the optical measurements with highest possible reproduceability. In order to achieve high purity, the samples were prepared in a ultra high vacuum (UHV, less than 10^{-9} Torr), after the substrates had been cleaned in an ultra sonic bath with various organic solvents and water. The whole process of preparing samples in UHV and depositing thin films using evaporators is usually referred to as *Molecular Beam Epitaxy* (MBE). Since our group does not possess such an MBE chamber, the group of Professor Fumagalli kindly granted us access to their setup which is illustrated in figure 3.1. The setup is very typical and reflects the common setup described in [20].

Topography analysis is performed utilizing well developed and proven methods of surface examination like reflection high-energy electron diffraction (RHEED) and scanning tunneling microscopy (STM). While the RHEED analysis can be carried out *in-situ* (i.e. the measurements can be made during the evaporation process onto the substrate), the examination of the samples with STM require the transfer of the prepared samples into the analysis chamber (AC) where the STM is located together with other setups (AFM, LEED) for *ex-situ* surface analysis.

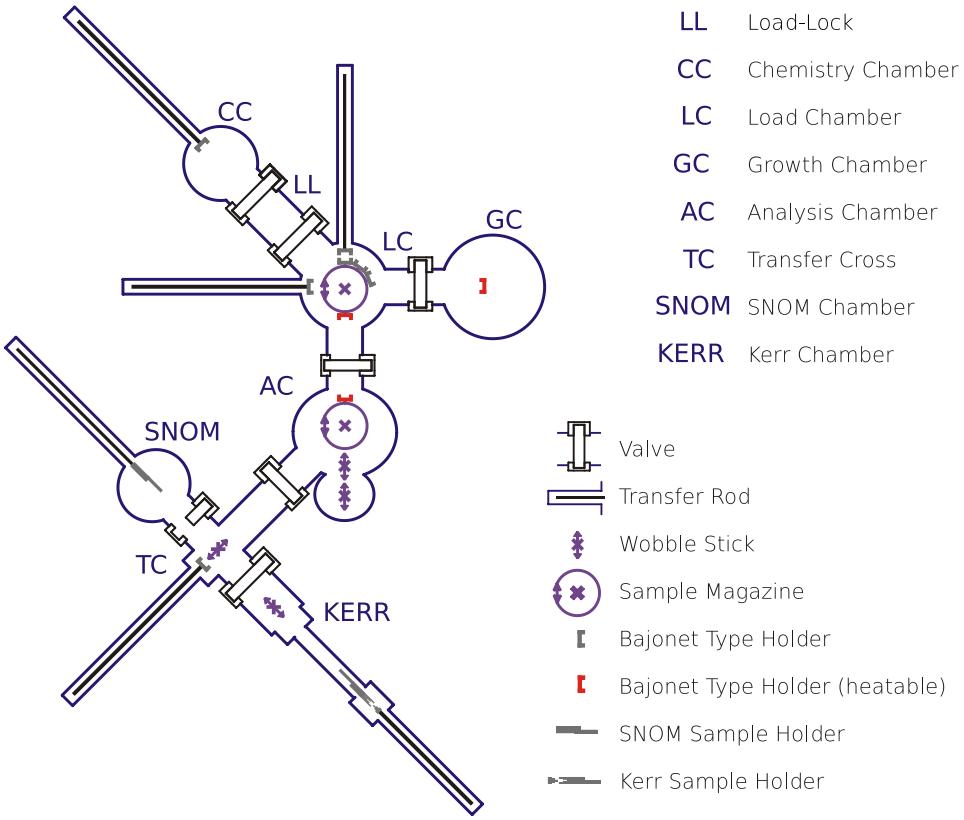

Figure 3.1: Schematic view of the MBE chamber used for sample preparation and quality analysis. The fresh MgO substrates are transferred into through the load lock (LL), then heated and annealed in the load chamber (LC). For film preparation they are transferred into the growth chamber (GC). All quality measurements of the films (STM, AES) are made in the analysis chamber (AC). RHEED pictures are taken *in-situ* in the growth chamber though. Figure courtesy diploma thesis Björn Lewitz [21].

3.1 Choice of substrates and film

The choice of materials of the model system for our experiments was made for several reasons. First, we needed a substrate which is transparent for the spectrum of our laser. Secondly we chose a substrate on which iron grows epitaxically. Studying previous works in [22], [23] and [24] we decided to use MgO(001) substrates. Fe grows in the [001]-direction with the Fe [100]-axis parallel to the MgO [110]-axis. As we will see later from our STM measurements, Fe shows a very small surface and interface roughness as also noted by Mühge et al. in [22].

The reason for the high quality of the Fe-films on MgO(001) is that the lattice constants of Fe along [100] and [001] match very nicely to that of MgO along the [110]-direction:

$$\begin{aligned} d_{\mathrm{Fe[100]}} &= 0.2866 \text{ nm}, \\ d_{\mathrm{MgO[110]}} &= 0.29817 \text{ nm}. \end{aligned}$$

This means that there is only low distortion of the Fe lattice, which was determined by Mühge at al. to be the following:

$$\begin{aligned} d_{\mathrm{Fe[100]}} &= (0.2859 \pm 0.0005) \text{ nm}, \\ d_{\mathrm{Fe[001]}} &= (0.2874 \pm 0.0003) \text{ nm}. \end{aligned} \tag{3.1}$$

Regarding the Au film, investigations were made by Rieckart et al. in [24]. They have shown that Au grows on MgO with the [100]-direction parallel to the [100]-direction of the substrate. However, LEED measurements showed that Au does not grow layer-by-layer but in forms of islands. Depositing a buffer layer of 1 nm Fe was the solution which allowed smooth and flat surfaces similar to Fe on MgO. Thus, the Fe on MgO does not only serve as a ferromagnetic layer in our experiments but also as a buffer layer to improve the epitaxy of the Au layer. Regarding Fe on Au (as we will need for the later spin transfer experiments), it is known from [25] and [26] for example, that Fe(001) grows in 45° rotation regarding Au(001), similar to Fe on MgO(001). Thus, in the sandwich configuration of MgO/Fe/Au/Fe, MgO(001) and Au(001) have parallel lattice alignments while the itinerant ferromagnetic Fe(100) are rotated by 45° with respect to MgO and Au.

3.2 Equipment for Evaporation

3.2.1 Electron Beam Evaporator

Before we commenced with the actual evaporation we had to decide what evaporators to use. For iron we chose an electron beam evaporator (EBE, Fig. 3.2) from Oxford Research, UK [27]. It evaporates rod material by targeting high energy electrons at it, allowing to evaporate high melting point materials at rates between $<$ 1 monolayer per minute to over 5 nm per minute. For first attempts we also evaporated gold with the same evaporator. However, since the amount of material which can be evaporated with the beam evaporator is limited for each load[1], we evaporated gold from a Knudsen-cell (see sec. 3.2.2) which can evaporate large amounts of (mid to high vapor pressure) materials.

A high-voltage potential of 2 kV is applied to the target rod in order to accelerate the electrons emitted from a dedicated filament which is held at ground potential. The control unit of the evaporator allows setting of both filament current (up to 6 A) and electron energy. Emission current must be maintained through these two parameters (it cannot be controlled directly). However, the control unit allows online check of *high voltage, filament current, emission current and ion flux* (a certain percentage of the vapor ionizes and can thus be measured as an anode current) and thus we could control emission all the time during evaporation.

Material can be loaded into four individual pockets, either as a rod (max. 2 mm diameter, 13.5 mm length) or in special crucibles. We tested rods of different diameters and different types of crucibles. Both crucibles and rods have benefits and drawbacks. Crucibles offer higher efficiency of the evaporation process than rods. While evaporation from a rod of 1.6 mm diameter yields films of up to 15 nm per pocket, the crucible allowed us to evaporate films thicker than 50 nm. The higher efficiency is a result of the smaller beam aperture as compared to the rod. As a result, there is less flaked evaporated material[2] within the pockets. On the other hand, however, we had problems with the thermal stability of the crucibles. At high emission currents we observed melting of the crucibles with the evaporation material which impedes the purity of the films deposited. The risk of melting can be avoided by using crucibles from a material with very low vapor pressure, i.e. tungsten. However, we did not have any such crucibles and producing them at the precision engineering department requires a setup for electrical discharge machining which was not available at that time. The crucibles

[1] Load here refers to the evaporator being filled with new evaporation material and being ready for evaporation. Loading the evaporator requires venting the UHV and detaching the evaporator from the chamber, a tedious process.

[2] Flaked material is weakly adhesive to the pocket walls and thus it may fall off easily. If this excess material is not removed periodically there is the risk of shorting the rods to ground, rendering the high-voltage and thus the whole evaporator useless.

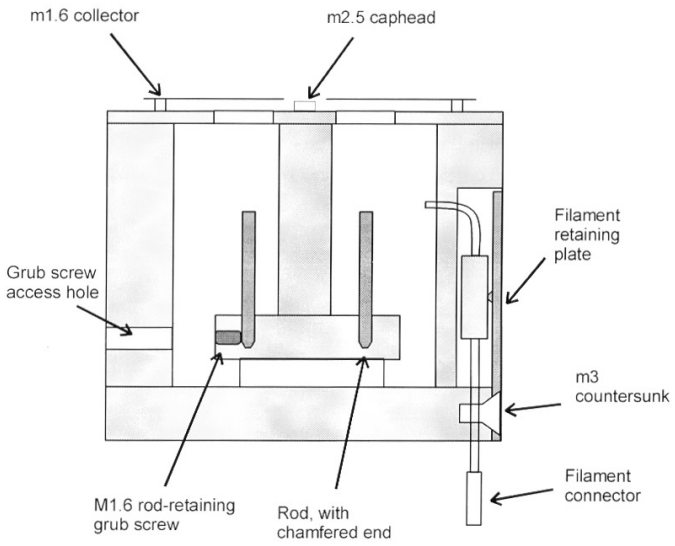

Figure 3.2: Electron Beam Evaporator, head assembly. The evaporation material is mounted as rods inside a copper assembly. Material may also be evaporated from 85 mm^3 crucibles which provide higher efficiency. The filaments are driven with currents up to 5 A allowing electron emission currents up to 100 mA. The electrons are accelerated through a high voltage of 2 kV. From the manual of Oxford mini e-beam evaporator [27].

that we tested were made from tantalum and molybdenum and were milled and drilled. To maintain the purity of the films and still be able to use high evaporation rates (i.e. high emission current) we chose rods over crucibles.

Prior to any evaporation, the unit and each of its individual pockets have to be degassed. First, we degassed the filaments by running them at up to $4 - 4.5$ A, the filament current which is used during evaporation (see tab. 3.1). While the filaments degas, background pressure will rise up to a lower 10^{-8} mbar range. Once the pressure has returned to the 10^{-10} regime, degassing of that pocket is complete.

After all four filaments have been degassed, the high voltage is set to maximum (2 kV) while the filaments are still off. Increasing the filament current triggers electron emission and thus electron bombardment of the target. When the emission current reading registers ≈2-5 mA, the target material and its turret or crucible will start to degas. This is registered by an increase of the measured ion flux and increase of the chamber pressure up to 10^{-7}. Once again, after a certain time-span (usually 10-20 minutes), degassing ceases when pressure is back to 10^{-10}.

The observed ion flux is determined by two effects:

- **Background ionization:** The background ionization results from the residual gas in the chamber and therefore depends on the chamber pressure. It causes the ion flux to rise as the emission current is increased, **instantly and linear with emission current**. After a longer period of evaporation, the contributed flux decreases as both the evaporator and the charge material will outgas even more.
- **Evaporation:** Once the emission current is high enough, evaporation starts which causes a drastic increase in ion flux. Since evaporation requires heating of the charge material, **the evaporation comes with an associated time lag**. When using crucibles, the observed delay is even longer and it may take 1-2 minutes until the ion flux due to evaporation can be measured after reaching the necessary emission current.

In case the background ionization rises too much which can be registered as a high flux of several micro amperes, the high voltage flashes over to ground potential. Since the delicate electronics of this particular electron beam evaporator model is poorly protected against such flash-overs, the glitch usually puts the micro controller of the control unit into a undefined state requiring a restart of the whole unit. Therefore a proper degassing and cooling of the evaporator was critical for reliable operation.

Since we needed to determine the exact evaporation rates in sensible physical units (thickness per time), a quartz micro balance (QMB, see section 3.2.3) was used for feedback during degassing and evaporation. The flux can be used as a coarse indicator to determine if there is any evaporation taking place and the flux approximately reflects to a certain rate on the QMB for identical materials and target configurations.

For the evaporation of iron, the following parameters had been found to deliver best results at highest stable rates:

Source	**Filament Curr.** A	**Electron Energy** kV	**Emission Curr.** mA
Rod (1.6 mm)	$4.2 - 5.0$	2	12
Rod (2.0 mm)	$4.4 - 5.0$	2	15
Ta-Crucible	$4.2 - 4.5$	2	$18 - 20$
Mo-Crucible	$4.3 - 4.5$	2	$30 - 35$

Table 3.1: EBE parameters for Fe/Au evaporation from rod/crucible.

3.2.2 High Temperature Cell

Although the electron beam evaporator is suitable for evaporation of even high melting point materials it has two significant disadvantages which are

its limited loading capacity and an upper limit for evaporation rates. Using crucibles to maximize efficiency, a charge of evaporation lasts up to 50 nm per pocket. However, since we wanted to grow thick gold films of up to 150 nm, we would have been subject to frequent refills of the pockets which requires the tedious process of opening the UHV chamber. Also, the limited rates make evaporation of thicker films uncomfortable and quite time-consuming.

For this reason, we were using a Knudsen-type, high-temperature effusion cell for the evaporation of gold. The name "high-temperature" indicates that even materials with relatively low partial pressures can be evaporated, but not tungsten contrary to the electron beam evaporator (3.2.1). The effusion cell consists of a self-supporting tungsten wire as heating system and an exchangeable 10 cm^3 crucible. A built-in thermocouple allows temperature feedback to its control unit.

Compared to the electron beam evaporator, operation of the high-temperature cell (HTC) is relatively simple: once the material is loaded, the chamber pumped to UHV conditions and the unit is degassed[3], we just need to set a temperature high enough for the evaporation material to reach a sufficient vapor pressure which is indicated by the rate registered on the QMB (Section 3.2.3).

The only concerning issue with the HTC is the choice of a proper crucible. There are several types available, made from different materials:

- Boron Nitride (PBN):

  pro: high thermal stability, low adhesivity of evaporation material

  contra: outgassing of nitrogen possible at high temperatures (above 1300 °C)

- Aluminium Oxide (Al_2O_3):

  pro: high thermal stability

  contra: outgassing of Al and O possible

- Tantalum (Ta):

  pro: no outgassing at lower and mid-range temperatures

  contra: evaporation material can melt into crucible at high temperatures, low thermal stability (risk of crucible-burst)

- Pyrolytic Graphite, Vitrious Carbon (C):

  pro: high thermal stability, allows very high temperatures

  contra: outgassing of carbon possible

[3]Degassing is performed analogous as for the electron beam evaporator. The unit is degassed at temperatures around the target temperatures until pressure has stabilized.

We have chosen a PBN crucible since an increased partial pressure of N_2 is not critical for the sample quality. It has a low sticking coefficient on metal surfaces, thus our metal films and also on the chamber walls. The latter meaning that N_2 can be pumped out very quickly.

3.2.3 Quartz Micro Balance

The quartz micro balance (QMB) is an essential measurement tool used in the evaporation processes. It allows accurate and independent[4] measurements of the film thicknesses and calculates the current evaporation rate by averaging the change of thickness over time. It is based on the works of Günther Sauerbrey in 1957 [28].

The balance consists of a small, oscillating ($f \approx 6$ MHz) quartz, shaped as a plate unlike most clock quartz crystals which have fork shapes and an oscillation frequency of 32.768 kHz (see Fig. 3.3). It is mounted inside the UHV chamber next to the sample holder so it is exposed to the evaporation beam as well. The films increase the mass of the oscillating plate which is detected as a drop of the oscillation frequency of the plate ($\omega = \sqrt{\frac{D}{m}}$). Frequency shifting of the quartz crystal due to deposited films which are thin compared to the thickness of the plate can be determined by considering the films as an increase of the thickness of the crystal plate.

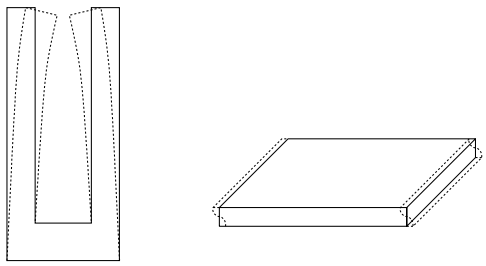

Figure 3.3: Various forms of quartz crystals. Left shows the fork shape used in most clock quartz crystals, right the plate shape employed for the quartz micro balances. The fundamental modes are indicated with dashed lines.

The fundamental frequency f_0 of such a crystal plate with thickness d_0 is:

$$f_0 = \frac{N}{d_0} \tag{3.2}$$

[4]The electron beam evaporator has some limited means of controlling the evaporation rate by means of measuring its ion flux. However the flux determined there is rather a coarse indicator since the background ionization contributes as well here. Thus the actual flux of metal ions is smaller than the value displayed.

where $N = 1670$ kHz mm, a material-dependant parameter which derives from the acoustic impedance Z of the material. Z incorporates the speed of transversal waves through the medium.

Evaporating a thin film will increase the thickness by $\Delta d \ll d_0$ and we can use the approximation $\frac{1}{1+x} \approx 1 - x$:

$$f = \frac{N}{d} = \frac{N}{d_0 + \Delta d} = \frac{N}{d_0} \frac{1}{1 + \frac{\Delta d}{d_0}} \approx f_0(1 - \frac{\Delta d}{d_0}) \tag{3.3}$$

However, internally the control unit of the balance determines the mass of the evaporated film, therefore the density of the evaporation material has to be programmed into the unit prior any evaporation process to eventually yield the actual thickness of the film from $d = \frac{Mass\ m}{Area\ A \times Density\ \rho}$.

As the balance is positioned next to the sample, the thicknesses determined vary from the actual thicknesses on the target substrate by a constant factor called the *Tooling Factor* [29]. This factor is programmed into the control unit of the balance during initial setup of the chamber. In order to increase the displayed accuracy of the balance, we have set the tooling factor to 1000, the maximum value[5]. The balance has been calibrated for both the electron beam evaporator (Fe evaporation) and the high temperature cell (Au evaporation) and thus the displayed values have to be multiplied by a different scaling factor each. Table 3.2 lists all parameters for the quartz micro balance for evaporation of Fe and Au.

Material	**Density** g cm^{-3}	**Impedance** 10^5/cm^2 s	**Scaling Factor**
Fe	7.86	25.30	0.1122
Au	19.30	23.18	0.2375

Table 3.2: QMB parameters for evaporation of Fe/Au films.

During evaporation of the wedges, the deposited thicknesses were logged regularly to keep track of the evaporation processes. When growing a wedge, the translation of the shutter is performed once a certain intermediate thickness has been reached (vertical step size of the wedge terraces).

3.3 Cleaning the Substrates

Our samples are based on single-crystalline substrates of Magnesium Oxide (MgO) in (001) orientation. They fit into the Omicron-brand sample holders (see figure 3.4) and have the dimensions $10 \times 10 \times 0.5$ mm^3. Furthermore

[5]By setting the tooling factor to 1000, the QMB displays an additional digit for both rate and thickness.

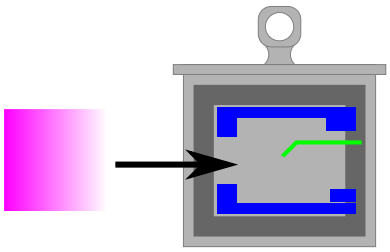

Figure 3.4: Omicron sample plate. The MgO substrates (purple) are put into the sample plate which fit into the 2-inch sample holders (Fig. 3.5) and are fixed with molybdenum clamps (blue). They can be grasped at the tag on the top with pincer grip wobblestick in order to be pulled out of the 2-inch holder in the UHV chamber and then transferred into the STM for further analysis for example. A sample carousel allows temporary storage of up to 8 sample plates. An additional tantalum needle (green) which point-contacted the substrate was welded to the sample plate to make sure there was an electrical contact between the evaporated film and the sample holder.

they are polished on both sides by the manufacturer. As one aspect, only a polished surface will allow the thin films to grow with high symmetry and coherence lengths. On the other hand, a polished surface on the backside of the sample is necessary to reduce optical scattering in the laser experiments.

Before we could transfer the samples into the UHV-chamber for film evaporation they needed be cleaned thoroughly, both chemically and by degassing through heating. As noted by Blomqvist et al. in [30] for example, the best possible results are achieved by cleaning the MgO substrates in an ultrasonic bath of acetone, isopropyl alcohol, ethanol for 10 minutes each. To remove any chemical residuals (*Carbon* !), in this case we also rinsed the substrates for another 5 minutes in deionized and highly cleaned water with ultrasonic cleansing. Since Magnesium Oxide is highly hygroscopic, the last bath must not last too long and the substrates are to be dried immediately with gaseous nitrogen. In order to prevent any contamination of the now clean substrates they were handled with ceramic tweezers instead of metallic ones and latex gloves[6].

After cleaning the substrates chemically they were ready to be transferred into the UHV chamber for MBE and analysis. Since fully opening the chamber requires a venting of the vacuum to ambient pressure and, after installing the samples, a time-consuming and tedious (multi-staged pumping and bake-out) restoring of the vacuum, the samples are transferred into the UHV through a load lock. The lock is usually a very small chamber whose pressure can be restored to a good vacuum within a few hours after opening

[6]In fact, during the sample preparation metallic tweezers were accidentally used once. AES spectra taken of these samples clearly showed contamination with nickel.

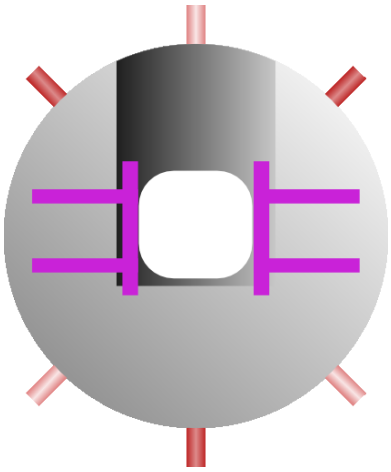

Figure 3.5: Illustration of the 2-inch sample holders used for transfer within the UHV chambers. The round plate has 6 mounting bolts, 3 of each along one perimeter circle (at $0°, \pm 135°$ and $180°, \pm 45°$), allowing the plate to be mounted onto the transfer rods and stationary holders in each chamber with a bayonet-type connector. The holder is put onto or picked up from a stationary holder by sliding the rod into it and twisting the rod grip to lock or unlock the 2-inch holder from the rod or the stationary holder and vice versa.

for loading. From the load lock the samples can be transferred throughout the whole UHV chamber using transfer rods (figure 3.1) which grasp the samples with 2-inch sample holders of molybdenum (see figure 3.5).

The purity of the substrates was checked with AES analysis before evaporating the thin films. Figure 3.6 shows the effectiveness of degassing and annealing the substrates. The carbon peak shows a remarkable drop in intensity proving that we were able to get rid of at least half of the carbon on the substrate. However, since there is also some carbon in the bulk of the crystal which ascends to the crystal surface while heating the sample, there will be still carbon visible in the spectrum.

Therefore we concluded that with the methods employed in this work (chemical cleansing, outgassing and annealing), a clean and perfect surface could not be achieved. For perfect results, the MgO substrate needs to be sputtered with appropriate methods, more precisely one needs *low-energy sputtering* with a plasma source [7]. In [24] Rieckart et al. have presented the use of such a source with which they were able to get rid of the carbon contamination below the sensitivity of AES analysis. We have taken owner-

[7] Conventional sputter guns do not allow low-energy sputtering with insulators like MgO since the sputtering ions charge the target which will deflect most of the ions effectively. This plasma source compensates the total charge by shooting additional electrons to the target.

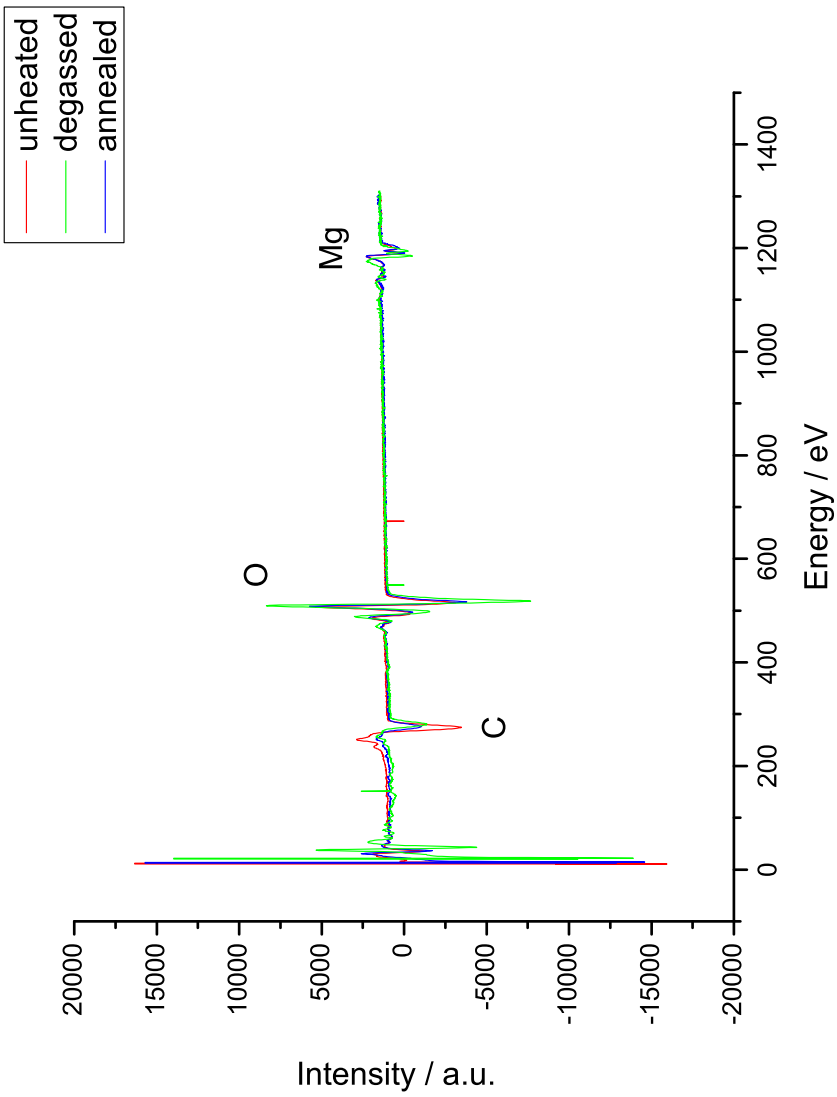

Figure 3.6: AES spectra of MgO(001)-substrates showing the effectiveness of degassing and annealing. The spectra were taken directly after transferring the substrates into the UHV (*unheated*), after being degassed for 12 hours at 100 °C (*degassed*) and after annealing (*annealed*) at 700 °C for 180 minutes. A remarkable drop of the intensity of the carbon peak at around 300 eV is detected after degassing and annealing respectively.

ship of the plasma source, its sophisticated setup and calibration, however, would go beyond the scope of this diploma thesis and therefore its use is subject to future works in this project.

3.4 Evaporation Process

The evaporation processes of iron and gold can be concluded as follows.

3.4.1 Evaporation of Iron Films

After cleaning, outgassing and annealing the samples, they were transfered into the growth chamber. The sample holder in the chamber was faced away from the evaporators while the electron beam evaporator with its shutter closed was running up. The parameters for the evaporator were set according to Table 3.1, then after the flux had stabilized the shutter of the electron beam evaporator (EBE) was opened and the rate was checked with the QMB which was set to the parameters for iron (3.2). When the designated evaporation rate was gained, the shutter of the EBE was closed again and the sample was faced downwards to the evaporators. The shutter to cover the sample (Fig. 3.7) was moved in and positioned over sample as necessary. The EBE shutter was opened again and evaporation starts and is registered with the QMB. Once the target thickness has been reached, the EBE shutter is closed again and the EBE is shutdown afterwards.

3.4.2 Evaporation of Gold Films

The process of gold evaporation was similar to that for iron. First turn the sample holder away from the evaporators, then close the shutter of the high temperature cell (HTC) and heat up the cell to 1350-1400°C. Then the shutter of the HTC was opened and the rate was checked with the QMB. If necessary, the temperature of the HTC was tuned until the designated rate on the QMB was read. Then the HTC shutter was closed again and the sample was brought into position as well as the sample shutter. Upon opening the HTC shutter, evaporation starts immediately but the QMB takes a few seconds until it reaches thermal equilibrium (the heat from the HTC produces false readings on the QMB since the crystal is out of thermal equilibrium).

3.5 Thin Films with Gradient Thickness

One goal of our measurements was to determine the exact mean free path of the ballistic electrons travelling through the gold films and to determine the optimum thickness for the iron film in order to achieve the highest possible efficiency in electron injection.

One could now prepare films with various thicknesses, measure the values of the aforementioned parameters for these and determine their optimal values by means of data evaluation methods like interpolation. Since the preparation of several samples is very time-consuming[8] and the conditions for each sample and measurement may vary[9], we are taking a different approach for these measurements: films with gradient thicknesses (wedges).

The process of evaporation can be seen analogous to the process of exposition of photographic paper towards a light source. The longer the exposition time of the photographic paper, the darker the exposed areas will be. In the case of Molecular Beam Epitaxy (MBE), the film thickness grows with exposition time. Thus in order to achieve a gradient of thickness along one lateral axis of the film, we would have to start exposing only one part of the sample, covering the rest of it with a shutter, then translate the shutter along the desired axis to expose more area to the evaporation beam over the time. The area which was exposed from the beginning of the evaporation process will naturally gain the highest thickness whereas the one exposed at last will have thinnest. One can also start with a completely exposed sample and then gradually close the shutter over the sample. This technique has the advantage that we can directly read the current thickness off the quartz micro balance during evaporation. Performing it vice versa, i.e. opening the sample gradually, means that we have to substract the current thickness measured off the QMB from the total thickness in the end to determine the thickness of the wedge at a specific point. We therefore favored closing the shutter gradually. Moreover, since the sample holder in the UHV chamber has more degrees of freedom than the shutter and since the latter extends into the chamber in an uncomfortable angle, we decided to keep the shutter fixed and move the sample holder instead.

For this specific task a custom shutter was designed and handcrafted from high-grade steel[10]. The shutter has to serve two tasks. First it must be able to cover the whole substrate so that a gradient thickness of the film can be grown along the full size of the substrate, and secondly, it must be able to cover an area of the substrate during evaporation permanently. This was necessary to achieve a region with small thicknesses at the verge of the substrate while we can still grow the gradient film on the remaining area of the substrate. The thin verge is required for optical adjustments in the laser setup later on: the pump and the probe-beam have to be aligned to meet in

[8]Remember that the amount of evaporation material like iron is limited in the evaporators. Only a few films can be prepared until the the evaporators have to be refilled which requires the UHV chamber to be opened.

[9]Varying conditions are slightly different substrates, ambient temperatures, contaminations, alignments of the optical setup etc.

[10]Materials for constructions of UHV parts must be carefully chosen. Metals like aluminum have the property to degas atoms from their bulk and may thus deteriorate the vacuum in the chamber. High-grade steel is in most cases the best choice, in fact, the chamber itself is made from it.

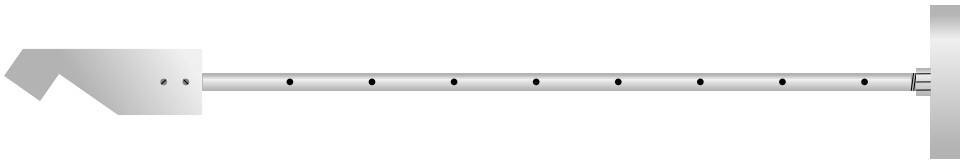

Figure 3.7: Schematical sketch of the shutter constructed for sample preparation. The arm is made from a high-grade steel tube (length: 350 mm, diam.: 8 mm) with vent holes. The sail is made from an iron sheet which was cut with a mill and mounted with two screws to the arm. A blind flange was chosen to mount the shutter to a translation stage to the MBE chamber.

one spot which is only possible as long the transmission of the beam through the film is high enough (i.e. finding the overlap and thus cross correlation signal).

The shutter consists of an iron tube (length: 350 mm, diameter: 8 mm) with vent holes which is mounted onto a blind flange (see Fig. 3.7). A tube was chosen in favor over a solid arm to reduce the risk of dead volumes which cannot be pumped properly and may deteriorate the vacuum continuously. The flange itself is mounted to a translation stage which is mounted to a 63 mm flange onto the chamber, coming in a angle of 35° regarding to the front flange of the chamber. Since the manipulator holding the substrate is located at an angle of 180° towards the front flange, the shutter sail had to be cut respectively. Figure 3.8 shows a photograph with the shutter sail covering the sample holder, taken with a CCD camera outside the chamber.

In order to achieve a linear gradient in thickness for a given start and end value, sample and shutter either have to be translated with respect to each other at a constant speed which depends on the evaporation rate and the total length of the gradient on the sample. Or, what we eventually favored, one keeps track of the current thickness with the help of the QMB (Sec. 3.2.3) and translates the shutter[11] each time a predefined thickness step has been evaporated. This choice was made since during the several cycles of evaporations we have performed, it showed that the rate of the evaporators regularly varied by up to half a magnitude from time to time, so that the choice of fixed time intervals would mean that we get non-uniform step sizes and therefore a bad linearity in the wedge.

Since the dimensions of the MgO substrates were 10×10 millimeters and we evaporated the wedge along the diagonal axis, the length of the projection of the wedge on the substrate is $10 \times \sqrt{2} \approx 14$ millimeters. We wanted to evaporate with the smallest sensible step size, this yields the

[11] In fact, we kept the shutter at a fixed position and moved the sample holder with respect to the shutter. Moving the sample holder allows to use more than one degree of freedom for sample movement (see Fig. 3.8).

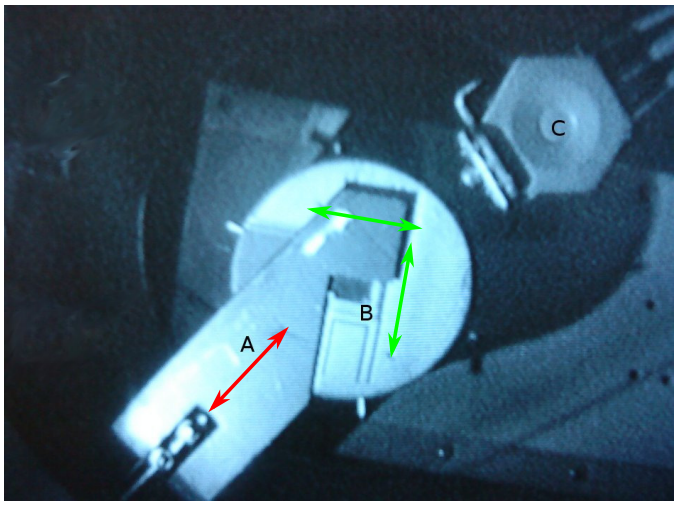

Figure 3.8: Live shot from the CCD camera through the bottom window in the growth chamber. It shows the shutter (A), the sample-holder (B) and the quartz-micro-balance (C). Green and red arrows indicate degrees of freedom of sample holder and shutter respectively.

smoothest possible gradient: one mono-atomic layer, i.e. 3 Ångstrøms or 0.3 nanometers.

Let's assume an end thickness of 50 nm for example, then we get for the number of steps,

$$n_{steps} = \frac{\mathrm{d}_{total}}{\text{step size}} = \frac{50 \text{ nm}}{0.3 \text{ nm}} \approx 167 \tag{3.4}$$

since the lateral length of the wedge is 14 mm, we have to translate the shutter by ≈ 0.08 mm each time

$$\frac{14 \text{ mm}}{167 \text{ steps}} \approx 0.08 \ \frac{\text{mm}}{\text{step}} \tag{3.5}$$

For a convenient operation of the shutter, we chose 0.10 mm per step.

The evaporation rate was chosen such that the pressure in the chamber would not deteriorate too much but still a rate is achieved which allows to grow the wedge within a reasonable amount of time with a comfortable step rate for the shutter translation[12].

The evaporation rate for gold was empirically set to ≈ 0.1 Å s^{-1}. At this rate, the pressure will not rise above $\approx$ 1-2 $\times 10^{-8}$ mbars during evaporation.

[12]The step rate here refers to the time interval after which the shutter or sample are manually translated with respect to each other.

So, assuming a constant rate during evaporation, the total duration of the process will be:

$$t_{total} = \frac{\mathrm{d}_{total}}{\text{rate}} = \frac{50 \text{ nm}}{0.01 \text{ nm}} = 5000 \text{ s} \tag{3.6}$$

and the shutter will have to be moved each

$$t_{interval} = \frac{\text{step size}}{\text{rate}} = \frac{0.3 \text{ nm}}{0.01 \text{ nm s}^{-1}} = 30 \text{ s} \tag{3.7}$$

3.6 Examination of the Sample Quality

The samples are analyzed both in real space (STM) as well as in reciprocal space (RHEED). Real space analysis allows to check the surface for local defects as well investigate corrugations and determine the actual dimensions. Reciprocal space tells us about the periodicity over large scales and gives a principal idea about the surface geometry.

3.6.1 RHEED Analysis

RHEED stands for *Reflection High Energy Electron Diffraction*. Thus electrons with high kinetic energy (5 to 50 keV) are diffracted in reflection at the sample surface.

Basics of RHEED

In contrast to LEED (*Low Energy Electron Diffraction*), electrons are accelerated to high kinetic energies of up 50 keV and hit the target in a small gracing angle (0.1°-4°). The diffracted beam is reflected to an adjacent fluorescent screen where the diffraction pattern can be seen. A CCD camera located behind the screen connected to a computer allows to take shots of the pattern to analyze intensities and lattice constants. The principal setup can be seen in figure 3.9, (a).

To understand why diffraction occurs and to be able to interpret the observed pattern, one uses the concept of the reciprocal lattice, reciprocal lattice vectors and the Ewald sphere (see Fig. 3.9 (b)). The reciprocal wavelength $\frac{1}{\lambda}$ of the wave vector of the incident beam defines the radius k of the Ewald sphere in the reciprocal lattice:

$$k = \frac{2\pi}{\lambda} \tag{3.8}$$

Thus, if one varies the energy (and therefore the wavelength λ) of the electron beam, the radius of the Ewald sphere will change anti-proportionally to it. This is helpful to tune the amount of spots visible on the screen, the larger the radius the larger will the solid angle of the sphere be and thus the

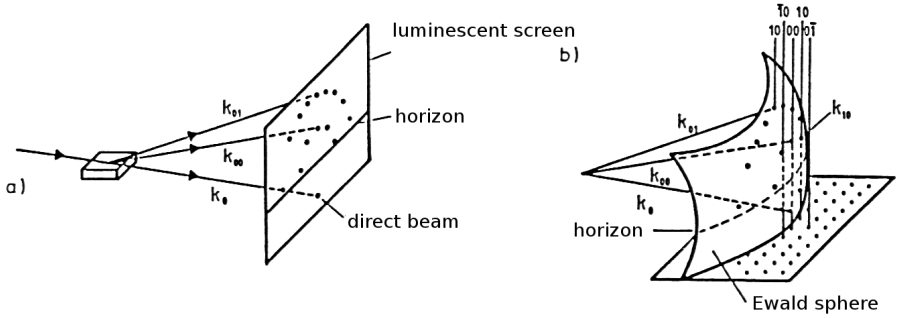

Figure 3.9: A high-energy electron beam hits the sample in a small gracing angle. Electrons are diffracted elastically and hit a luminescent screen. The direct beam is not visible on the screen as it lies below the horizon defined by the sample's shadow (a). The diffraction pattern can be constructed with the help of the Ewald sphere (b). Constructive interference occurs only when the rods indicating the allowed momentum vectors of the incident beam intersect with the Ewald sphere. Figure taken from M. Henzler, *Oberflächenphysik des Festkörpers* [32].

number of spots on the projected area. Now, if two points of the reciprocal lattice lie on the surface of the Ewald sphere,

$$\mathbf{K} = \mathbf{k}' - \mathbf{k} \tag{3.9}$$

the requirements for diffraction are met and reflected spots can be observed on the screen. Figure 3.10 shows the picture of the Ewald sphere in reciprocal lattice, indicating the two vectors (incident and diffracted beam and the the reciprocal lattice vector $\mathbf{K}$). Technically speaking, this means that the incident has the proper momentum and angle of incidence so that constructive interference between several elastically scattered beams occurs.

The striking advantage of RHEED over LEED is the geometrical setup where the electrons streak the sample parallel to its surface. Access to the sample in perpendicular direction is therefore still possible and one can evaporate films onto the sample while performing RHEED analysis. Since the perpendicular component of the electron beam energy is very small (a few hundreds eV: for 50 keV and 0.5° one gets $E = \sin(0.5° * 50 \text{ keV} \approx 436\ eV$), the overall electron energy has to be very high compared to LEED to achieve the effectively same energy of incidence.

We used a *Createc HP4* RHEED system. The HP4 is an advanced apparatus which is specially designed as a *in-situ* characterization tool in MBE analysis for studying growth rates and growth dynamics by measuring RHEED intensity oscillations. The system consists of the RHEED gun which is mounted to the MBE chamber (see Fig. 3.1), a power supply

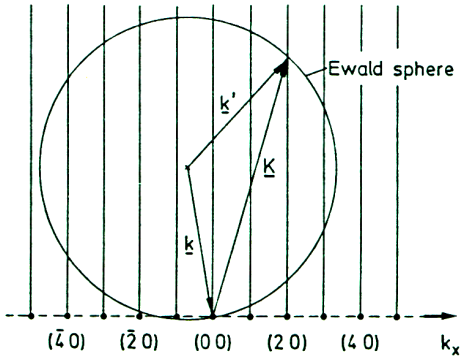

Figure 3.10: Ewald sphere in a two-dimensional reciprocal lattice. The sphere is a helpful construction to understand why diffraction occurs in a crystal lattice. Its radius is defined by the incident wave wector **k**. Constructive interference takes place if the both the diffracted beam end on a lattice point or if two lattice point lie on the perimeter of the Ewald sphere. Both equals that both vectors satisfy Equation 3.9. Figure taken from H. Lüth, *Surfaces and Interfaces of Solid Materials* [20].

and a control unit for the magnetic lens and electrostatic deflection system. The power supply allows energies up to 50 keV and beam currents of up to 100 μA. The lens and deflection system is directly integrated into the RHEED gun, the magnetic lens focuses the beam on the luminescent screen while the electrostatic deflection system positions the beam. Table 3.3 lists the beam parameters used for our RHEED measurements. Settings for the lens and deflection system change for every single measurement and have to be adjusted anew every time by tuning the pattern to best possible contrast and visibility.

Parameter	Setting
High voltage / kV	50
Filament Current / A	2
Emission Current / μA	$35 - 40$

Table 3.3: RHEED parameters used for our measurements.

Interpretation of RHEED images

In the case of an atomically flat and highly symmetric surface, the diffraction pattern shows bright, highly focussed spots which lie on different circles representing the different order of diffraction (*Laue circles*, see Fig. 3.11). However, in most cases the symmetry of the surface is violated so that the

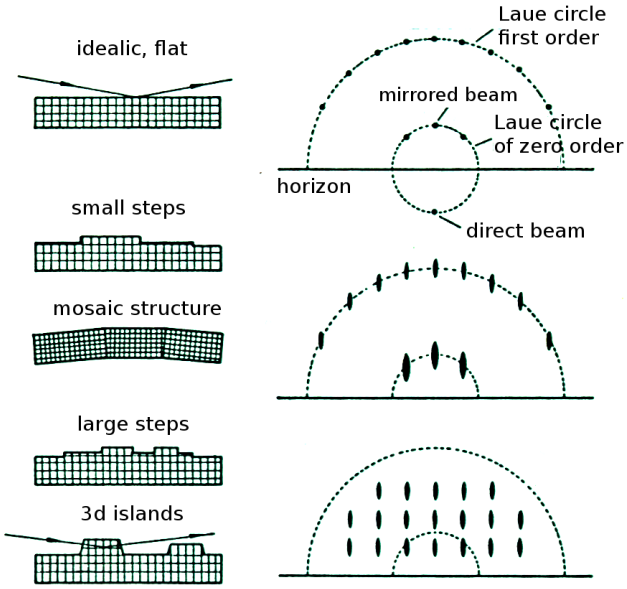

Figure 3.11: The morphology of the surface determines the pattern which can be observed on the luminescent screen during a RHEED measurement. An ideal, flat surface with high symmetry shows a pattern with sharp spots which lie on Laue circles. Small steps or a mosaic structure wash the spots out. If the surface consists of large, more or less regular steps (i.e. islands), the spots do not lie on the Laue circles anymore but instead form a regular, rectangular pattern. Figure taken from M. Henzler, *Oberflächenphysik des Festkörpers* [32].

observed pattern differs from that of an ideal surface. If there are small steps, or areas of the surface are slightly tilted (*mosaic structure*), the spots have elliptical shapes and less intensity. In the sense of the Ewald sphere, this means that the rods which intersect the sphere have a non-zero thickness.

RHEED Images

We measured Fe on MgO(001) films at electron energies of 50 keV, captured the luminescent screen with a CCD camera and analyzed the images with the software *Specs Safire 4* [31].

Figure 3.12 shows two RHEED images, taken at a relative azimuthal angle of 45°. The images are distorted in their geometry but the patterns suggest that the surface has islands according to [32]. Looking at figure 3.13 which is another RHEED image of Fe on MgO(001) at an inital azimuthal angle, one can see that there are actually two diffraction patterns, from Fig. 3.11 we concluded that this compound RHEED image can only be explained when considering the surface to be a crystalline structure (which creates the

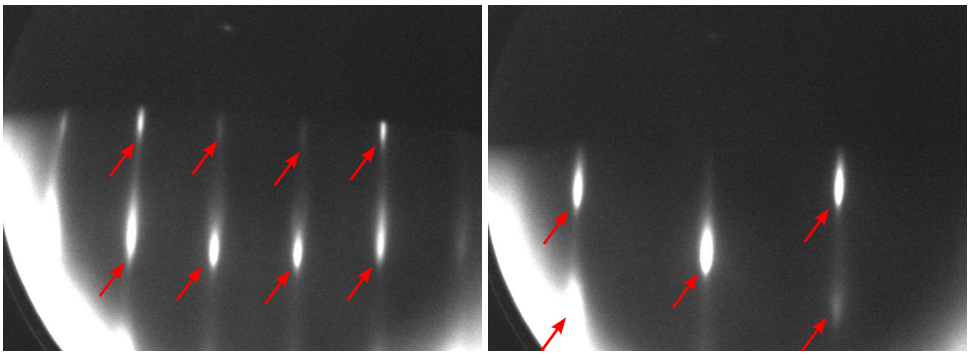

(a) Initial angle (b) Relative angle of 45°

Figure 3.12: RHEED image of Fe(001) on MgO taken at $E_{kin} = 50$ keV. The displayed pattern suggest three-dimensional islands after [32], at first sight (red arrows) (see Fig. 3.11). To support this assumption, an image along the same direction as (a) is analyzed in figure 3.13. The image in (a) indicates a distorted 4-fold symmetry and the one in (b) a 6-fold symmetry meaning that we were looking along the [10]- and [11]-direction of the island superstructure.

periodic pattern) which has small islands all over the surface (which creates the 4-fold symmetry pattern). The overlaid 4-fold pattern can only be a result of small islands of the iron film unless there are other gaseous materials in the chamber which were adsorbed during evaporation. Since the principal residual gasses in the chamber are nitrogen, hydrogen and water, which do not adsorb crystalline at room temperature, adsorbed residual gases cannot induce the observed diffraction pattern. Further qualitative analysis of the islands is done in section 3.6.2.

RHEED oscillations

When measuring the intensity of a diffraction spot while evaporating a thin film onto the substrate, a periodic change can be observed, the so-called *RHEED oscillations*. The cause of this phenomenon is that each time a new monolayer gets assembled from single atoms, the symmetry of the surface is lowered compared to that of a complete monolayer. This means, that when the intensity has a local maximum, we have just evaporated a full monolayer and when the intensity has a local minimum, we are just right in the process of building the next monolayer. RHEED oscillations can be used to cross-check the rate measured with the quartz micro balance (sec. 3.2.3). They also depend on the temperature of the substrate during evaporation [33].

Since the measurement of RHEED oscillations was not essential for our experiments it was not subject to further investigations. However, we measured 3 curves for a diffraction spot while evaporating Fe on MgO during the first evaporation tests. The rate was about $0.05 - 0.1 \text{Å s}^{-1}$ as measured

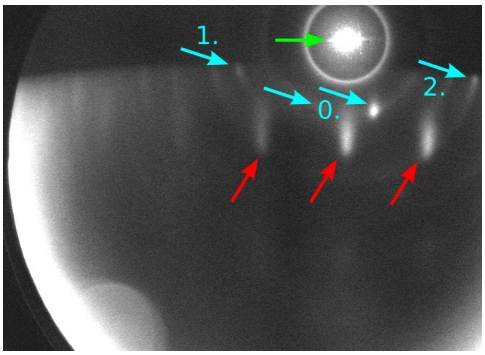

Figure 3.13: Another RHEED image of Fe(001) on MgO taken at $E_{kin} = 50$ keV at the initial angle position (see Fig. 3.12, (a)). In this image, the direct beam is clearly visible (green arrow) and can be distinguished from the other spots due to its central position and bright intensity. Blue arrows indicate the diffraction spots of zero, first and second order (see 3.11, (a)) of a flat and periodic structure with sharp spots. Red arrows indicate the superstructure again (Fig. 3.12).

with the QMB. The RHEED oscillations measured in the first and third run did not yield any periodic change in intensity due to fluctuations of the electron beam evaporator[13], however the second run showed an oscillation that might come from a layer-by-layer growth.

Figure 3.15 shows the evaluated RHEED oscillation from the second run. The mean value of the duration to finish one monolayer (i.e. 10 Å) is is determined to be 80 s which corresponds to a rate of 0.1 Å s^{-1} which is in agreement with the rate measured with the QMB.

3.6.2 STM Analysis

Basics of STM

STM stands for Scanning Tunneling Microscopy and is a technique for real-space analysis of samples at an atomic scale. Unlike methods which use reciprocal space, it yields an image which reflects almost exactly the true morphology of a surface[14]. The basic physics behind an STM is the *Quantum Tunneling Effect*, the phenomenon which describes the ability of particles on the atomic scale to tunnel through energy barriers which they could never overcome when applying classical physics. Since the morphology is analyzed by measuring the tunneling current between STM tip and sample

[13] Fluctuations are usually compensated by adjusting the filaments whose light is seen as background illumination on the RHEED screen.

[14] Since STM measures the electron densities instead of the atoms, the picture might still look a bit different from the real surface.

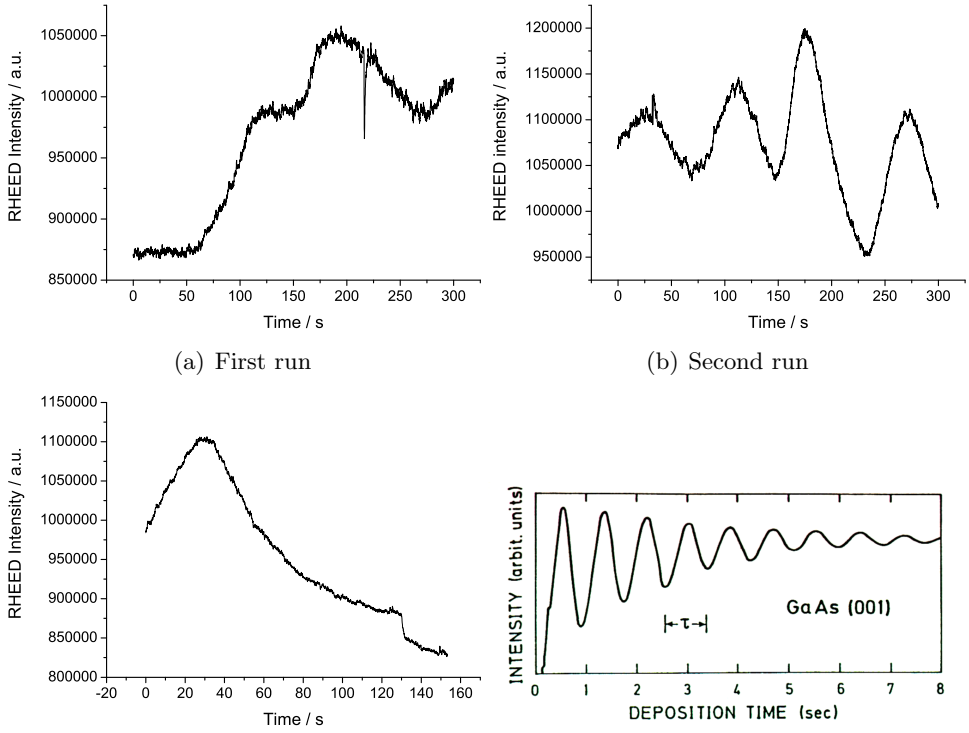

(a) First run (b) Second run

(c) Third run (d) Oscillations from [20]

Figure 3.14: Several runs of measured RHEED oscillations illustrating the layer-by-layer growth of Fe on MgO(001). During the first and the third run (plots (a) and (c)), we had problems maintaining a stable rate from the electron beam evaporator. The variations in amplitude do not result from the growth but from the changing background luminescence of the evaporators filament. During the second run (b), the evaporation rate was stable most of the time and so we think the oscillations observed really result from the growth while there is still a background from the filament which changes the amplitude. Figure (d) shows a measurement from literature [20] which exhibits perfect periodic behavior with exponentially decaying amplitude meaning the film grows thicker and out of focus from the electron beam.

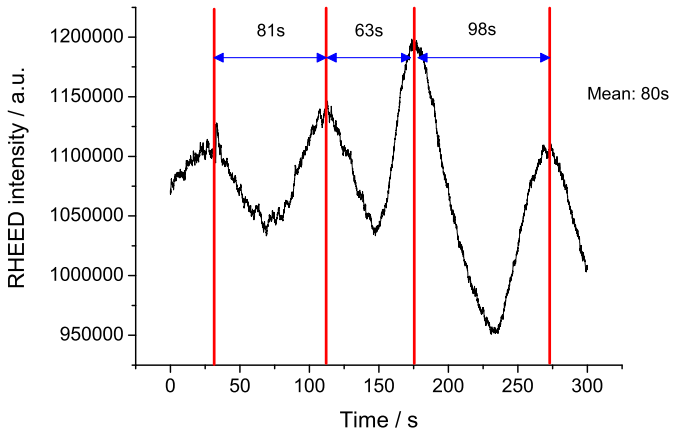

Figure 3.15: Each intensity peak has been marked on the time axis allowing to determine the distance between two peaks which reflects the amount of time that was necessary to grow one monolayer, we took the mean value of these intervals. The increase in amplitude in the last peak was due to a mandatory increase of the EBE filament current (the rate was decreasing) which generates an offset (filaments glow brighter).

while scanning over the sample, its surface has to be electrically conducting. In order to be able examine non-conducting surfaces, one either has to cover the surface with a conducting layer (in most cases a thin evaporated gold film will suffice) or use the related *Atomic Force Microscopy* instead. As our substrates are originally insulators (MgO), STM cannot be performed before the metallic films are evaporated onto the surface. Electrical contact with the STM electronics is made with the Omicron sample plate, the clamps of the holder must therefore have electrical contact with the films. To improve the contact further, we welded a contact needle to the sample holder which would poke into the substrate (see Fig. 3.4).

For a generic wave function which represents a particle, for the transmission probability it can be shown [34] that:

$$T = |S(E)|^2 \;=\; \frac{16E(V_0 - E)}{V_0^2}\; \exp\left(-4\sqrt{2m(V_0 - E)}\;\frac{d}{\hbar}\right) \qquad (3.10)$$

where S is the ratio of the amplitudes of the incoming and transmitted wave functions, E the kinetic energy of the particle and V_0 the energy of the potential barrier. The equation is valid in the approximation of wide and high barriers. Thus the probability of a particle to tunnel through a barrier decays exponentially with the width d of the barrier. Using *Fermi's Golden Rule*, we can derive an expression for the tunneling current:

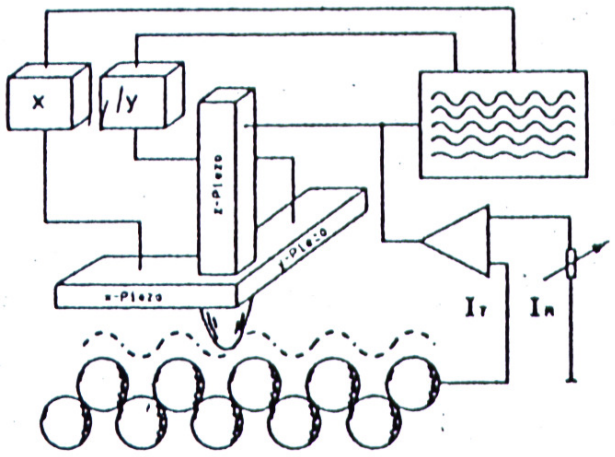

Figure 3.16: Generic scheme of an STM. A very fine tip (usually tungsten or platinum) is scanned along the topography of the surface. As the distance between tip and sample changes while the tip is held at *constant height*, the tunneling current will change. In *constant current mode*, the tunneling current is kept constant over a feedback circuit which adjusts the height of the tip over the sample by controlling the piezo manipulators.

$$I_{\text{tunnel}} \propto \exp(-2\kappa d) \tag{3.11}$$

with $\kappa = \frac{\sqrt{2m_e\Phi}}{\hbar}$, ϕ being the work function of the conducting material. From Equation 3.11 it is clear, that I_{tunnel} depends exponentially on the distance d between tip and surface: if that distance changes by just one Ångstrøm, the current will change by one magnitude already. Thus even smallest corrugations around 0.01 Å can be detected at best. Figure 3.16 shows the generic scheme of an STM.

We used a combined STM/AFM setup by *Omicron Vakuumphysik GmbH* [35]. It's located within the analysis chamber of the MBE chamber (see Fig. 3.1) and can be operated both as an STM as well as an AFM. The images were stored with the software provided by Omicron (*Scala Pro 4.1*), for analysis of the images we used the freeware *wsxm* [36]. It allows plane correction (for taking into account when the sample is not located perpendicular to the STM tip), Fourier analysis, smoothing, roughness analysis, distance calculations and a lot of methods to spruce up the images for better presentation.

Before we started with the real surface analysis with the STM, we ran a few tests to get familiar with the operation and usage of the STM. It turned out that both positioning the samples with the wobblestick into the

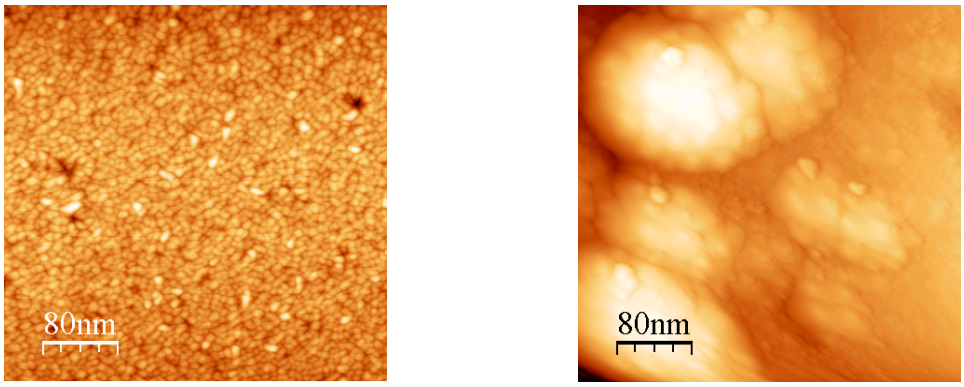

(a) First STM image of Fe (b) First STM image of Au

Figure 3.17: First STM images taken of iron and gold surfaces evaporated with the electron beam evaporator. While iron (a) has a rather smooth surface with a small grain size, the gold surface is marked by several large blobs (b). For detailed analysis, see Sec. 3.6.2, 3.6.3, 3.6.4.

STM as well as the operation of the STM require quite some practice and experience. For example, every tip will always produce a different quality of images. So does an old tip yield different results. In principle, best results are achieved with a single-atomic tip. In order to get a single atom at the tip, one needs to carefully crush the tip into surface in a controlled manner by increasing the *Loop Gain* (a relative value which controls how strong the feedback control for height correction is set in constant height mode) and the *Bias Voltage* (the applied voltage between tip and sample) both by a factor of 10 to pick up an atom from the sample surface. After a minute, both settings can be restored to normal and the tip is moved to a fresh spot. Usually this will yield usuable results if there were problems acquiring a proper image before. Before acquiring an image, both the forward and backward scan display windows of the software should be set to *line scan*, allow to control that both scans of the same line deliver the same profile. If these profiles don't match, either the tip has still a blunt shape or the current spot on the sample is inappropriate for measurements.

For both iron and gold, Table 3.4 shows the parameters for the Omicron STM which were used as initial values when tuning the STM for image acquisition.

Corrugation Analysis

In the quest to find the optimal parameters for sample preparation we wanted to investigate how the temperature of the substrate influences the roughness of the surface when evaporating. In [37] Rieder et al. showed

Parameter	Initial Value
Bias Voltage / V	0.3-0.7
Feedback Current / nA	0.1
Loop Gain / %	0.5-1
Scan Area / nm^2	400×400
Scan Speed / $nm \times s^{-1}$	100

Table 3.4: Initial parameters for STM image acquisition.

that the temperature of the substrate has to be high enough to overcome the *Schwoebl barrier*. An energy which defines the lower limit at which large, atomically flat surfaces can be achieved. The additional energy is required for the atoms to have the necessary mobility to distribute evenly along the surface. Below this energy, the film is expected to grow islands instead of flat terraces. On the other hand, high temperatures mean that the atoms have an increased mobility so the chances that disordering of the surfaces takes place is higher. Apparently both effects are competing and thus we want to check the situation for the case of iron on MgO(001).

The flatness of the surface was important for our iron-gold interface. Large corrugations at the interface can increase scattering and lower the efficiency of hot electron injection from the ferromagnetic layer into the gold layer. To investigate the temperature dependence, we evaporated iron from the electron beam evaporator (see Sec. 3.2.1) at different substrate temperatures, namely 100°C, 200°C, 300°C, 400°C, 500°C and 600°C. Several STM images of these samples were taken directly after evaporation and the data was again analyzed with *wsxm* [36]. However, due to problems with the electrical contact, we couldn't take any STM images of the sample evaporated at 500°C substrate temperature.

The software *wsxm* allows for roughness analysis by plotting histograms of the surface corrugation. This yields a column bar plot which plots the number of events over the height of each pixel in the image. Importing these histograms into *Microcal Origin* and fitting them with a Gaussian yields a value for the roughness from full width at half maximum of (FWHM) the peaks. Four images of each temperature were taken and analyzed. We took the mean value of the four FWHM values calculated and finally plotted these over the temperature. The result is shown in figure 3.18.

To conclude, the corrugation is nearly constant over the temperature range we investigated. The corrugation shows a slight increase with growing temperature, however, this might be owed to other external fluctuations during evaporation or STM measurements. We will see in the next chapter though that the temperature still influences the film quality as higher temperatures increase the grain sizes. As a conclusion, we evaporated the films

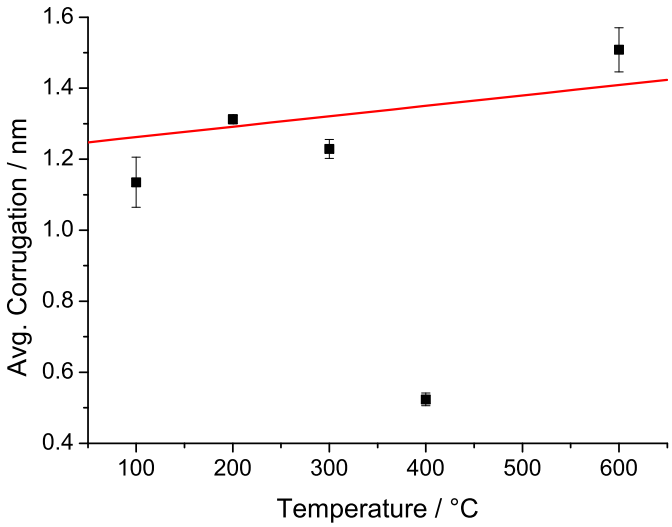

Figure 3.18: Temperature dependence of corrugation during evaporation. Data was taken from the FWHMs of the histograms in figures 3.19-3.23. The data point at 400°C was omitted in the linear fit since the STM measured unrealistic corrugations (see text), the rest was fitted with a linear function.

at room temperature to achieve a well-defined interface between iron and gold.

3.6.3 Grain size analysis

In addition to an increase of the corrugation with higher substrate temperatures during evaporation, it has become obvious that the average size of the grains of the iron film has a temperature dependency as well. Looking at the STM images of the corrugation analyses (Fig. 3.19-3.23), it can be immediately observed that grain sizes increase with higher temperatures. To analyze grain sizes, we needed to find a solution which would yield reproducable and comparable results. Simply performing a profile analysis with *wsxm* would not be able to yield exact values for corrugations as the grain sizes of a single film vary statiscally over the whole film area. Analyzing lattice constants with *wsxm* works best when the lattice has high symmetry which is not the case for the iron films. A good method therefore was to calculate the auto correlation (AC) of the image data and plot it against the grain size. The result from this analysis is a plot which yields a kind of histogram of the distances on the film and the shape of it allows to infer the long distance order and the typical grain size of the film.

We have written a small program in *C* (*autocorr.c*) which performs the auto correlation, its source code can be found in the appendix (see B). It

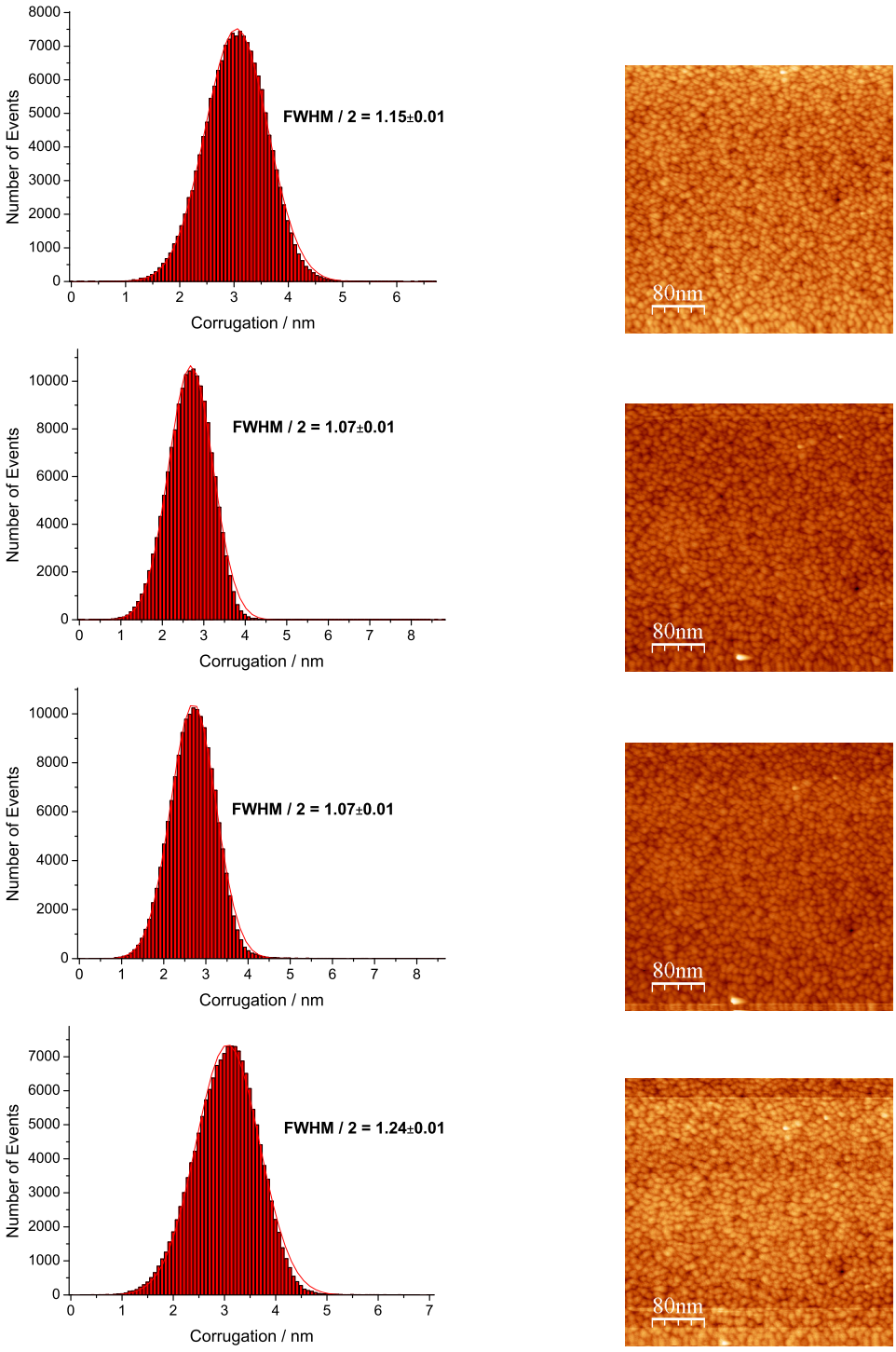

Figure 3.19: Corrugation histograms of Fe evaporated at 100 °C

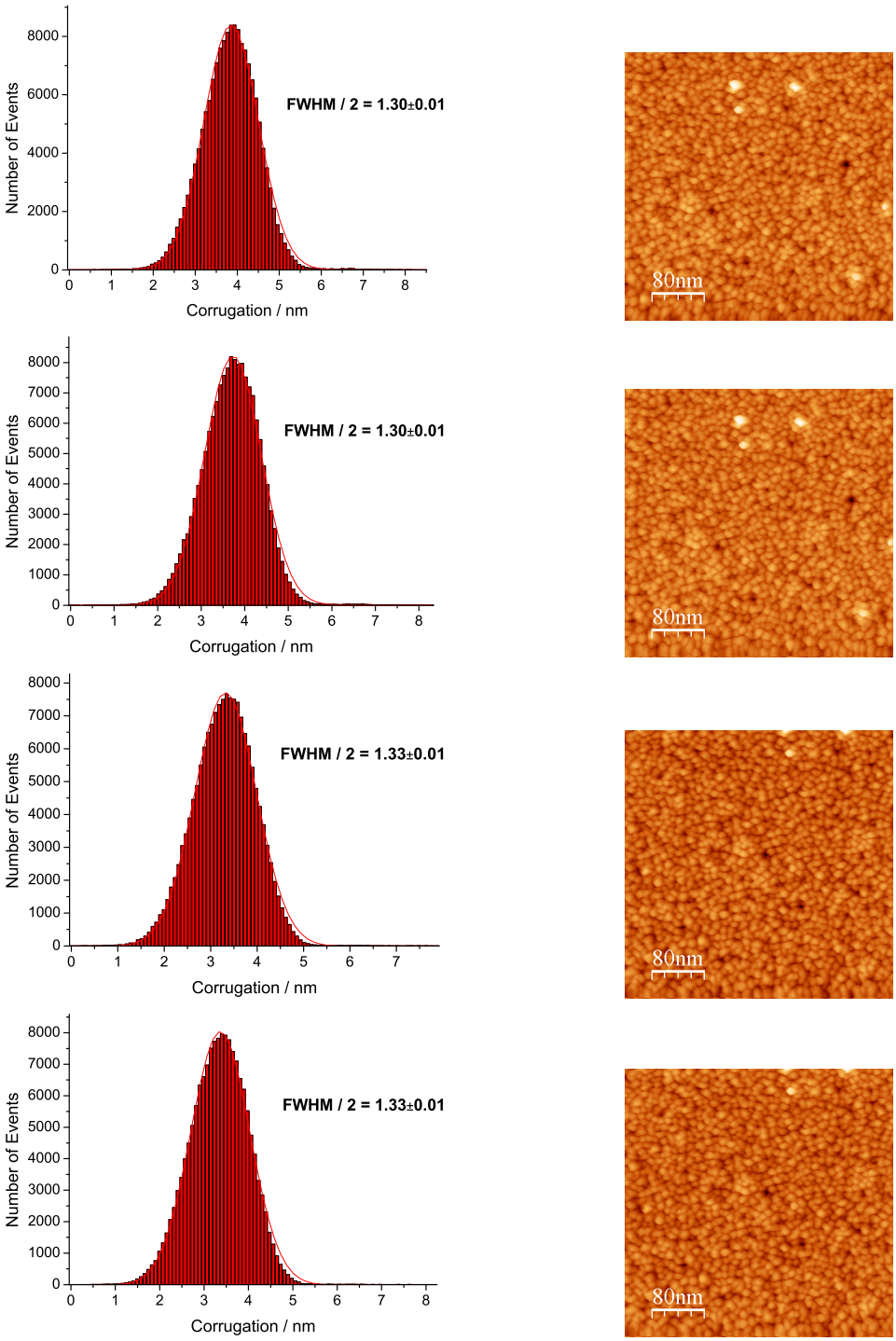

Figure 3.20: Corrugation histograms of Fe evaporated at 200 °C

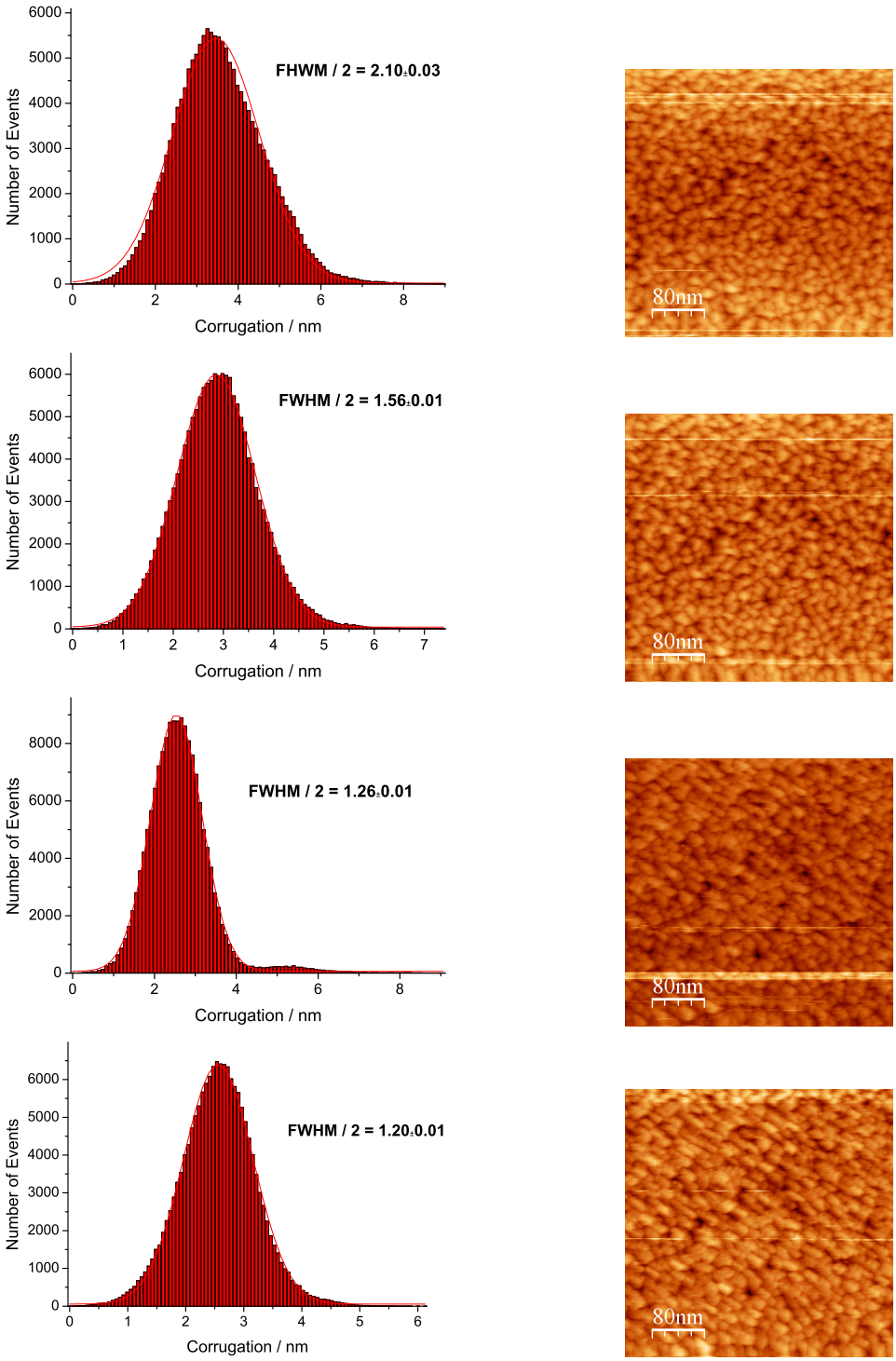

Figure 3.21: Corrugation histograms of Fe evaporated at 300 °C

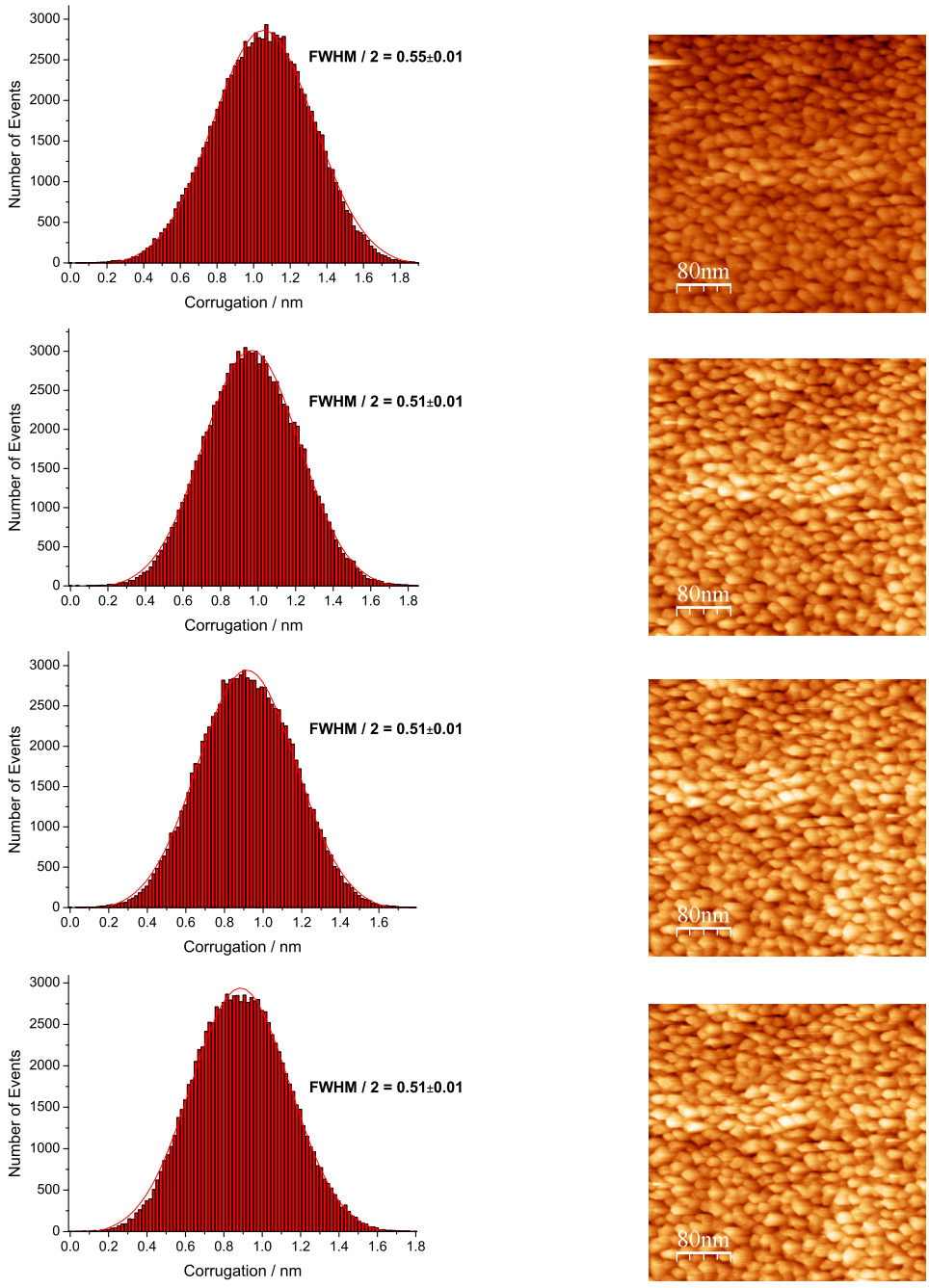

Figure 3.22: Corrugation histograms of Fe evaporated at 400 °C

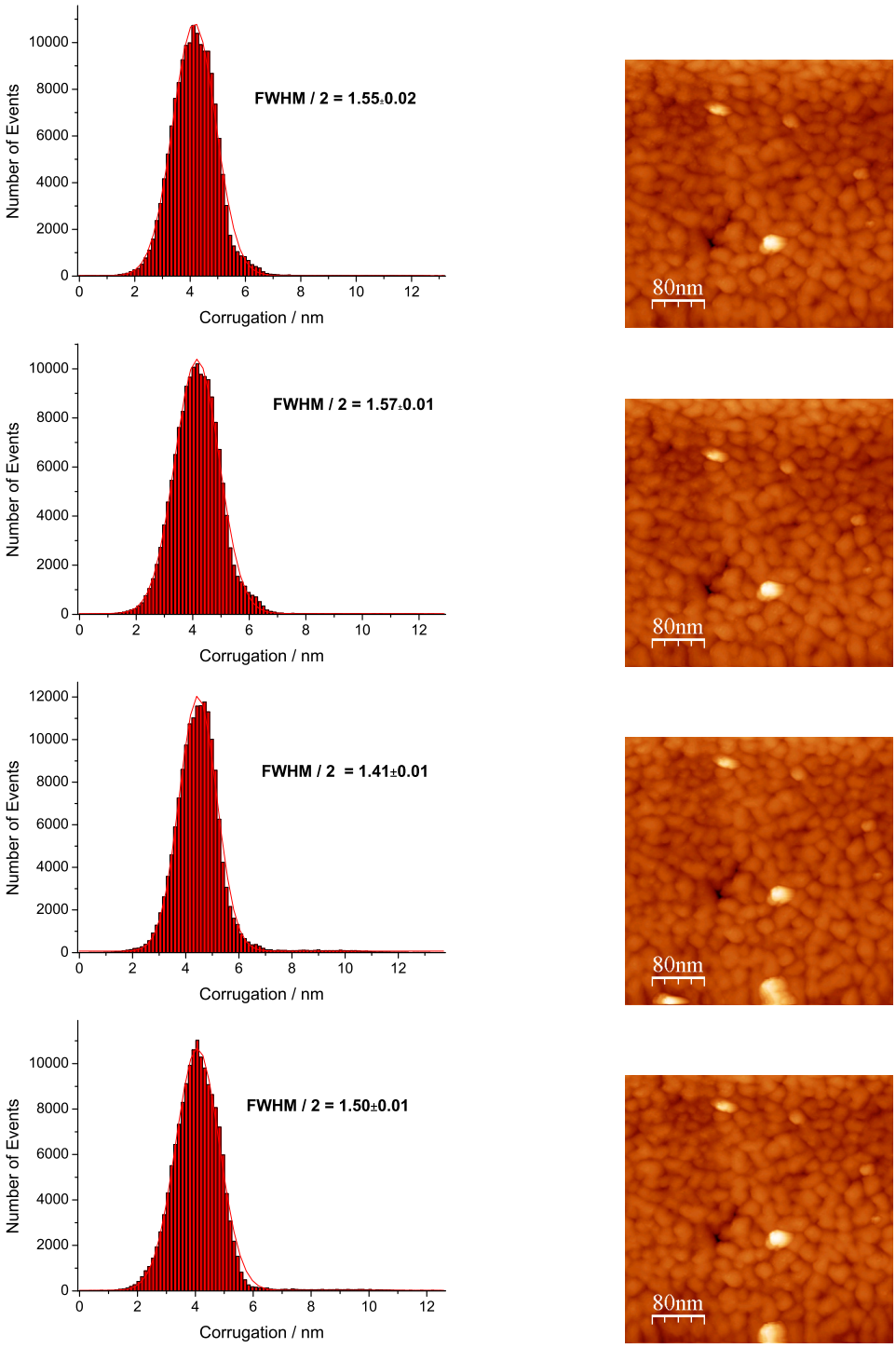

Figure 3.23: Corrugation histograms of Fe evaporated at 600 °C

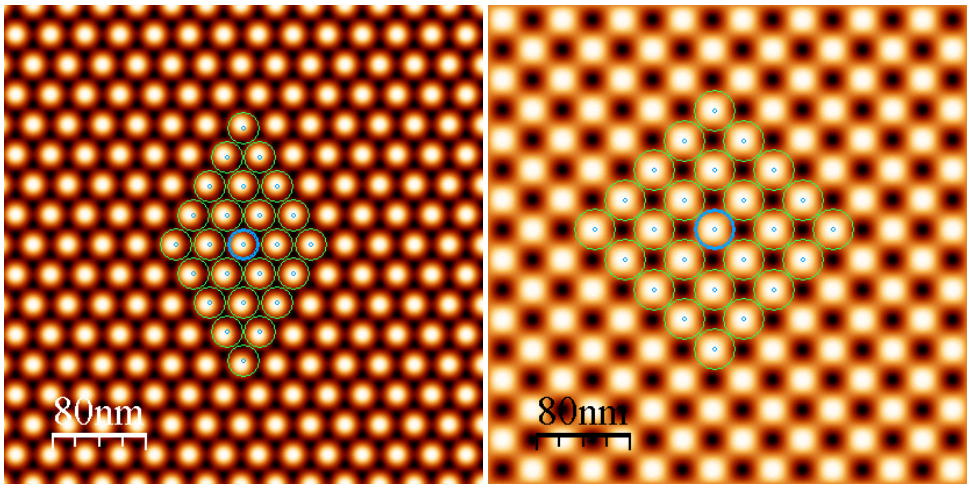

(a) Model for *hcp*-lattice (b) Model for *sc*-lattice

Figure 3.24: STM images of model lattices generated with *Origin*. Both images were overlaid with a grid for lattice constant analysis. Since the surface symmetries of the surfaces are very high, the lattice constants could be determined very easily with this method.

parses STM image data exported from *wsxm* as ASCII matrix input files, calculates the auto correlation and outputs the result to the terminal. The result would be redirected into a file which then could be read into *Origin* to analyze the peaks.

The input data (the STM images) is the same that was used for the corrugation analysis in the previous section. We calculated and plotted the auto correlation for each of the four images of each temperature and combined the four images at one temperature into one plot. Then we plotted the mean value of the auto correlation from the four images, disregarding outliers if any. The resulting plots are shown in Fig. 3.26.

To test our algorithm, we generated two model lattices (*simple cube* (sc) and *hexagonal closed-packed* (hcp)) and analyzed the grain sizes there with the auto correlation algorithm. Since we know the lattice constants for our model lattices, we can cross-check the plots to find the corresponding peaks.

The model images could be easily analyzed with *wsxm* since their lattices have a high symmetry. To determine the lattice constant, the software provides the possibility to overlay the image with a grid whose lattice constant and type (e.g. *hexagonal*, *sqaure*, *7x7* and so on) has to be adjusted to match the underlying image. One can then immediately read the lattice constant and type from the software. Figure 3.24 shows the results.

The lattice constants for the model images were determined as follows:

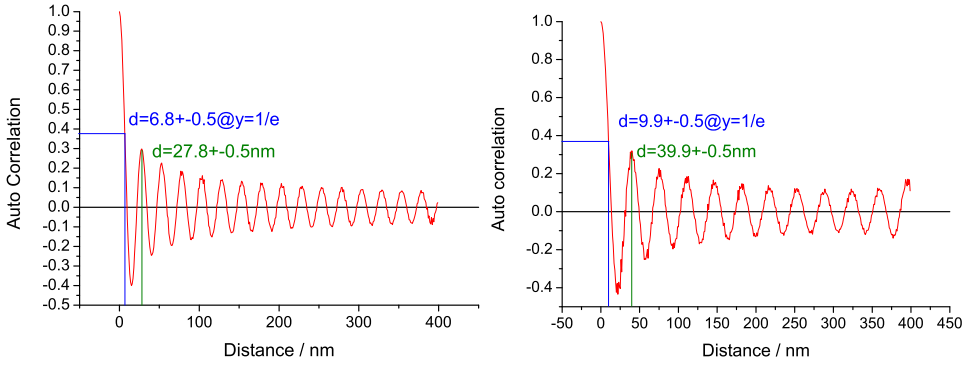

(a) AC plot for *hcp*-lattice (b) AC plot for *sc*-lattice

Figure 3.25: Auto correlation plots for the STM model images generated with *Origin*. The grain sizes can be read from the dominating distances found between atoms in the lattice. Every peak represents such a distance. The first peak reflects the distance of one atom to its next neighbours. It can also be read at $y = \frac{1}{e}$.

$$d_{hcp} = 28 \text{ nm} \tag{3.12}$$
$$d_{sc} = 35 \text{ nm} \tag{3.13}$$

where d is the shortest distance to the next lattice point.

Now, if we take a look at the auto correlation plots for the two model lattices in Figure 3.25, we can read the lattice constants from the first peaks of the oscillations:

$$d_{hcp} = 27.8 \pm 0.5 \text{ nm} \tag{3.14}$$
$$d_{sc} = 39.9 \pm 0.5 \text{ nm} \tag{3.15}$$

The lattice constant for the hcp-lattice read from the auto correlation analysis matches with the value determined with lattice analysis with *wsxm* within error range. For the sc-lattice, however, the lattice constant read from the auto correlation analysis differs by a magnitude of the error range. The reason is that the auto correlation analysis accumulates the distances to all next neighbours in the lattice. For hcp, the distance to all the next neighbouring lattice points are equidistant. For sc, however, one point has four neighbours with distance d and four with distance $d \times \sqrt{2}$. Thus, we have to calculate the average distance for all eight neighbours, which is:

$$d_{sc}^{avg} = \frac{d_{sc} + d_{sc} \times \sqrt{2}}{2} = \frac{(35 + 35 \times \sqrt{2}) \text{ nm}}{2} \approx 42.2 \text{ nm} \tag{3.16}$$

Thus the values lie within fivefold error intervals which is still acceptable. Moreover, the value for the lattice constant can also be read at ordinate value $\frac{1}{e} \approx 0.37$, more precisely the axis of abscissae at $y = \frac{1}{e}$ corresponds to $\frac{1}{4}$ of the lattice distance. This becomes helpful when the auto correlation has very small oscillations to determine the lattice constant from the peak occurences.

Taking a look at the AC plots from the real STM image data in Figure 3.26, it's apparent that the oscillations in the AC are too small to be accounted for. Thus, we looked at the values for the distances at $y = \frac{1}{e}$ and plotted those over the temperature. The result is shown in Figure 3.26 (f). Likewise the corrugation, the grain size clearly has a proportional dependence on the substrate temperature during evaporation in the sense, that basically the grain size grows with the temperature, ranging from 16 to 56 nm (4 to 14 nm $\times$ 4).

Thus this grain size analysis also suggests growing the films at lowest possible substrate temperatures to achieve smooth and flat films.

3.6.4 Grain size comparison: Fe and Au

From the STM image analysis in the last chapter we know that the average grain size for our iron films varies from 16 to46 nm, depending on the temperature of the substrate during evaporation. Now, let us compare the grain sizes of our iron and gold films as they were prepared with MBE. For this, we let the auto correlation algorithm analyze the STM image of gold ($d \approx 50$ nm) from Figure 3.17. The resulting AC plot is shown in Figure 3.27, the typical grain size is around 200 nm.

To conclude the grain sizes (evaporation at room temperature):

$$d_{Fe} \approx 16 \text{ nm} \tag{3.17}$$

$$d_{Au} \approx 200 \text{ nm} \tag{3.18}$$

Since the images are only 400 $\times$ 400 nm in dimension and the blobs on the gold surface cover half of the image (they are 200 nm), heights are not Gaussian distributed as they are for iron so we can not apply the method from Section 3.6.2 to determine the corrugation of the surface.

3.6.5 Analysis Conclusion

To conclude the quality analysis for Fe on MgO(001) from RHEED and STM:

- Fe grows as expected with low corrugation ($\approx$ 1 nm) on MgO(001)

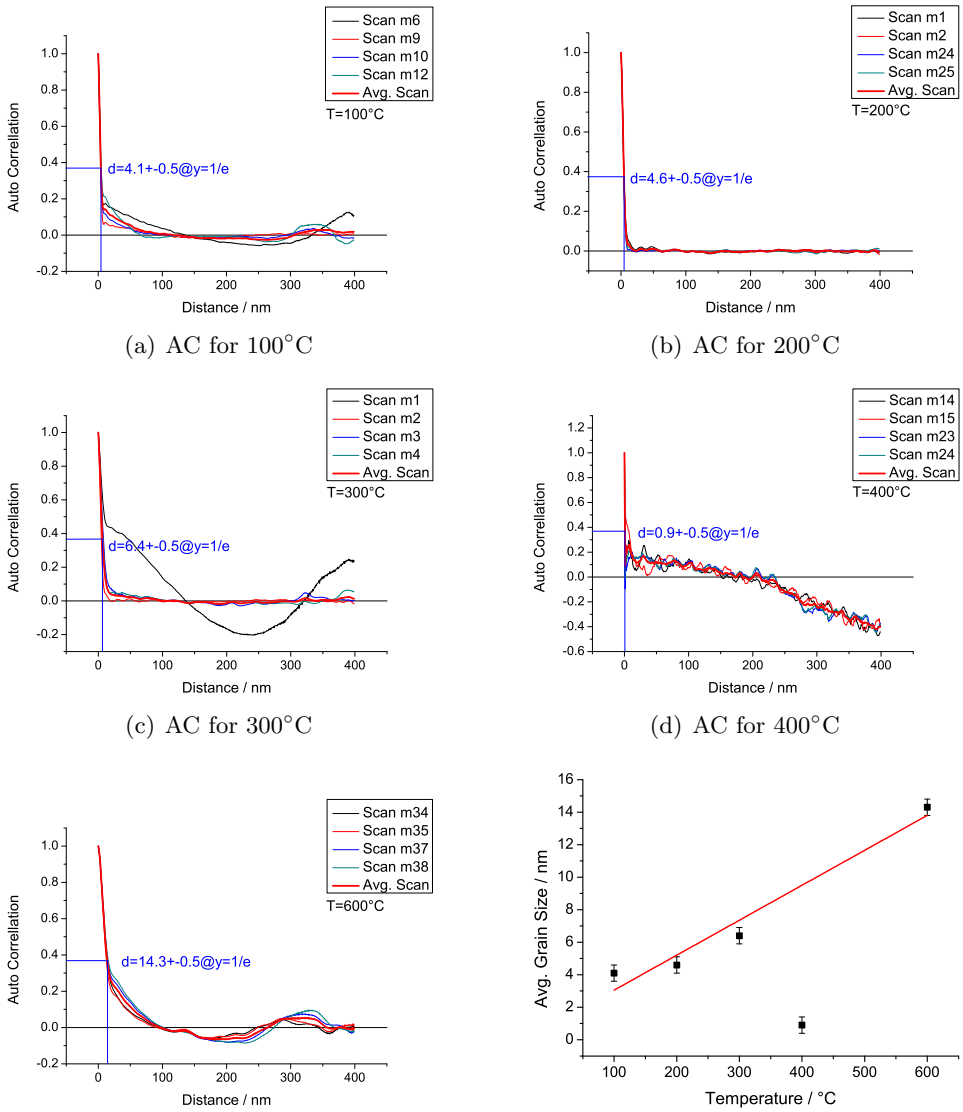

(a) AC for 100°C

(b) AC for 200°C

(c) AC for 300°C

(d) AC for 400°C

(e) AC for 600°C

(f) Grain size against temperature

Figure 3.26: Auto correlation plots for different temperatures

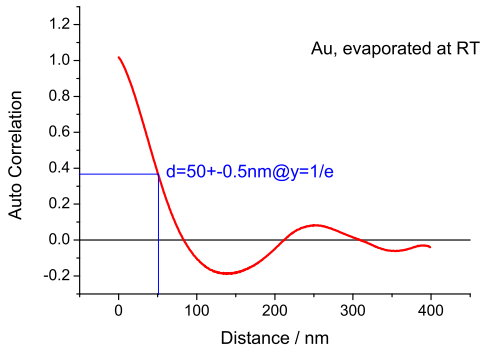

Figure 3.27: Plot of the auto correlation for the STM image of gold. The grain size (more accurately $\frac{1}{4}$ of it) was read again at ordinate value $y = \frac{1}{e}$, around 200 nm. As opposed to the AC analysis for iron, a smooth oscillation was observed.

- layer-by-layer growth can be observed
- corrugation results from small islands, these can be seen as grains in the STM
- corrugation and grain size depend on the substrate temperature during evaporation
- the lower the substrate temperature, the lower the corrugation
- the lower the substrate temperature, the smaller the grain size
- Fe has a small grain size (about 20 nm) while Au forms blobs of up to 200 nm lateral dimension

3.7 Final sample parameters

The samples which were used for the measurements were evaporated with parameters determined from the previous analysis (samples 1-3 were measured in the SHG setup while we were still investigating with the sample preparation). That is, the substrates were not to be heated during evaporation and the samples were cleaned, outgassed and annealed prior evaporation. We produced wedges for the thickness dependency analysis. Sample 9 was made to check whether the evaporation rate has any influence on the roughness of the surface. The samples have associated numbers which are referred to in the chapter on measurements and results. This allows to crosscheck the evaporation parameters once two samples show different results in the SHG

experiments[15]. Table 3.5 lists all samples and their parameters with date and sample number, figure 3.28 illustrates the samples.

[15]This was actually the reason why sample 9 was made. We had different results on samples with identical film thicknesses but which were evaporated at slightly different rates. Since the rate can play a role in the surface roughness we investigated whether this was actually the reason for the different results.

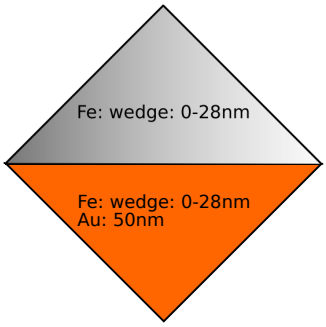

(a) Sample 1

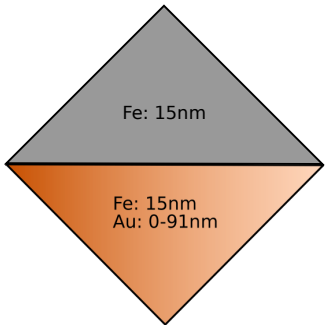

(b) Sample 2

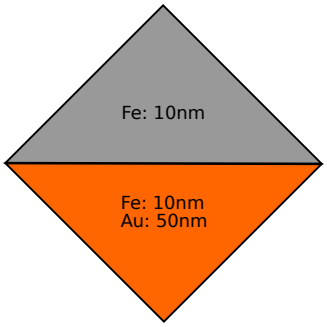

(c) Sample 3

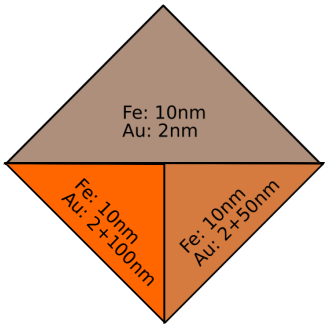

(d) Samples 4, 5 and 6

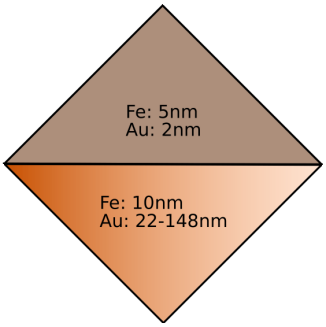

(e) Sample 7

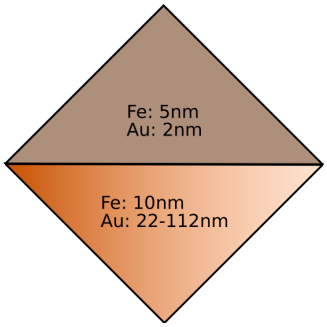

(f) Sample 8

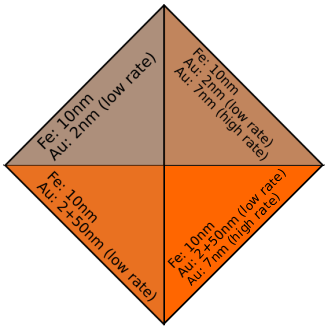

(g) Sample 9

Figure 3.28: Illustrations of the samples used for SHG measurements. All samples consist of $10 \times 10 \times 0.5$ mm^3 MgO(001) substrates on which Fe films of various thicknesses are evaporated over the whole substrate area. The Au films cover the Fe films with different geometries and thicknesses over the substrate area. See table 3.5 for detailed sample parameters.

No.	**Type**	**Date**	$\mathbf{d}_{Fe}$ nm	$\mathbf{Rate}_{Fe}$ Ås^{-1}	$\mathbf{d}_{Au}$ nm	$\mathbf{Rate}_{Au}$ Ås^{-1}	T_{evap} °C	T_{anneal}/t °C	T_{degas}/t °C
1	Fe wedge	10.4.2009	0-28	0.4	50	0.1	400	800	100-110
2	Au wedge	20.5.2009	15	0.05	0-91	0.1	400	1000	100-110
3	Au 50	22.5.2009	10	0.05	50	0.1	400	800	100-110
4	Au 50/100	1.7.2009	10	0.1	48 / 98	0.5/2.0	RT	600	100-110
5	Au 50/100	7.7.2009	10	0.1	48 / 98	0.1	RT	600	100-110
6	Au 50/100	9.7.2009	10	0.05	49 / 96	0.2	RT	600	100-110
7	Au wedge	31.7.2009	5	0.05	22-148	0.3-0.4	RT	600	100-110
8	Au wedge	5.8.2009	5	0.05	22-112	0.4	RT	600	100-110
9	Au flat/rough	2.9.2009	10	0.05	50 / 57	0.2/2.4	RT	600	100-110

Table 3.5: Parameters of the samples prepared for SHG measurements.

Chapter 4

Measurements and Results

In the previous chapters we have outlined our motivation for this project as well as the prerequisites which include the improvements to the experimental setup as well the sample preparation. We now turn our focus to the laser experiments performed. We have run various measurements with the samples to investigate electron and spin dynamics over different time scales as well as different thicknesses for the non-magnetic spacer layer (gold). Furthermore we used both non-linear (SHG) and linear optical effects to be able to compare both techniques in regard to their suitability for the investigation of electron and spin dynamics. The measurements performed can be summarized as follows:

- Hysteresis analysis: ferromagnetic properties of the iron layer
- Shorttime SHG: ballistic vs. diffusive transport
- Longtime SHG: electronic vs. phononic transport
- Wedge measurements: thickness dependency of transports
- MOKE measurements: alternative method to analyze spin dynamics

We have dedicated one section for each of the measurements. Prior to any series of measurements, especially after a new sample has been inserted, the optical setup has to be realigned. Since this involves a number of steps, we describe this procedure in detail in the following section.

4.1 Alignment procedure

The laser cavity (see Sec. 2.4.1, Page 20) is first adjusted for maximal output. For this, the end mirrors (**OC** and **HR**)) are adjusted for maximal output in *cw* mode. The laser is put into mode-locking and optimized for maximum output with the cavity dumper enabled by adjusting the end

mirrors, pick-out mirror, Ti:Sa crystal, prisms (**PR1** and **PR2**) (see Fig. 2.8, Page 22. The cavity is adjusted such that in the spectrum of mode-locking regime the cw-component will be suppressed, The control unit of the cavity dumper allows to set the delay, phase, dumping rate and output power of the RF signal (see Sec. 2.4.1, Page 20, Subsection "Cavity Dumping"). Once the laser has been aligned for maximal and stable output, we performed the adjustment of the beam overlap.

4.1.1 Beam overlap

The two beams (pump and probe) have to be in time and spatial overlap. This means, that both beams will join on the sample with identical delay and position. The overlap is conveyed by coherence effects which can be detected with the linear detector (see Sec. 2.3.1, Page 11). To find the overlap, the following steps have to be performed. First we try to find a rough spatial overlap of the two beams on the sample with the help of an optical microscope. Since 50 or even 100 nm thick gold films won't let the pump beam pass through in back pump configuration, we are using the thin gold regions to perform this alignment. Then both the pump and the probe can be seen as bright spots on the sample. *The higher the roughness of the films, the higher the scattering and the better the visibility of the laser spots on the sample.* Once the spatial overlap is found, we measure the *cross correlation* signal by scanning through the time delay (Fig. 4.1). We usually block the pump beam with the knife for this (see Figure 2.5, Page 18). The zero delay is found by determining the center of the Gaussian. Once the zero delay has been found, fine spatial adjustment is performed by maximizing the intensity in the cross correlation signal. Further improvement in the signal is achieved by proper adjustment of the monochromator (alignment of beams into slit, fine tuning of wave length). This means that the foci and the beam position are adjusted with the lenses which focus the beam onto the sample (see Fig. 2.7, (f), Page 21). The previous time scan may be repeated to verify the zero is still valid. It has shown that the cross correlation signal heavily depends on the morphology of the sample. Samples which showed high scattering (bright spots visible in the microscope) usually yielded very irregularly shaped Gaussians which made it hard to find the zero delay. Once the proper overlap has been found, the knife is closed further to suppress also the cross correlation signal to make sure we measure the probe SHG only. In case of high scattering due to a rough sample surface, the blocking of the separate beams becomes more difficult and we have to find a compromise between blocking the cross correlation and letting the probe pass. If the scattering of the sample is too high it cannot be used for measurements however.

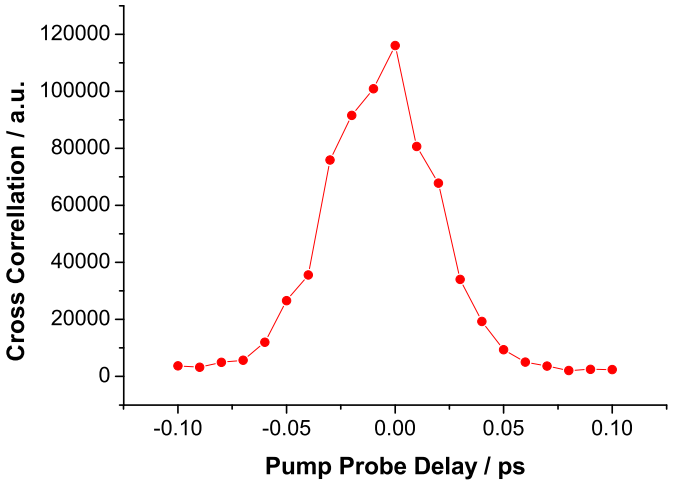

Figure 4.1: The cross correlation is the intensity signal obtained from the photo multiplier while scanning the time delay between pump and probe. At the exact time of overlap, the cross correlation signal will be maximum which sets the zero delay between pump and probe.

4.1.2 Laser-induced damage of the films

During the pump-probe experiments we experienced several problems with laser-induced damage. This means that the intensity of the incident pump laser beam was so high that it caused irreversible damage to the films. This damage could either be due to *heat accumulation* or it could be a *single shot effect* (high intensity). To verify this, we ran two small tests with **sample #6**. First we **reduced the repetition rate** by adjusting the cavity dumper to find a damage threshold. Within the range of adjustments, however, we couldn't determine a sane threshold rate. In the second test, we put an attenuator consisting of a polarizer and a $\lambda/2$-plate to rotate the polarization plane. We first set the angle to **30**° which corresponds to a beam power of approximately **18** mW (see Tab. 4.1) and positioned the laser beam onto a new spot on the sample and observed the burning in the microscope for several minutes. If there was any damage, the spot from the pump beam would gain intensity indicating that it digs itself into the sample. For **30**° and **20**° we did not see any "burning", even after more than 5 minutes of irradiation. We then changed the angle gradually from **20**° towards **0**°. Since burning was visible at an angle of **14**°, we ran a second test starting at this angle. We repeated this way until we found that at **17**°, which corresponds to approximately **37** mW, the sample would not be subject to any visible burning. *The laser-induced damage is therefore a single shot effect and can be avoided by reducing the beam intensity. This*

Rel. Angle °	**Power** mW
-5	37
0	42
10	42
15	40
20	34
25	26
30	18
35	11
40	5

Table 4.1: Calibration table: Power vs. angle of polarization filter

can also be achieved by defocusing the pump beam on the sample with the collimator lens. Subsequently we defocused the pump to reduce the intensity to below 90% in the following experiments.

4.1.3 Alignment of the photodiodes for MOKE and LR

Once the setup has been properly aligned for SHG, the alignment for the MOKE and linear reflectivity detectors is rather simple. The diodes just have to be aligned for maximum signal. And in case of the MOKE detector, the output signal of both diodes has to be balanced.

Alignment for MOKE

To measure the rotation of the polarization plane from the MOKE effect, we use a setup of two photodiodes which are equipped with a polarization filter each (see Fig. 4.2). The diodes are connected to a pre-amplifier which feeds the lock-in. The filters are positioned to have perpendicular orientation regarding their polarization plane. By measuring in perpendicular configuration, we are able to determine the rotation angle by adding the two components of the two vectors. For a proper alignment, the output of both diodes has to be balanced so that for a non-attenuated fundamental with no external magnetic field applied to the sample, the signal on both diodes is identical. In order to balance the diodes, the detector casing is attached to rotary holder which allows to set proper azimuth.

Alignment for LR

To measure linear reflectivity, we disconnected one of the two photo diodes in the detector. Then the spot is focussed and aligned onto the detector until the maximum output signal is observed. In case the output signal is

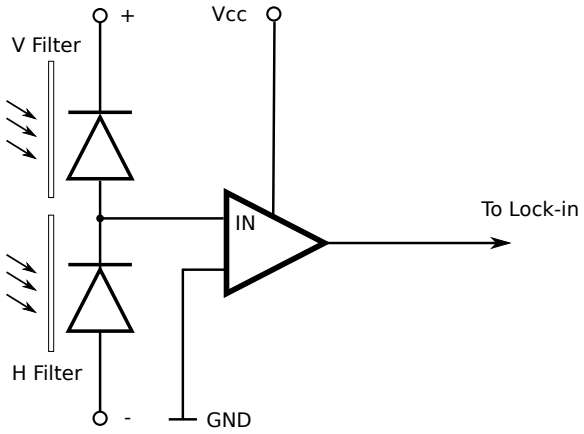

Figure 4.2: Our setup to measure MOKE uses two photodiodes wired in a voltage divider configuration. In case of identical signal intensities at both diodes, the voltage at the input of the pre-amplifier will be zero. With the help of the polarization filters, the diodes measure perpendicular components of the polarization which will be equal if the diodes are balanced and there is no MOKE effect. If we have a MOKE signal, the voltage at the pre-amplifier will be non-zero and an electric current is measured, amplified and fed into the lock-in.

too high, it will overdrive the pre-amplifier connected to the diodes. We therefore used filters to attenuate the intensity to a proper level so that we could use the full scale of detection of the diode.

4.2 Hysteresis analysis

To verify the ferromagnetic properties of the iron layer, we have performed optical hysteresis analysis. We wanted to make sure that the ferromagnetic properties would not be hampered by the adjacent gold layers. We therefore measured at spots on the sample where the gold layer had different thicknesses. Since the non-ferromagnetic gold layer suppresses the optical signal completely, measuring the hysteresis required the samples to be inserted into the sample holder with their back side (from which pumping normally is performed) facing to the front to be able to probe the ferromagnetic layer directly. Another motivation for the hysteresis measurements was to find out what external field is necessary to saturate the magnetization, that is find the critical external field at which the magnetization remains constant. The hysteresis was measured in *transversal geometry* of the external magnetic field. The current for the magnetic coils was swept from **-2.5** to **2.5** Amperes which corresponds to sweeping the external field from **-75** to **75** Gauss. We measured on **sample #6**. Figure 4.3 shows the results of the

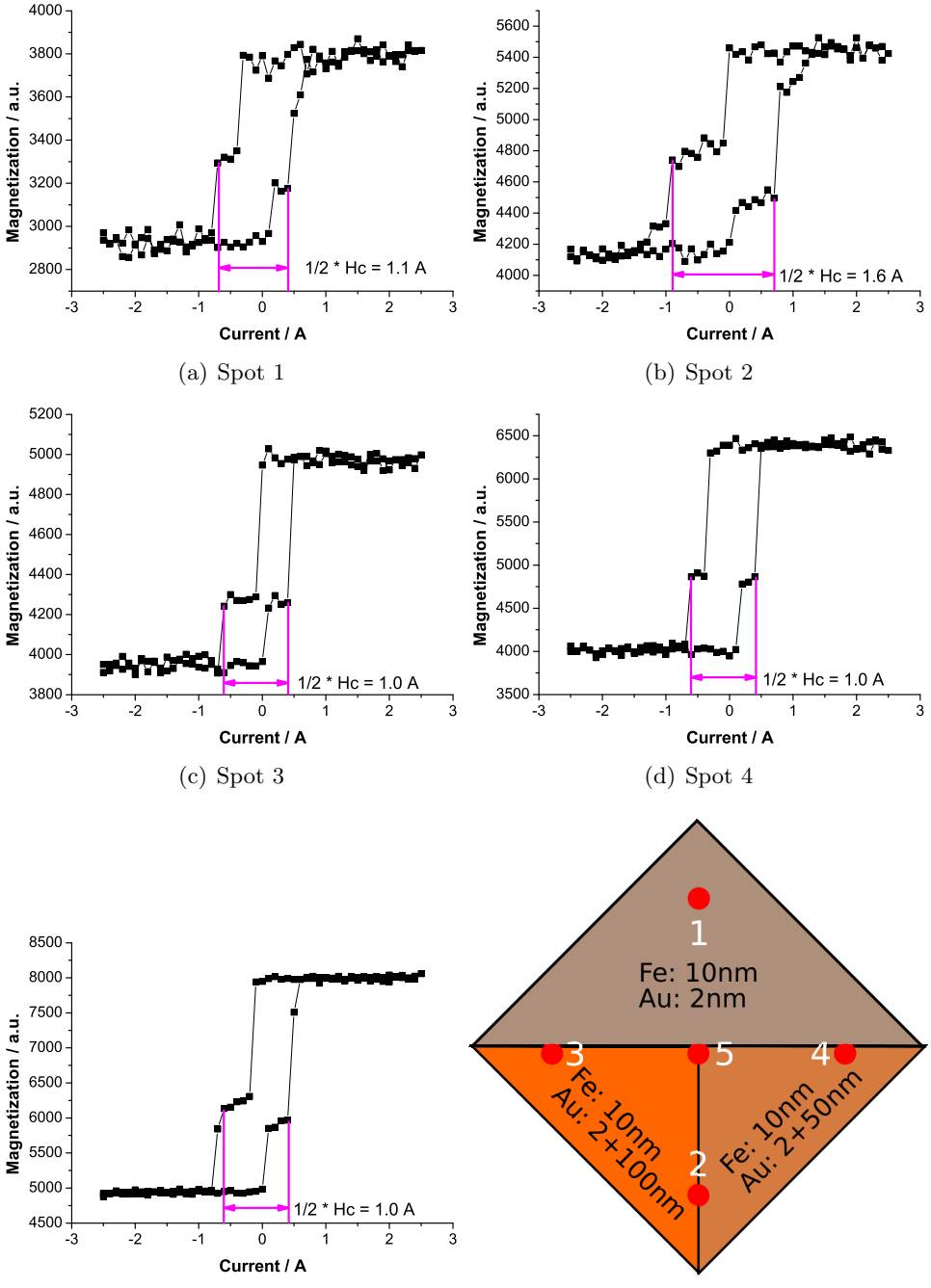

(a) Spot 1 (b) Spot 2

(c) Spot 3 (d) Spot 4

(e) Spot 5 (f) Spotmap

Figure 4.3: The Figures (a)-(e) show the hysteresis loops measured at different spots on the sample and therefore for different thicknesses of the gold layer. They have a more or less rectangular shape with some slight distortions. These distortions have also been found by Costa-Krämer et al. in [39]. What is important for us, is that the hysteresis curves have equivalent values for the coercivity ($H_c \approx 0.5$ A = 15 Gauss). We can conclude that the gold layer does not hamper the ferromagnetic properties of the iron layer. Saturation of magnetization is found at around 1 Ampere.

hysteresis analysis. We have probed at 5 different spots which lie below different thicknesses of the non-ferromagnetic gold layer. The hysteresis loops are comparable for all spots and show rectangular shapes as also reported by Costa-Krämer et al. in [39] for single iron layers. We therefore conclude that the ferromagnetic properties of the iron film are not influenced by the adjacent gold layer. A saturation of the magnetization occurs at around **1 Ampere**, that is around **30 Gauss**. Consequently we will sweep the current through the magnet between **-1.5 A** and **1.5 A** in the following experiments.

4.3 Shorttime: ballistic vs. diffusive transport

The first task of the series of optical measurements of the core experiment was to reproduce the previous results obtained within the scope of this project since we have made modifications to the setup (new magnet and sample holder, rearrangement of some components on the optical table). Furthermore, the new samples were produced with a different type of evaporator and chamber. Thus we have produced samples with a 10 nm iron layer and 50 and 100 nm gold layer using the shutter. For this series of measurements, **sample #5** was used (see Tab. 3.5, Page 71). The external magnetic field was driven to saturate magnetization in the ferromagnetic layer ($\approx$ **30 Gauss**). The time range for the pump-probe was set from **-0.5** to **2.0** picoseconds.

4.3.1 Discussion of the results

We have recorded three different signals during each run of the measurements:

- $\Delta E_{even}(t)$: non-magnetic SHG (see Section 2.3.5, Page 16)
- $\rho(t)$: magnetic SHG
- linear reflectivity (see Section 2.3.1, Page 11)

Non-magnetic SHG

The non-magnetic SHG signal yields information about the electronic transport from the moment of excitation ($t = 0$ ps). The signal is distinguished by a strong peak shortly after delay which increases steeply but recovers on a longer time scale. The peak results from a sudden changes in the electron energy distribution below the surface caused by ballistic carriers excited from the ferromagnetic layer reaching the gold surface. The charge density remains unchanged, however, since any surplus charge from the ballistic carriers is compensated by carriers with energies around E_F. The relaxation

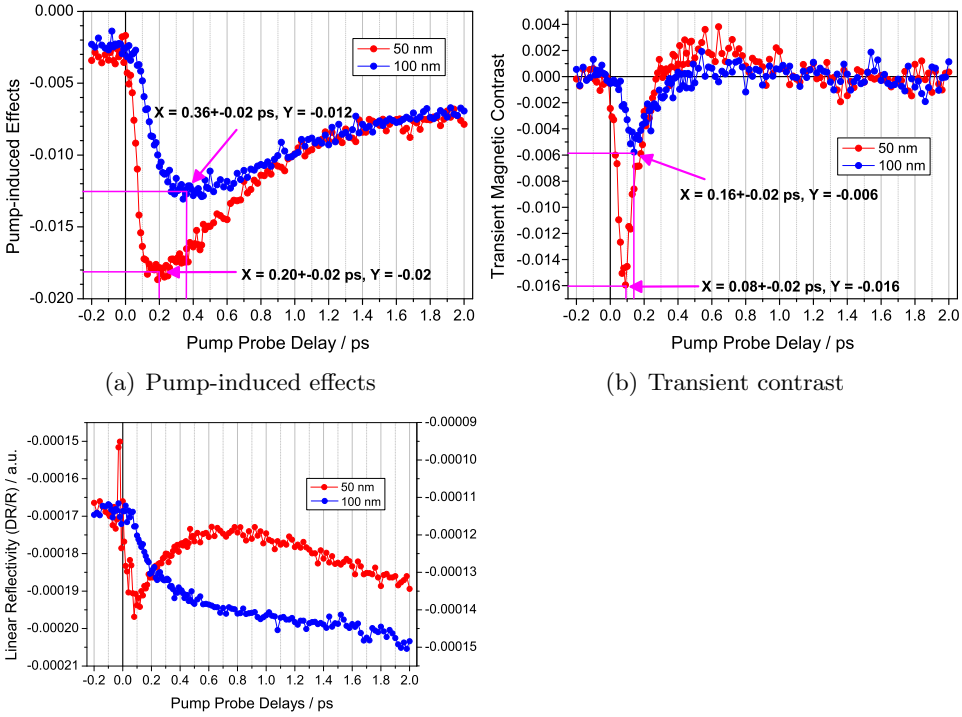

(a) Pump-induced effects

(b) Transient contrast

(c) Linear reflectivity

Figure 4.4: Result plots for the pump-induced effects (a), transient magnetic contrast (b) and the linear reflectivity (c) for **50** and **100 nm** gold layers. The ballistic carriers change the energy distribution at the gold surface which is detected in a change of SHG intensity. From the time scale we can read the average time that the have carriers travelled since excitation. Plot (a) does not distinguish between majority and minority carriers. This can be seen in the transient contrast plot (b) which is proportional to the surface magnetization. The signal is characterized by a short peak resulting from the ballistic, minority carriers and by an change of sign and overshoot caused by the majority carriers which travel diffusively (see text). The linear reflectivity show the bulk dynamics at the same time. It also show that the zero delay is set correctly for both thicknesses.

into energy ground states takes place on a longer time scale than perturbation from the carrier injection which explains the asymmetric shape of the peak. The intensity of the peak and its position on the time axis depend heavily on the thickness of the gold layer. For a **50 nm** gold layer, the peak has its maximum at $\approx$ **200** $\pm$ **20** femtoseconds, the intensity reaches up to **2 percent** of the total intensity. For **100 nm**, the peak is shifted to $\approx$ **360** $\pm$ **20 fs** and has a reduced relative intensity of around **1.25 percent**. The explanations for both effects are obvious. A thicker gold layer means, of course, that the path for the carriers to the surface is longer and thus the longer they take to reach the gold surface. On the other hand means a thicker gold layer that the carriers experience more electronic scattering within the crystal. If the gold layer is too thick, more carriers will be subject to diffusive transport rather than ballistic transport and the signal peak "smears out".

Magnetic SHG

The results in the magnetic component show that there are clearly two types of carrier transports possible. We have identified these to be **ballistic** and **diffusive**. Ballistic here means that the carriers travel through the gold layer with minimal scattering as a small packet. Due to this nature of ballistic transport, they reach the gold surface after a very short time upon excitation (**80** $\pm$ **20 fs** and **160** $\pm$ **20 fs** for **50 nm** and **100 nm** of gold respectively). The ballistic carriers can be identified are the minority carriers from the excitation spectrum for iron in Fig. 4.5. This "ballistic" peak is compensated shortly thereafter by the majority carriers from the **diffusive** transport. This means, that the magnetization will not only compensate to zero but also an **overshoot** is detected (thus these are the majority electrons). The diffusive carriers from larger packets than the ballistic carriers which is marked by a much broader peak of the magnetization. Since they are also much slower than the ballistic carriers (Fig. 4.5), the magnetization takes much longer until it recovers to zero. Figure 4.6 illustrates the two types of transport of the minority and majority carriers and the resulting magnetization.

Linear reflectivity

The linear reflectivity reflect the bulk dynamics in the gold layer. The reflectivity for **50 nm** shows a similar curve like the non-magnetic SHG component: a first pronounced peak followed by decay indicates that there is again ballistic transport followed by diffusive carriers. For **100 nm**, the peak from the ballistic transport is no longer visible which arises from the fact that the too many ballistic carriers have scattered in the bulk to be detectable in the linear reflectivity signal. The proper zero delay is also

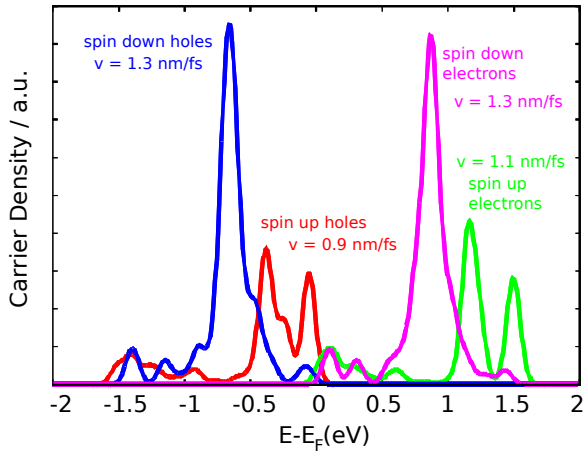

Figure 4.5: Excitation spectrum for iron. There are four types of carriers which can be excited from iron. Spin-up holes (minority holes), spin-down holes (majority holes), spin-up electrons (minority electrons) and spin-down electrons (majority electrons). The carriers are excited from different bands in the energy spectrum of iron and have therefore different velocities after excitation. The spectrum shows that the carrier densities for spin-down carriers are higher than the ones for spin-up carriers. This explains the why spin-down form the majority and spin-up the minority densities.

verified from this signal, as the peaks from the coherence artifact appear at $t = 0$ ps.

4.4 Longtime: electronic vs. phononic

The first variation in the experimental scheme that we made within the context of this thesis was that we were repeating the original experiment but on a much longer timescale. In previous measurements, the timescales for the pump-probe delay usually ranged between **-0.5** and **3.0** picoseconds. In this series of measurements we have extended the range to up to **500** picoseconds. The motivation behind this is that we expect more effects other than spin and electron dynamics on the longer timescale, namely the lattice dynamics or phononic transport. Since the excited hot carriers have high velocities high above the Fermi energy (around $v_F = 1$ nm/fs, see Fig. 4.5), they reach the gold surface after short delays. Lattice deformations propagate through the crystal with the velocity of sound ($v = 3.24$ nm/fs). Since lattice deformations do not change the equilibrium between majority and minority carriers, we do not expect any variations in the magnetic channel. Again, **sample #5** was used and the other parameters are identical to the previous shorttime measurements.

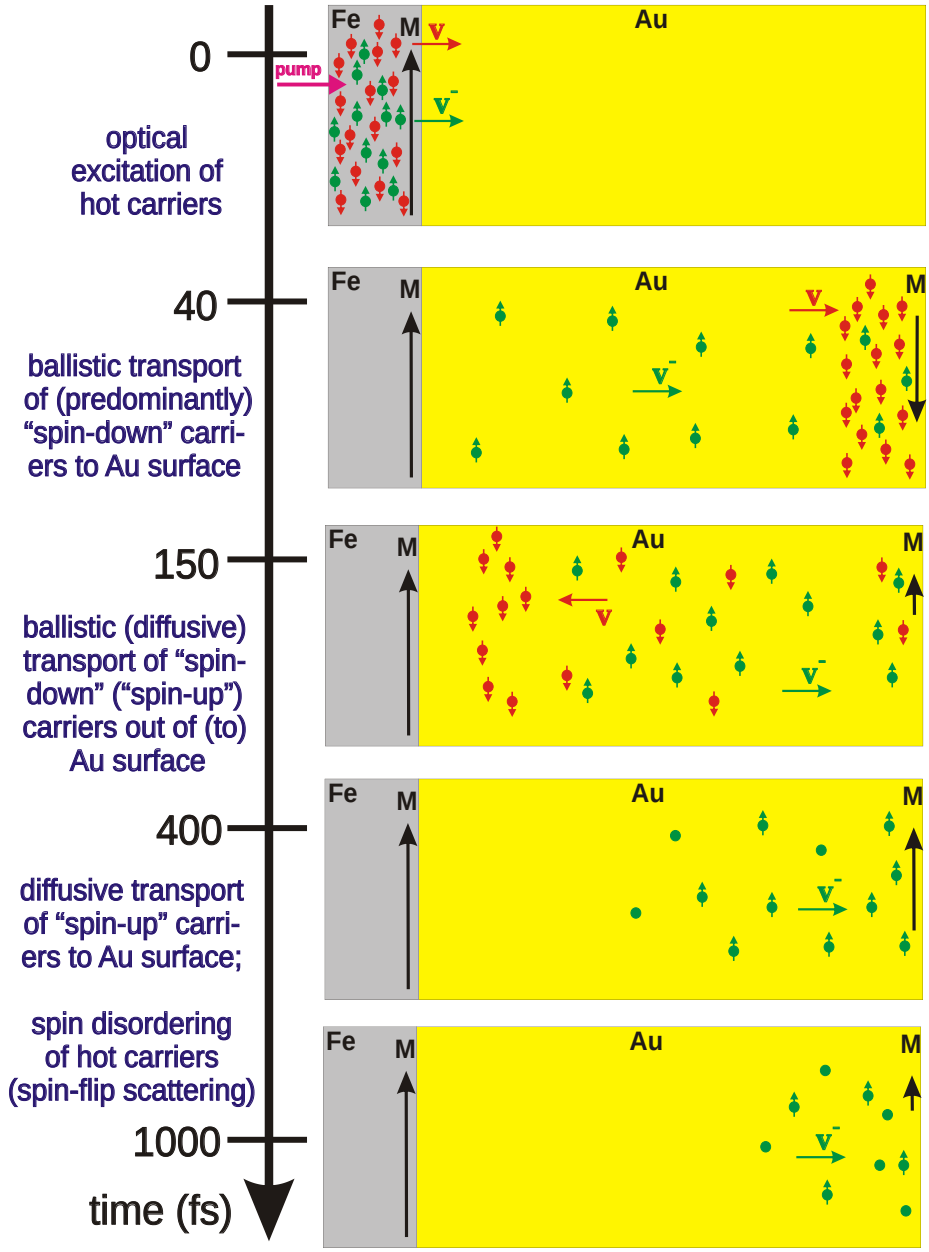

Figure 4.6: Illustration two types of the carrier transports within the gold layer after excitation. While the **ballistic** carriers (minority) reach the gold surface after only **40 fs**, the **diffusive** carriers (majority) take **150 fs** and more to reach the surface and to flip magnetization. After more than **1000 fs**, all electrons will have distributed within evenly and magnetization levels to zero.

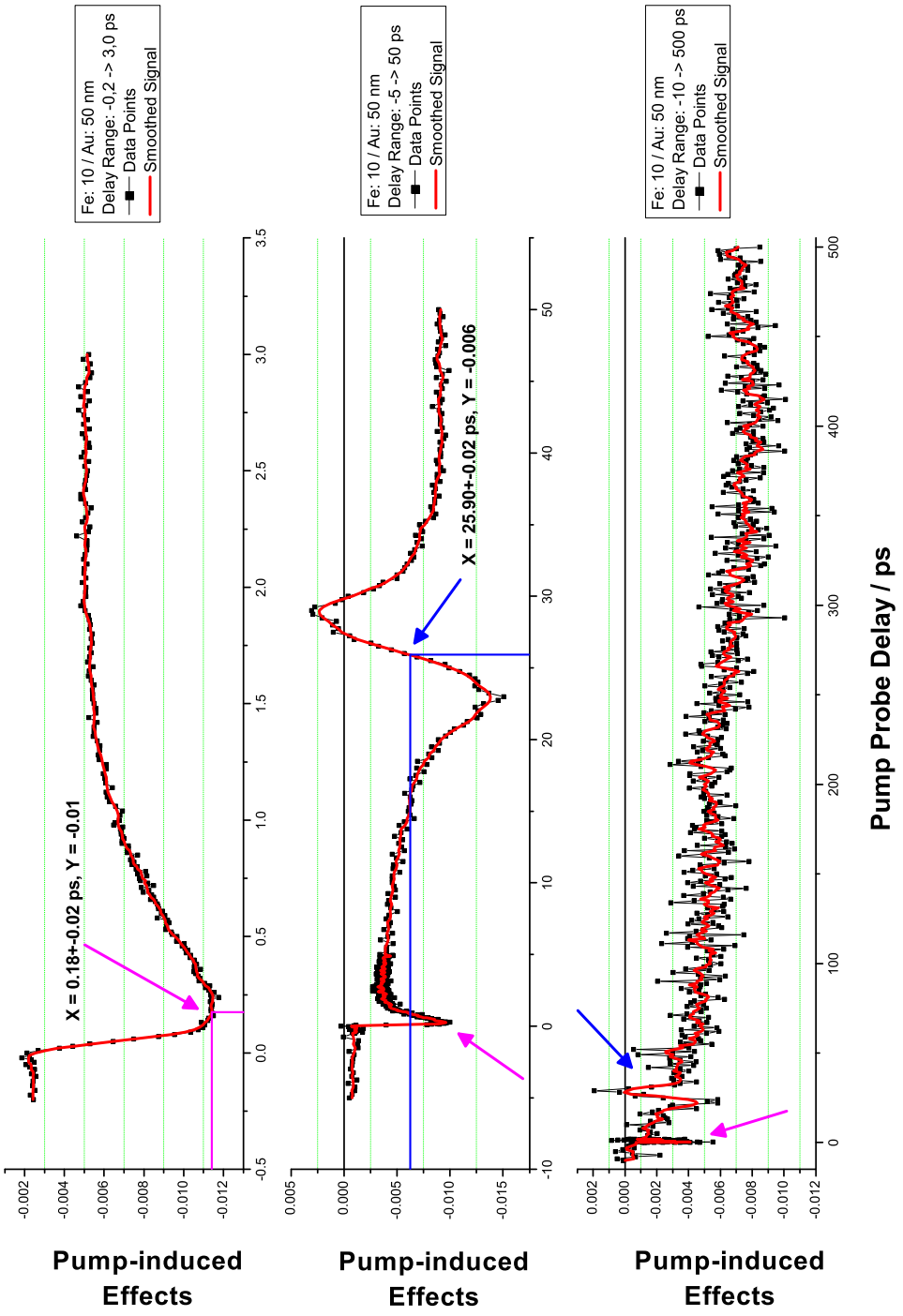

Figure 4.7: The non-magnetic part of the SHG signal shown on different time scales: **(a): -0.5-3.0 ps**, **(b): -0.5-50.0 ps** and **(c): -0.5-500.0 ps**. The curves in (a) are almost identical with the results from the shorttime measurements. However, the effect is less pronounced here (only around **1.2** percent compared to the **2.0** percent). The peak still arrives at around **180 fs**. Looking at the two longtime runs, an additional of two peaks can be distinguished at a delay of ≈**26 ps**. This results from lattice dynamics (see text).

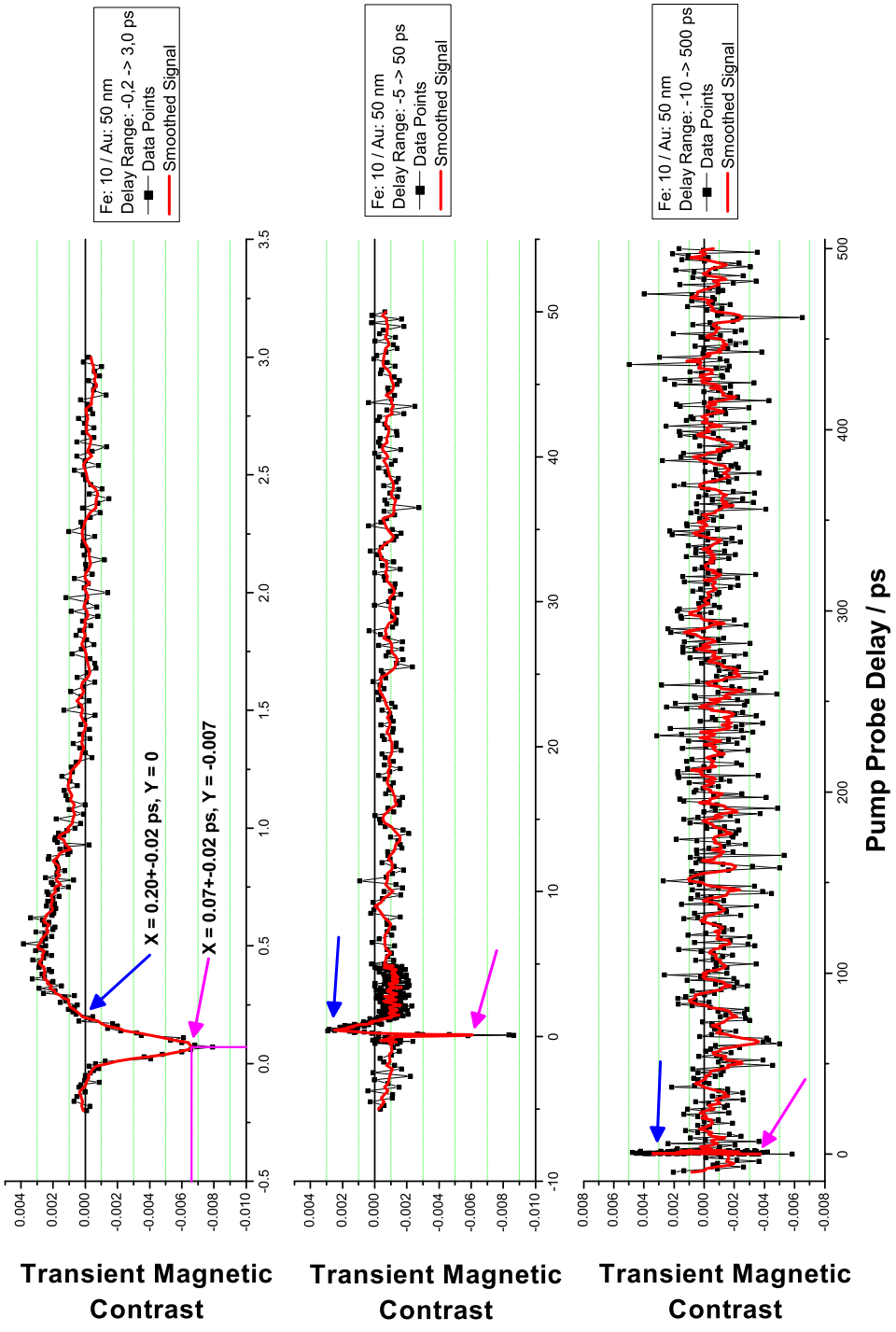

Figure 4.8: The magnetic component of the SHG signal does not show any further effects even on longer time scales. While we can see two additional peaks from the shock wave resulting from the lattice vibrations after excitation in the non-magnetic part, there are no further changes in the surface magnetization after the initial ballistic peak and the accompanying overshoot.

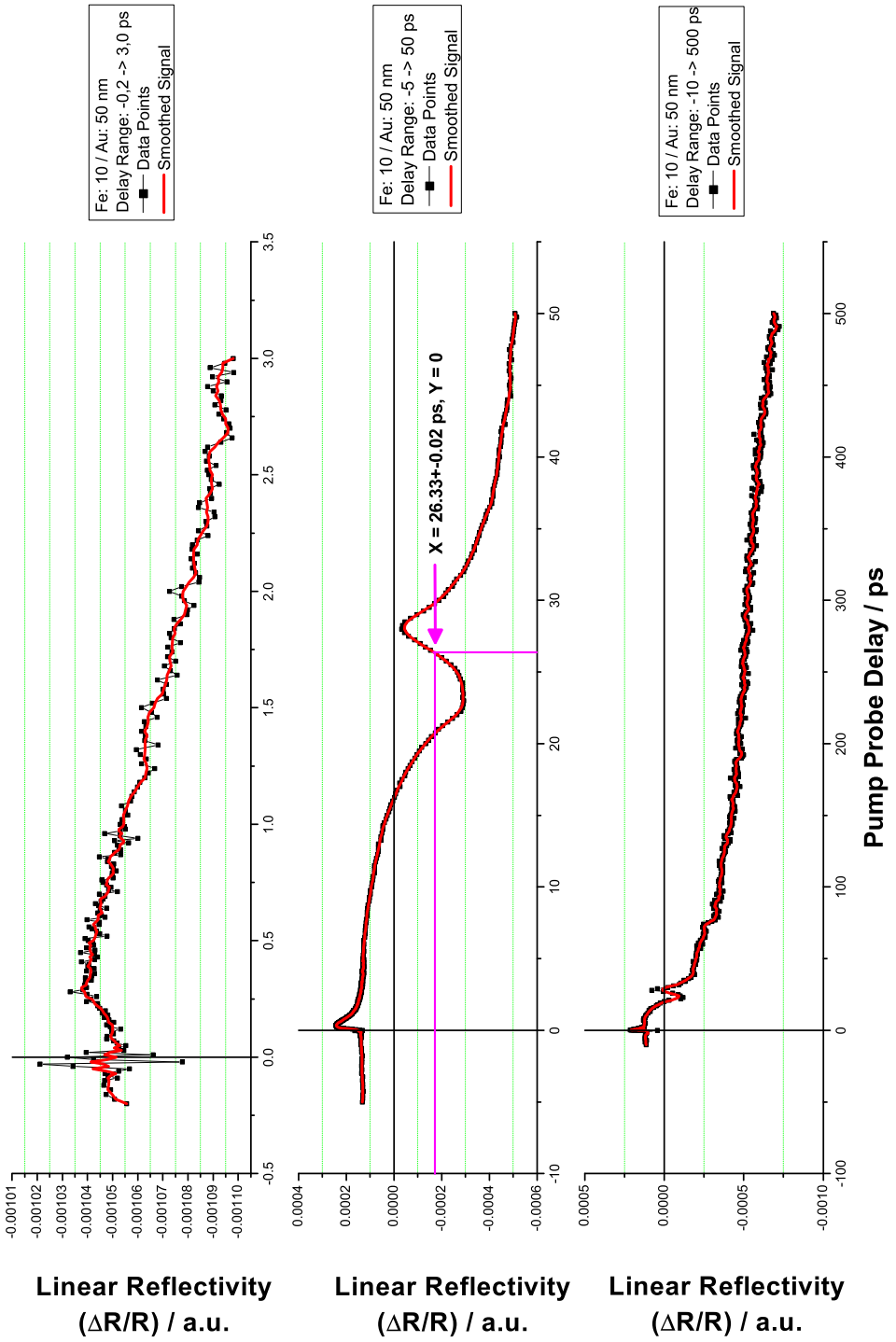

Figure 4.9: The linear reflectivity shows the same additional two peaks at ≈**26 ps** like they already appeared in the non-magnetic component of the SHG signal at the same time. Scanning on the longer time range of **500 ps** does not reveal any further peaks. However the signal should recover on even longer time scales. The coherence artifact at $t = 0$ ps indicates a proper set zero delay.

4.4.1 Discussion of the results

From the result plots in 4.7-4.9 we see what happens on longer time scales. Two additional peaks can be distinguished at a delay of **26 picoseonds**. This peaks results from a acoustic pulse triggered by a lattice deformation the gold layer after injecting the electrons from the iron layer. From the propagation time and the thickness of the gold layer, we can calculate the velocity of the acoustic pulse which is around 1923 **m/s**. The lattice vibrations or *phonons* do not induce changes in the spin equilibrium and therefore is no visible peak in the magnetic SHG component. The measurement of the linear reflectivity is sensitive enough to detect the acoustic pulse, too, as opposed to the initial ballistic peak which can only be seen in the non-magnetic SHG measurement. The acoustic pulse is detected in the linear reflectivity at the same delay as it is in the non-magnetic SHG.

4.5 Wedge: thickness dependency

The idea of the wedge was to be able to conduct a systematic analysis of the thickness dependence of the electron and spin dynamics. With this analysis, we would be able to determine the velocity of the ballistic and diffusive electron and spin transport and compare these velocities with the calculated values from theory. The production of the wedges is discussed in Section 3.5, Page 43 which also elaborates the motivation behind the wedge concept. **Sample #5** was used (see Tab. 3.5, Page 71) and the external magnetic field was driven to saturate magnetization in the ferromagnetic layer ($\approx$ **30 Gauss**). The time range for the pump-probe was set from **-0.2** to **3.0** picoseconds. The sample was moved with the micrometer screws of the sample holder in order to measure at gold thicknesses of **50**, **60** and **70** nanometers. To calibrate the displacement of the sample with the current thickness of the wedge, we used the results from the evaporation process of the wedges.

4.5.1 Discussion of the results

The wedge measurements did not yield the expected results. It was much more difficult to maintain the alignment (time- and spatial overlap and zero delay) while moving to higher thicknesses than we thought. The stability of the new sample holder is still not sufficient so that an automated sweeping of the thickness by translation of the sample along the wedge could be performed[1]. For the first attempt we have swept the thickness over a range of **20 nm** only, which corresponded to a lateral translation of the sample of approximately **1.62 mm** which was already enough impair the alignment

[1] Albeit the fact that the setup still doesn't have a motorized stage but has to be translated manually with the micrometer screws.

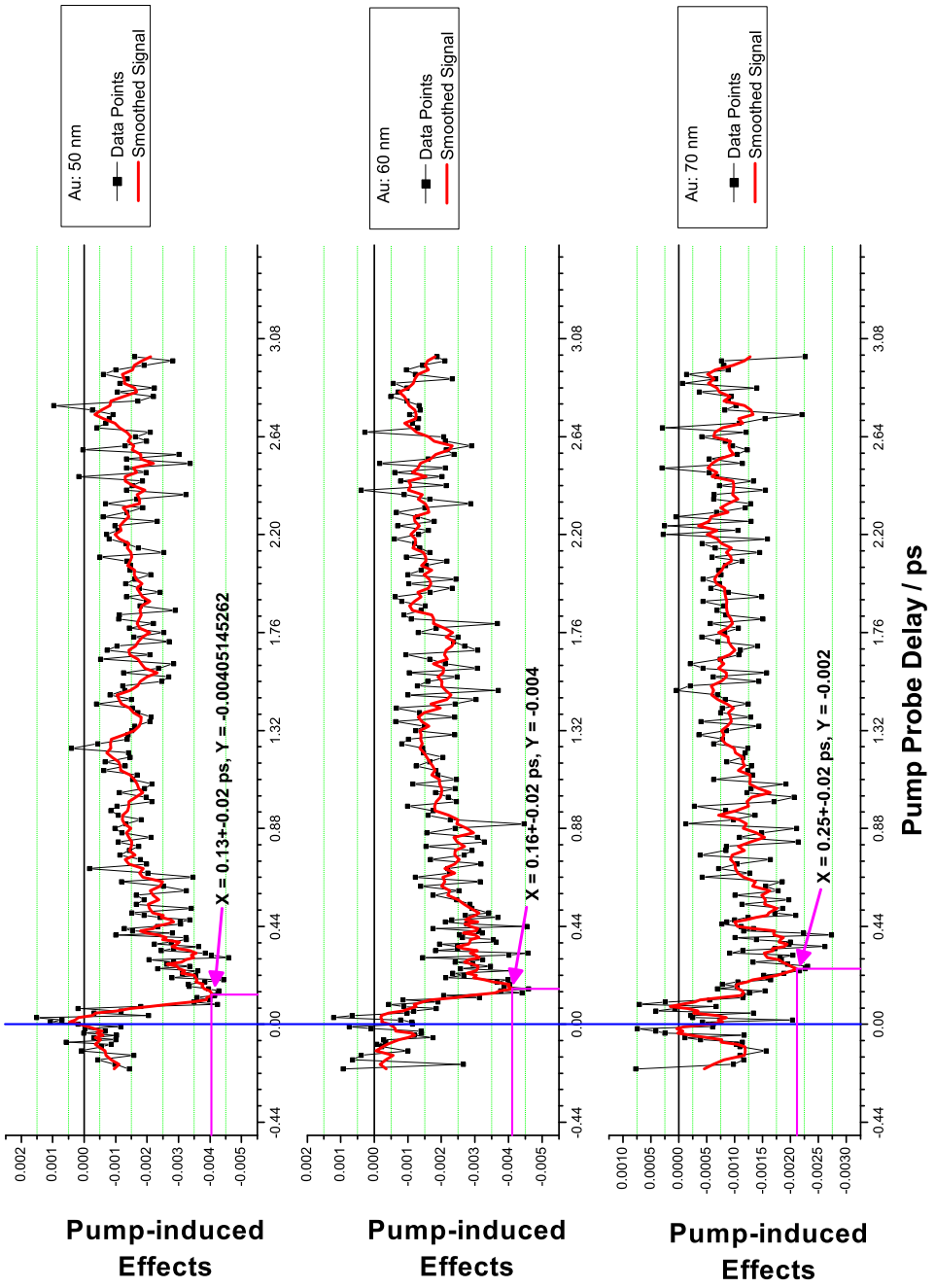

Figure 4.10: Pump-induced effects for different thicknesses along the wedge. The peak with the local maximum is shifted from **130** (50 nm) over **160** (60 nm) to **250** femtoseconds (70 nm) as one would expect for increasing thicknesses. The results for 70 are very noisy, however, as alignment was relatively poor during this measurement (zero delay, time/spatial overlap).

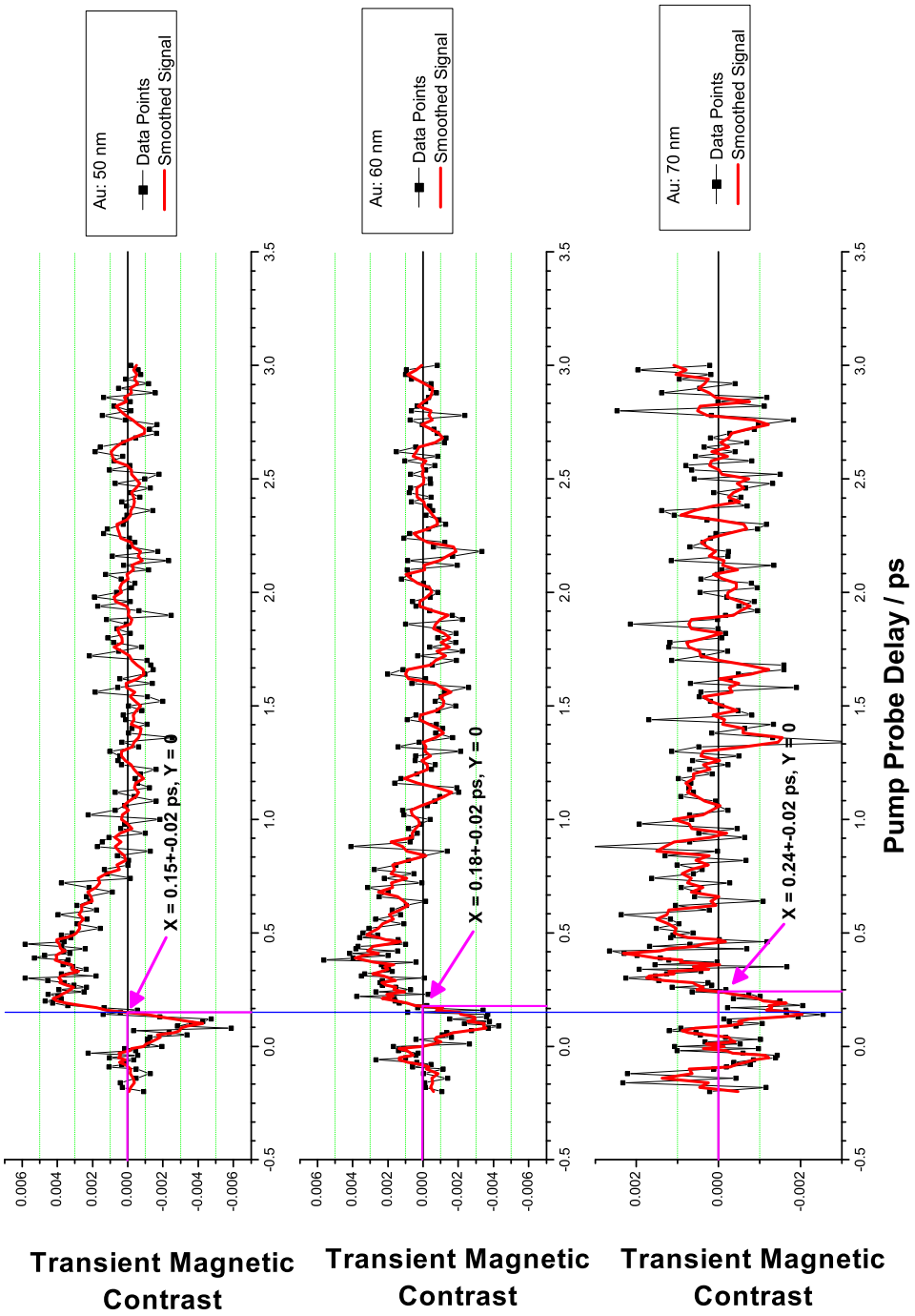

Figure 4.11: Dynamic contrast for different thicknesses along the wedge. We have used the zero crossing of the magnetization due to the overshoot from the diffusive electrons as a mean to determine the propagation time. The zero crossing is shifted from **150** (50 nm) over **180** (60 nm) to **240** femtoseconds (70 nm). Again, the signal for 70 nm is very noisy due to the poor alignment.

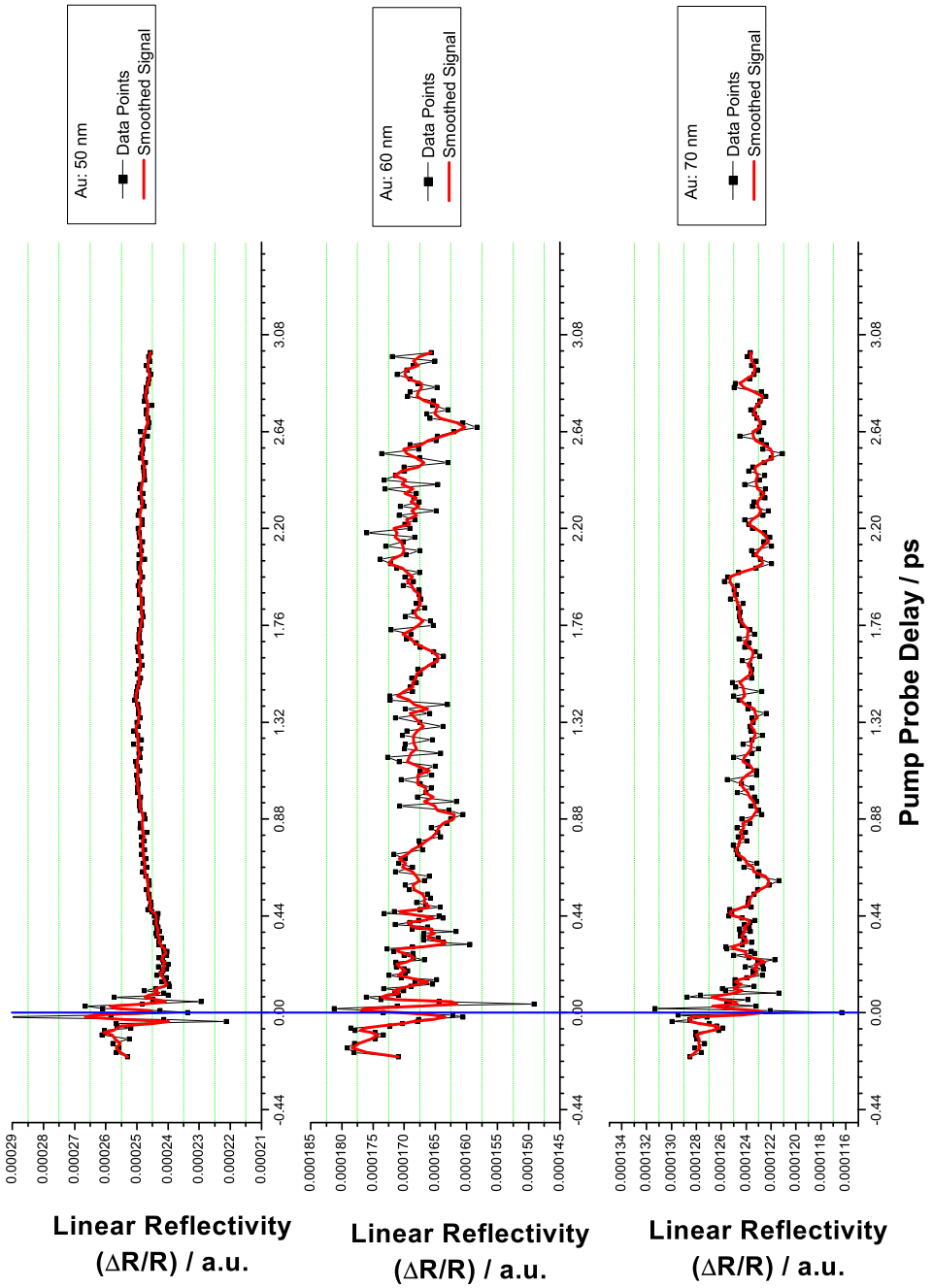

Figure 4.12: Linear reflectivity for different thicknesses along the wedge. The zero delay is definitely properly set for **50 nm** as the distinguishable coherence artifact lies at $t = 0$ fs while the rest of the signal is rather flat. For **60** and **70 nm**, however, we're picking up too much noise thus we cannot be sure that we are still at the proper zero delay since the coherence artifact might blur within the noise.

such that the results obtained should be considered with care. However, the trend of the ballistic peak in non-magnetic SHG and the zero crossing of the mSHG component shifting to later times is definitely there. At least, for the thicknesses **50 nm** and **60 nm** the shift of the characteristic data points that we have used to determine the propagation time matches both in the magnetic (Fig. 4.10)and non-magnetic (Fig. 4.11) signal: **3 fs**. The difference between **60 nm** and **70 nm** is approximately **6 fs** for the non-magnetic and **9 fs** for the magnetic component, so this datapoint should be rather discarded. Unfortunately, we could not achieve a stable signal for even higher thicknesses so that we were unable to measure any sensible signal. Thus, in order to perform more reliable wedge measurements, the stability of the alignment has to be improved further.

4.6 Linear MOKE: alternative access to spin dynamics

Besides the measurements with the advanced SHG techniques, we have also performed conventional linear MOKE measurements to be able to compare them with our method of choice, mSHG. The MOKE measurements provide information on bulk spin dynamics analog to the linear reflectivity which yields bulk electron dynamics. While we measured mSHG with the field applied in transversal geometry (inner coils), for MOKE we chose the longitudinal configuration (outer coils). This has to be kept in mind when comparing our mSHG and MOKE results. However, since the non-magnetic part of the SHG signal can be measured in both geometries, we had a mean to verify that the observed effect is comparable in both configurations: If the geometry had any considerate influence on the SHG signal, it should reflect in the non-magnetic component also. The plots for non-magnetic components can be found in Figures 4.13 (d) and (e).

4.6.1 Discussion of the results

The bulk spin dynamics analyzed with MOKE in (4.13 (a) and (b)) show different results when comparing to the mSHG signal. The first striking difference is that there is no peak (purple arrows) from the ballistic carriers, both for **50 nm** and **100 nm** gold layers. The overshoot from the diffusive transport (blue arrow) is, however, detected. We haven't found yet any reasonable explanation for this behavior but one can speculate: One possible scenario is that the different penetration depths of the sensitivity (see Sections 2.3.2, Page 12 and 2.3.3, Page 14) might be related to that issue. Since the ballistic carriers form small packets the magnetization is concentrated within a small space whereas the majority carriers from diffusive transport occupy larger spaces and thus their magnetization. And since

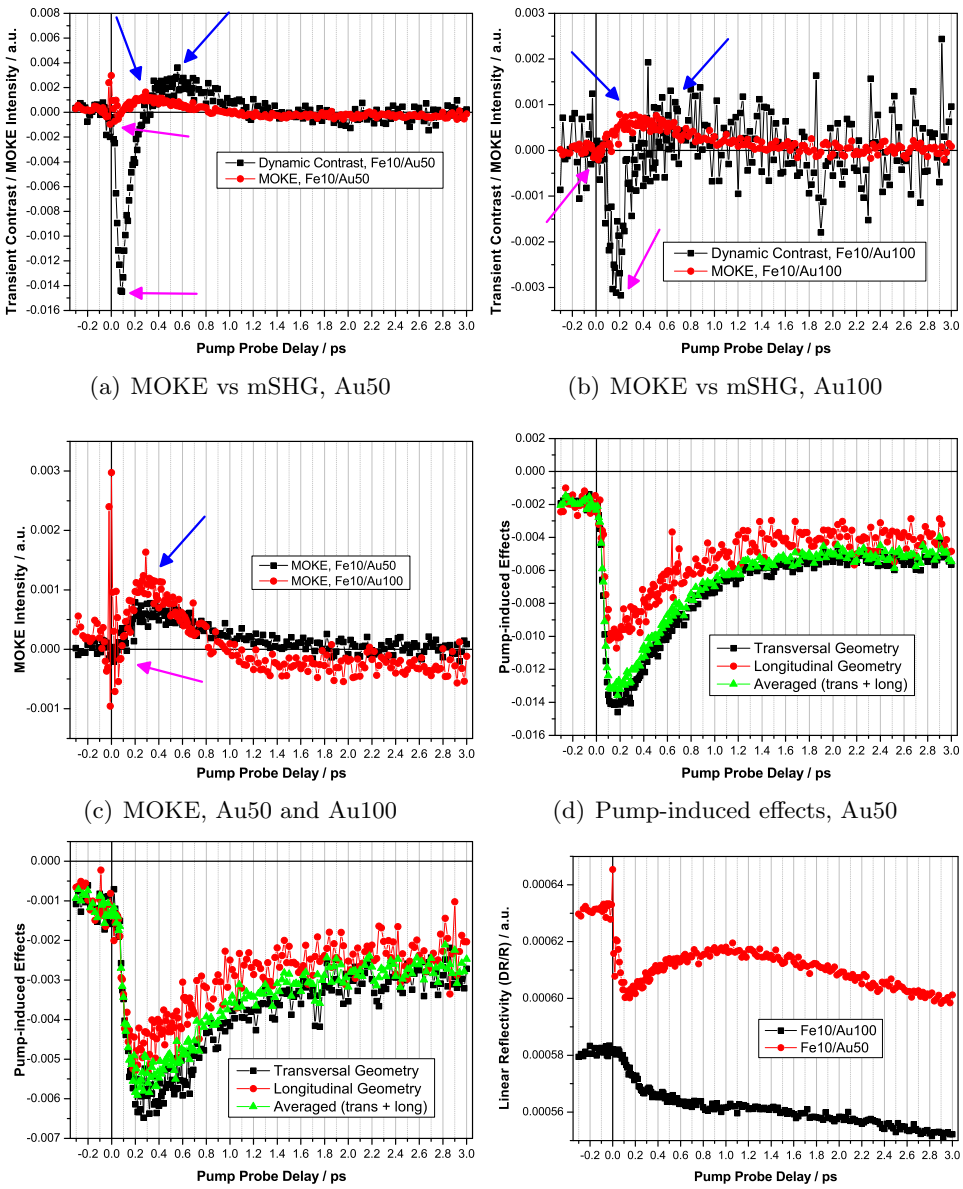

(a) MOKE vs mSHG, Au50

(b) MOKE vs mSHG, Au100

(c) MOKE, Au50 and Au100

(d) Pump-induced effects, Au50

(e) Pump-induced effects, Au100

(f) Linear Reflectivity

Figure 4.13: Comparison of the results for MOKE and SHG measurements. The MOKE measurements were performed in **longitudinal geometry**. Comparing the MOKE measurements with the magnetic SHG measurements in **(a)** and **(b)** one can clearly see that the first peak (purple arrow) from the ballistic carriers is not visible in the MOKE signal while we can still observe the overshoot from the diffusive transport (blue arrow). The ballistic peak is missing both for **50** and **100 nm** scans **(c)**. Since the non-magnetic signal is independent from the external magnetic field, we can use these results to in **longitudinal** and **transversal** geometry of the external field are comparable **(d)**. The same applies for the linear reflectivity **(e)**.

MOKE is bulk-sensitive (as opposed to the surface sensitivity of mSHG) it has larger response functions for magnetizations within large spatial than for magnetizations within a surface or interface. The plot in 4.13 (c) compares the MOKE signal for different thicknesses of the gold layer, 50 and 100 nm. The overshoots (blue arrow) for 50 and 100 nm and the ones from the measurement of the magnetic component in 4.4 (b) are on comparable time scales, however the overshoot for 50 nm has a higher intensity than the one for 100 nm in the mSHG measurement while this is the opposite case for MOKE. Since the difference between 50 and 100 nm is rather small, this might rather be an artifact than a real effect. The ballistic peak would yield more information if it was detectable with MOKE. The plot for linear reflectivity in 4.13 shows the same dynamics as found for the shorttime measurements.

Chapter 5

Conclusion & Discussion

In the this work we have introduced a new concept to switch magnetizations in ferromagnetic materials. Instead of using external magnetic fields produced by coils or other ferromagnetic materials, we inject spin-polarized carriers directly. These hot carriers are excited from a magnetized ferromagnetic layer and thus form a spin-polarized current. The spin-polarized current passes a non-ferromagnetic spacer layer over several transport mechanisms which we have investigated in this work and change, what has not been achieved yet, the magnetization in a second ferromagnetic layer.

The model systems that we have perceived for this setup are made from crystalline, dual-side polished magnesium oxide substrates (MgO (001)) on which metallic multi-layers are grown epitaxially by means of evaporation in ultra-high vacuum environment. A layer of 10-20 nanometers of iron serves both as the source for spin-polarized electrons as well providing a buffer layer to improve epitaxial growth of the overlaying gold layer. The gold layer, usually 50-100 nanometers in thickness, provides a non-ferromagnetic spacer medium to separate a second iron layer. This is the target layer, whose magnetization is altered by the spin-polarized carriers generated in the source layer. Before the actual switching by spin injection can be performed, however, we had to perform a lot of preliminary research to understand ultrafast magnetization and spin dynamics, i.e. the transport mechanisms of the carriers in the metallic multilayers. For this, we have reduced our model system to a *MgO(001)/Fe/Au* bilayer setup thus neglecting the target ferromagnetic layer for now.

To generate spin-polarized electrons in the source ferromagnetic layer, an external magnetic field is first applied to drive the magnetization in the specimen into saturation, then a femtosecond laser excites "hot electrons" by pumping the sample from the backside. Due to the magnetization in the source layer, there are more electrons with one spin orientation (majority electrons) than with opposite orientation and the flow of electrons becomes spin-polarized. After excitation the electrons have sufficient kinetic energy

so that they enter the gold spacer layer. Since the *majority* and *minority* have different energy bands within gold, their velocities and transport mechanism are *different*. Within the framework of this project we were able to demonstrate that.

The first focus of this thesis was put on the techniques of producing the samples ourselves by means of molecular beam epitaxy and investigating what factors have a direct influence on the results of the core experiments. In order to achieve best possible sample qualities, we have varied different evaporation parameters like substrate temperatures, evaporation rates and annealing procedures. To conclude these, we have found out that the films should be evaporated at lowest possible substrate temperatures (usually room temperature), lowest possible evaporation rates and the substrates themselves need to be thoroughly cleansed and annealed to remove as much contamination as possible and maintain high substrate purity. Good quality films are desirable to reduce optical scattering of the laser at the sample surfaces and electron scattering at Fe/Au interfaces.

The second focus of this thesis was to continue the investigations performed in the core experiment, that is the SHG measurements. Within the framework of this thesis we have extended the time range of the pump-probe delay to observe electronic and spin transport on a longer time scale after excitation. In fact, we were able to monitor lattice dynamics of the gold as acoustic waves as a result of lattice deformations triggered by heat resulting from the carrier injection. There were, however, no effects visible in the magnetic component of the SHG probe signal.

We have also performed conventional linear MOKE measurements to monitor the bulk spin dynamics. The results were distinct from the mSHG results. Like the measurement of the bulk electron dynamics with linear reflectivity, we were able to detect the majority carriers, but the sharp peak resulting from the minority electrons (ballistic) was not visible at all. We presume that the packets formed by the ballistic carriers are to small to induce enough changes in the bulk magnetization to be detected by MOKE. This would also explain, why the overshot from majority spins is still detectable.

In an additional experiment, we wanted to determine the velocities of both the ballistic and diffusive transport mechanisms directly. For this, we created a gold wedge in the evaporation process and installed the sample into a displayable sample holder. Unfortunately, we weren't yet able to design a sample holder that was stable enough to maintain proper optical alignment and beam overlap while moving the sample between the measurements. Therefore, the experiments didn't yield any truly usable results to determine the velocities. We can say though, that the results show that there is a trend that clearly suggests a shift of the peaks towards longer

times for higher thicknesses. We think, that a more reliable sample holder with a motorized stage will not only yield better alignment but also allow a completely automated measurement for the wedge to finally determine the electron velocities and compare them with theory.

Finally, we have realized that there is still a long way to go and more caveats have to be ruled out until we can perform the experiments which we have originally perceived, namely the switching of magnetization by injection of spin-polarized "hot electrons". However, we have shown that such experiments are generally feasible and we have already successfully tackled the first obstacles to finally reach our goal.

Appendix A

Engineering Drawings

The following engineering drawings were created using the open-source CAD-software *qcad*, version 2.2.0 (see [38]). All scales are in millimeters, screws used are in metric dimensions ("M x"). Material is either high-graded steel or aluminium as indicated in the drawings. Shaded areas indicate the metal parts; drilled holes or threads are indicated with solid fill. Large blank areas indicate larger apertures. These drawings were actually used to handcraft the parts or file them to the departments precision engineering group.

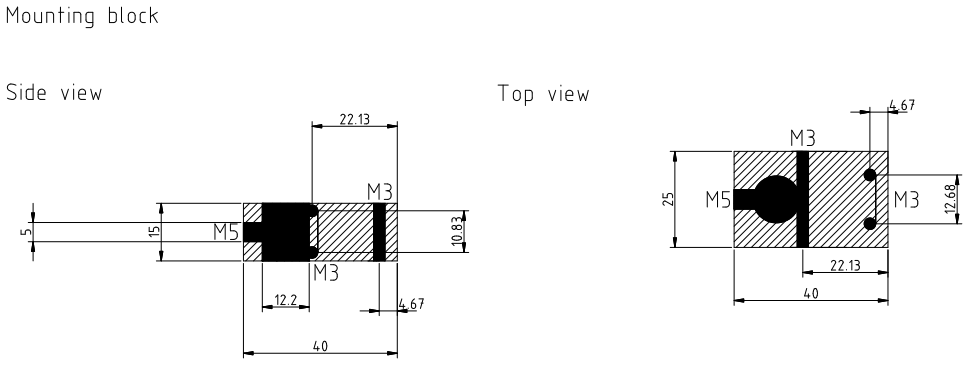

Figure A.1: Helmholtz Coils - Mounting Block

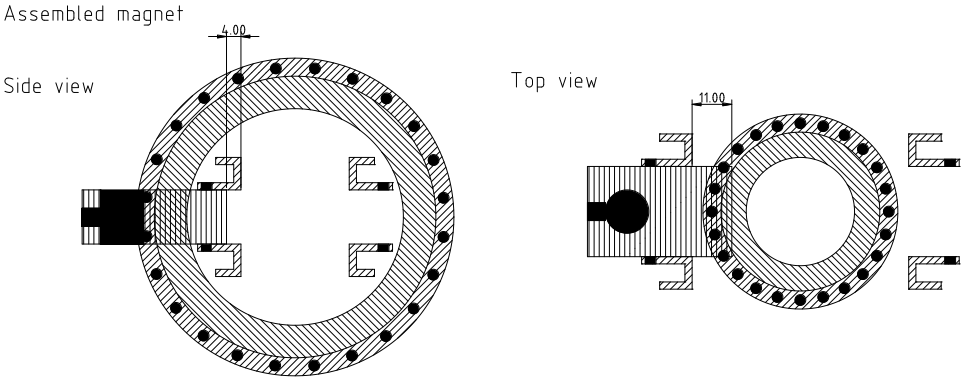

Figure A.2: Helmholtz Coils - Assembled View

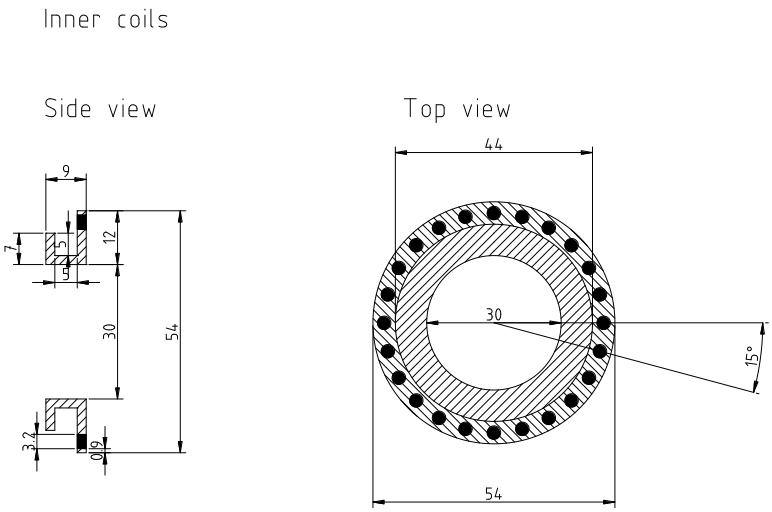

Figure A.3: Helmholtz Coils - Inner Coils

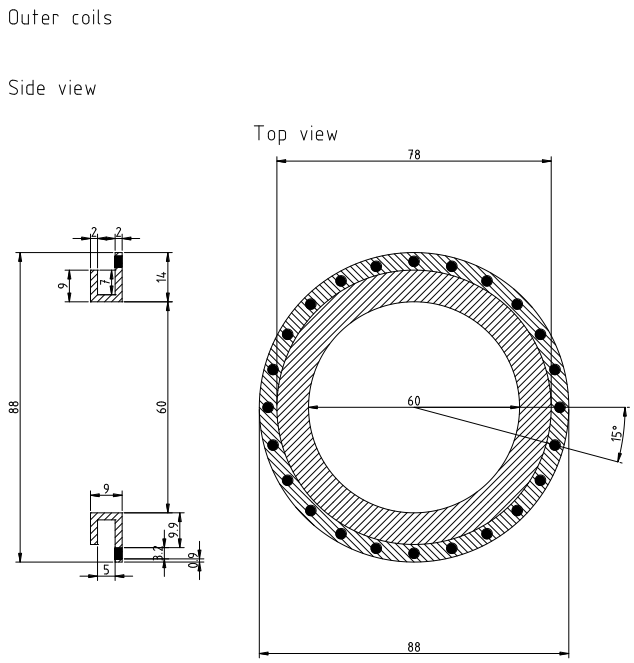

Figure A.4: Helmholtz Coils - Outer Coils

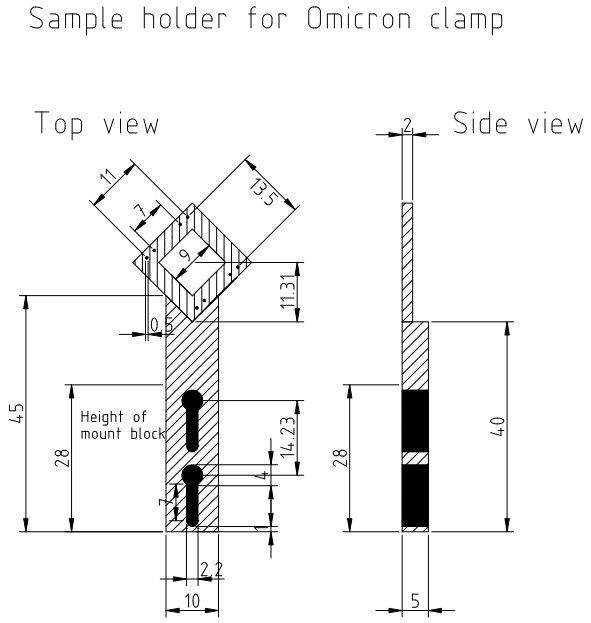

Figure A.5: Sample holder for positioning the samples in the magnet

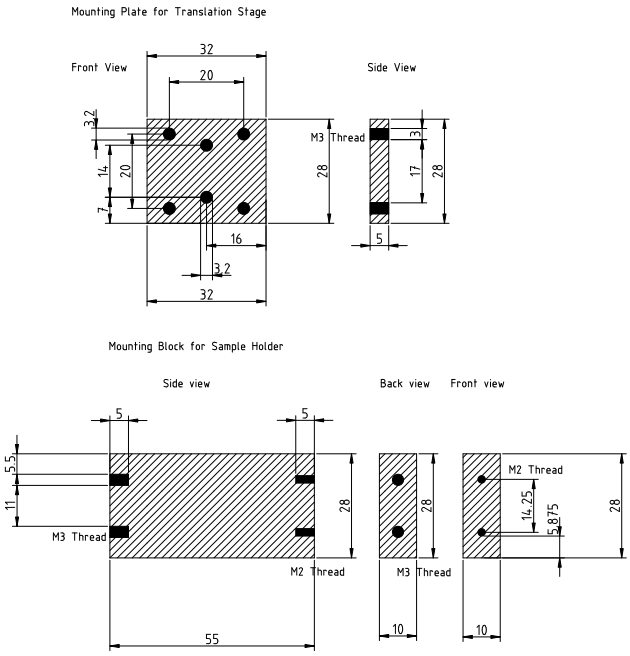

Figure A.6: Sample Holder - Mount Assembly

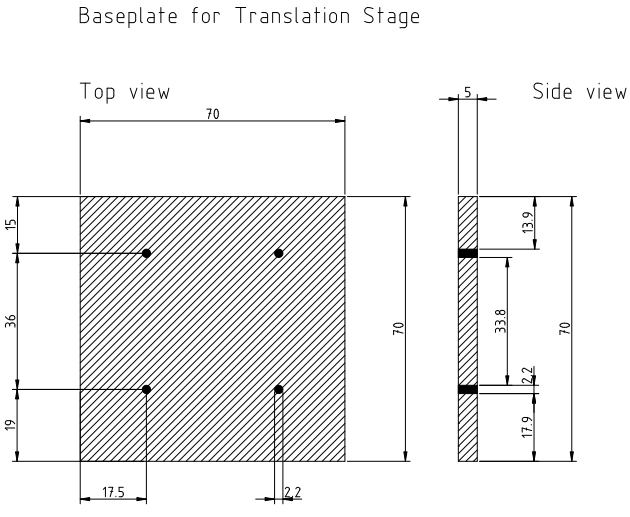

Figure A.7: Sample Holder - Base plate for Translation Stage

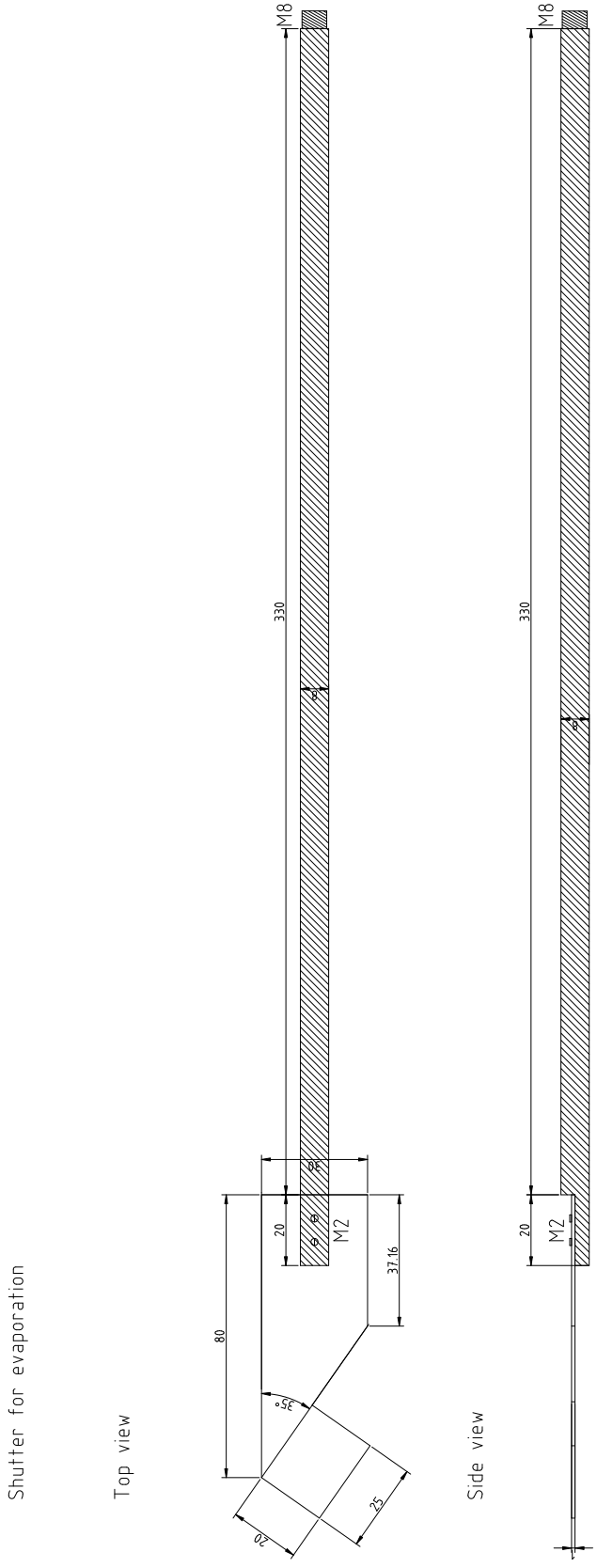

Figure A.8: Shutter used for evaporation

Appendix B

Source code of autocorrelation program

```
1  /* autocorr.c - program code for autocorrelation analysis of
       grain size of STM images */

3  #include <stdio.h>
   #include <string.h>
5  #include <math.h>

7  /* Number of lines in data files exported from wsxm */
   #define NLINES 160000
9
   /* Number of points per line */
11 #define NPOINTS 400

13 /*
    * array data:
15  * X - distance of point on X-axis
    * Y - distance of point on Y-axis
17  * Z - elavation of point at x,y
    */
19 double x[NLINES], y[NLINES], z[NLINES];

21 /* parse - read in data file exported from wsxm
   *          and store data into glocal arrays
23 */
   int parse(char * filename)
25 {
     int i;
27   FILE* file;
     char buf[100];
29
     if ((file = fopen(filename, "r"))) {
31
       for (i = 0; i < 4; i++)
33       fgets(buf, 100, file);
```

```
35      for (i = 0; i < NLINES; i++) {
          fscanf (file ,"%lf %lf %lf", &x[i], &y[i], &z[i]);
37      }
    }
39  }

41  /* autocorr - actual function to perform autocorrelation on
        image data */
    int autocorr() {
43
      /* variables:
45     *
       * ac - autocorrelation for each point
47     * n - holds the amount occurrences for each distances
       * i,j - loop indices
49     * s - mean value of z-elevation
       */
51
      double ac[NPOINTS];
53    unsigned long long n[NPOINTS];
      int i, j, r;
55    double s;

57    s = 0;

59    /* make sure buffers are zeroed */
      memset(ac, 0, sizeof(ac));
61    memset(n, 0, sizeof(n));


63
      /* calculate mean */
65    for (i = 0; i < NLINES; i++)
        s = s + z[i];
67
      s = s / NLINES;
69
      /* substract mean from z-data */
71    for (i = 0; i < NLINES; i++)
        z[i] = z[i] - s;
73
      //    for (i = 0; i < NLINES; i++)
75    //    z[i] = sin (2*M_PI*x[i]/50) * sin (2*M_PI*y[i]/50);

77    for (i = 0; i < NLINES; i++)
        for (j = i; j < NLINES; j++) {
79        /* calculate distance of points at i and j index */
          r = round(sqrt((x[i] - x[j])*(x[i] - x[j]) + (y[i] - y[j])
              *(y[i] - y[j])));
81        /* count only distances which are smaller than a scan line
               */
          if (r < NPOINTS) {
83    /* increase count of this specific distance */
      n[r] = n[r] + 1;
```

```
85    /* calculate autocorrelation for this distance */
      ac[r] = ac[r] + z[i]*z[j];
87        }
        }
89
      /* normalize autocorrelations */
91    for (i = 0; i < NPOINTS; i++)
        ac[i] = ac[i]/n[i];
93
      /* output calculated AC data to terminal */
95    for (i = 0; i < NPOINTS; i++)
        printf ("%d\t%f\n", i, ac[i]);
97  }

99  int main (int argc, char** argv) {


101
      char filename [256];
103
      /* case-matching for the amount of arguments specified: */
105
      switch (argc) {
107
        /* if argc == 1 only the programname was specified during
            invocation,
109      * thus prompt for both operands/arguments
         */
111     case 1:
        printf ("\nNo arguments specified: \n\nInput filename: ");
113     scanf ("%s", &filename); /* scan input directly to integer
            */
        break;
115
      case 2:
117     /* if we got argc == 2, then we have one argument specified
            and will
         * now try to parse the filename, if this fails, we proceed
119      * to default: (no break) */

121     if (sscanf (argv [1], "%s", &filename) == 1)
          break;
123   default:

125     /* something we cannot interpret was specified on command
            line, print help
         * message and exit with error
127      */

129     printf ("\nUsage: %s filename\n\n", argv [0], argv [0]);
        return -1; /* Return with EXIT_ERROR (= -1) */
131   }

133   parse (filename);
      autocorr();
```

```
135
    return 0;
137
}
```

Bibliography

[1] B.Hillebrands and K.Ounadjela. *Spin Dynamics in Confined Magnetic Structures I.* Springer-Verlag Berlin, 2002.

[2] B.Hillebrands and K.Ounadjela. *Spin Dynamics in Confined Magnetic Structures II.* Springer-Verlag Berlin, 2003.

[3] B.Hillebrands and A.Thiaville. *Spin Dynamics in Confined Magnetic Structures III.* Springer-Verlag Berlin, 2006.

[4] P. Grünberg, R. Schreiber, Y. Pang, M. B. Brodsky and H. Sowers. Layered Magnetic Structures: Evidence for Antiferromagnetic Coupling of Fe Layers across Cr Interlayers. *Physical Review Letters*, 57:2442–2445, 1986.

[5] M.N. Baibich, J.M. Broto, A. Fert, F. Nguyen Van Dau, and F. Petroff. Giant magnetoresistance of (001)fe/(001)cr magnetic superlattices. *Physical Review Letters*, Volume 61, Number 21:2472–2475, 1988.

[6] Kai-Zhong Gao (Seagate Technology). Magnetic thin films for perpendicular recording. In *2009 APS March Meeting - MondayFriday, March 1620, 2009; Pittsburgh, Pennsylvania*, 2009.

[7] Ioan Tudosa. *Magnetization dynamics using ultrashort magnetic field pulses.* PhD thesis, Stanford University, 2005.

[8] Joachim Stöhr, Hans Christoph Siegmann. *Magnetism - From Fundamentals to Nanoscale Dynamics.* Springer-Verlag Berlin, 2006.

[9] J. C. Slonczewski. Current-driven excitation of magnetic multilayers. *Journal of Magnetism and Magnetic Materials*, 159(1-2):L1–L7, June 1996.

[10] M.D. Stiles D.C. Ralph. Spin transfer torques - current perspectives. *Journal of Magnetism and Magnetic Materials*, 320:1190–1216, 2008.

[11] M. Tsoi, A. G. M. Jansen, J. Bass, W.-C. Chiang, M. Seck, V. Tsoi, and P. Wyder. Excitation of a magnetic multilayer by an electric current. *Phys. Rev. Lett.*, 80(19):4281–, May 1998.

[12] E. B. Myers, D. C. Ralph, J. A. Katine, R. Louie, and R. A. Buhrman. Current-induced switching of domains in magnetic multilayer devices. *Science*, 285(5429):867–870, August 1999.

[13] O. Misochko, M. Lebedev, N. Georgiev, and T. Dekorsy. Coherent phonons in ndba2cu3o7x single crystals: Optical-response anisotropy and hysteretic behavior. *Journal of Experimental and Theoretical Physics*, 98(2):341–347, February 2004.

[14] A.K. Zvezdin and V. A. Kotov. *Modern magnetooptics and magnetooptical materials*. Institute of Physics Publishing, 1997.

[15] Karl Heinz Bennemann. *Nonlinear optics in metals*. Oxford Science Publications, 1998.

[16] Yuen-Ron Shen. *The Principles of Nonlinear Optics*. Wiley-Interscience, John Wiley and Sons, 1984.

[17] I. Radu, G. Woltersdorf, M. Kiessling, A. Melnikov, U. Bovensiepen, J.-U. Thiele, and C. H. Back. Laser-induced magnetization dynamics of lanthanide-doped permalloy thin films. *Phys. Rev. Lett.*, 102(11):117201–4, March 2009.

[18] Uwe Conrad. *Statische und dynamische Untersuchungen ultradünner Metallfilme mit optischer Freqeunzverdopplung und nichtlineare Mikroskopie*. PhD thesis, Freie Universität Berlin, 1999.

[19] Y.R. Shen. Surface second harmonic generation: A new technique for surface studies. *Annual Review of Materials Science*, 16:69–86, 1986.

[20] Hans Lüth. *Surfaces and Interfaces of Solid Materials*. Springer-Verlag Berlin, 1995.

[21] Björn Lewitz. Aufbau und Inbetriebnahme eines polaren Kerrspektrometers zur Messung im Ultrahochvakuum. Master's thesis, Freie Universität Berlin, 2007.

[22] Th. Mühge, A. Stierle, N. Metoki, H. Zabel, U. Pietsch. Structural properties of high-quality sputtered Fe films on $Al_2O_3(11\bar{2}0)$ and MgO(001) substrates. *Applied Physics A - Solids and Surfaces*, 59:659–665, 1994.

[23] G. Fahsold, G. König, W. Theis, A. Lehmann, K.H. Rieder. Epitaxial FeO films from ultrathin Fe on MgO(001) studied by He-atom scattering. *Applied Surface Science*, 137:224–235, 1999.

[24] M. Rickart, B.F.P Roos, T. Mewes, J. Jorzick, S.O. Demokritov, B. Hillebrands. Morphology of epitaxial metallic layers on MgO substrates: influence of submonolayer carbon contamination. *Surface Science*, 495:68–76, 2001.

[25] P. Grünberg, S. Demokritov, A. Fuss, R. Schreiber, J. A. Wolf and S. T. Purcell. Interlayer exchange, magnetotransport and magnetic domains in fe/cr layered structures. *Journal of Magnetism and Magnetic Materials*, 104-107:1734–1738, 1992.

[26] B. T. Jonker J. J. Krebs and G. A. Prinz. Properties of fe single-crystal films grown on (100)gaas by molecular-beam epitaxy. *J. Appl. Phys.*, 61:2596–2599, 1987.

[27] Oxford Applied Research. *Mini E-Beam Evaporator - Model EGCO4*. Crawley Mill, Witney, Oxon, OX8 5TJ, United Kingdom, June 1999.

[28] Günther Sauerbrey. Verwendung von schwingquarzen zur wägung dünner schichten und zur mikrowägung. *Zeitschrift für Physik*, 155:206–222, 1959.

[29] MAXTEK, INC. *Maxtek Thickness Monitor - Model TM-350/400*. 5980 Lakeshore Drive, Cypress, CA 90630-3371 Tel: (714) 828-4200 Fax: (714) 828-4443 Email: sales@maxtekinc.com support@maxtekinc.com, 11 edition, August 2005.

[30] P. Blomqvist, R. Wäppling. Structural properties of ultrathin bcc Co (111) layers. *Journal of Crystal Growth*, 252:120–127, 2001.

[31] SPECS GmbH, Voltastrasse 5, 13355 Berlin, Germany. Safire 4 - a software for rheed analysis.

[32] W.Göpel M.Henzler. *Oberflächenphysik des Festkörpers*. Teubner Verlag, 1994.

[33] A. Schatz, S. Dunkhorst, S. Lingnau, U. von Hrsten and W. Keune. RHEED intensity oscillations during epitaxial growth of fcc Fe on Cu(001). *Surface Science*, 310:595–600, 1994.

[34] Franz Schwabl. *Quantenmechanik*. Springer-Verlag Berlin, 1992.

[35] Omicron Vakuumphysik GmbH. *The UHV AFM/STM User's Guide*. Idsteiner Straße 78 D-65232 Taunusstein Germany, June 2000.

[36] I. Horcas, R. Fernandez, J.M. Gomez-Rodriguez, J. Colchero, J. Gomez-Herrero, and A.M.Baro. WSXM: A software for scanning probe microscopy and a tool for nanotechnology. *Review of Scientific Instruments*, 78:013705, 2007.

[37] K.Thürmer, R. Koch, M. Weber, and K.H. Rieder. Dynamic Evolution of Pyramid Structures during Growth of Epitaxial Fe(001) Films. *Physical Review Letters*, 75, 9:1767–1771, 1995.

[38] Switzerland Ribbonsoft GmbH, 8046 Zurich. qcad, 2d computer aided design.

[39] Costa-Krämer, J. L. and Menendez, J. L. and Cebollada, A. and Briones, F. and Garcia, D. and Hernando, A. Magnetization reversal asymmetry in fe/mgo(001) thin films. *Journal of Magnetism and Magnetic Materials*, 210(1-3):341–348, February 2000.

[40] J.C. Slonczewski. Excitation of spin waves by an electric current. *Journal of Magnetism and Magnetic Materials*, 195:261–268, 1998.

[41] John David Jackson. *Classical Electrodynamics*. John Wiley & Sohns New York, 1962.

[42] Mark C. Barnes, Doh-Y. Kim and Nong M. Hwang. The mechanism of gold deposition by thermal evaporation. *Journal of Ceramic Processing Research*, 1:45–52, 2000.

[43] A. Melnikov, O. Krupin, U. Bovensiepen, K. Starke, M. Wolf, and E. Matthias. Shg on ferromagnetic gd films: indication of surface-state effects. *Applied Physics B: Lasers and Optics*, 74(7):723–727, May 2002.

[44] T. Miyazaki and N. Tezuka. Giant magnetic tunneling effect in $Fe/Al_2O_3/Fe$ junction. *Journal of Magnetism and Magnetic Materials*, 139:231–234, 1995.

[45] J.H. Weaver and E.E. Koch C. Krafka, D.W. Lynch. *Optical Properties of Metals*, volume I and II. Fachinformationszentrum Energie - Physik - Mathematik GmbH, Karlsruhe, Germany, 1981.

Acknowledgements

This work wouldn't have been possible without the help and support of my friends and colleagues. I would therefore like to thank the following people for their precious input.

First of all, I would like to thank my supervisor *Uwe Bovensiepen* for introducing me into this topic and making this thesis possible. He was always there to help with words and deeds and had a lot of good ideas in cases some of the experiments didn't work.

Alexey Melnikov was the one whom I directly worked together with. He is an absolute expert when it comes femtosecond lasers and electron dynamics and the project covered by this thesis was mainly his idea. Also, Alexey was the one who helped me shaping the text of this thesis and who had an infinite amount of patience reading and correcting my texts. Thank you, Alexey. Without you, this thesis would never have been possible.

I would like to thank *Michael Karcher* who was my lab-mate in the MBE laboratory at Prof. Fumagalli's workgroup. Michael knows almost the entire experimental setup in the Fumagalli workgroup by heart and he was just an invaluable help during all the experiments for sample preparation. I have learned so incredibly many things from Michael and still keep learning from him. Thanks Michael!

My friend *Daniel Sachse* for helping me with LaTeX, helping with inkscape to make the drawings and giving to good tips on designing the magnet. Also, Daniel was always there to support me mentally, also together with his enchanting wife *Lili*. He kept on driving me all the time.

Anja Diesing helped me with some of the CAD drawings, she is a real talent when it comes to making things visual on the computer. Thanks Anja.

Axel Luchterhand assisted me in the workshop when building the magnet.

The following people haven't helped me directly but I still would like to thank them for their support: *Wolf Dieter Woidt*, *Jonas Hoffmann*, *Milian*

Wolff, *Marco Starace*, *Jens Dreger*, *Philipp Neuser*, *Prof. Robert Schrader* and many more I forgot to mention. Thank you, everybody!

Last but not least, I'm especially thankful to my parents and my sister Anna and my brother Philippe. Without their restless support and help I probably would have never got so far and being able to earn a degree at a university. Danke *Mama*, *Papa*, *Philippe* und *Anna*!